

**A story of dust and ice — constraining
dust-driven immersion freezing in climate
models using spaceborne retrievals**

Der Fakultät für Physik und Geowissenschaften
der Universität Leipzig

eingereichte

D I S S E R T A T I O N

zur Erlangung des akademischen Grades

Doctor rerum naturalium
Dr. rer. nat.

vorgelegt
von

M.Sc. Diego Villanueva

geboren am 6. November 1991 in Chile

Gutachter

Prof. Dr. Ina Tegen

Prof. Dr. Ulrike Lohmann

Verleihungsbeschluss: 20. September 2021

The present study was prepared between October 2017 and May 2021

at the Leibniz Institute for Tropospheric Research (TROPOS)

Department 'Modeling of Atmospheric Processes'

Permoserstraße 15

04318 Leipzig

Germany

The work was supervised by

Prof. Dr. Ina Tegen

Bibliografische Beschreibung

Diego Villanueva

Eine Geschichte von Staub und Eis — Verbesserung staubgetriebene Gefrieren von Wolkenröpfchen in Klimamodellen mithilfe weltraumgestützten Beobachtungen

Universität Leipzig, Doktorarbeit

Mai 2021

129 Seiten, 154 Literaturverweise, 104 Abbildungen, 7 Tabellen

Kurzzusammenfassung

Wolken und Aerosole beeinflussen den Energiehaushalt und den Wasserkreislauf der Erde. Es gibt zunehmend Hinweise darauf, dass Staubaerosol die Vereisung von Wolken, ihren Strahlungseffekt und ihre Antwort auf die globale Erwärmung beeinflusst. Um den Klimawandel genauer zu projizieren, ist es daher wichtig, den Weg von staubinduzierten Gefrierprozessen zur Vereisung der Wolken besser zu simulieren. Gegenwärtige Gefrierschemen, die von Laborergebnissen auf größere atmosphärische Skalen extrapolieren, sind jedoch limitiert in ihrer Anwendbarkeit. Basierend auf Satelliten-Beobachtungen von Wolkenphasen und Aerosolen wird in dieser Arbeit untersucht, wie das staubbedingte Gefrieren in Klimamodellen verbessert werden kann, um Klimaeffekte von Staubeiskeimen genauer abschätzen zu können. Zu diesem Zweck werden Reanalyse-Daten eines Aerosolmodells mit dem Satelliten-Beobachtungen von Wolkenphase kombiniert und die globale Kovariabilität zwischen Mineralstaubaerosol und Wolkenvereisung abgeschätzt. Basierend auf einem weltraumgestützten Lidar, einer Lidar-Radar Kombination und einer Radiometer-Polarimeter Kombination werden hemisphärische und saisonalen Kontraste in der Wolkenphase lokalisiert und quantifiziert. Schließlich werden diese Schätzungen verwendet, um den Einfluss des Mineralstaubes auf das Gefrieren von Wolkenröpfchen in einem Klimamodell einzugrenzen. Die vorgelegten Ergebnisse zeigen, dass Beobachtungen des Kontrastes in der Wolkenphase dafür verwendet werden können, das staubgetriebene Gefrieren von Wolkenröpfchen in Klimamodellen zu optimieren.

In den Extratropen steigt die durchschnittliche Häufigkeit von Eiswolken für höhere Mineralstaub-Mischungsverhältnisse um +5% bis +10%. Bei ähnlichen Mischungsverhältnissen von Mineralstaub kann die Häufigkeit von Eiswolken für verschiedene Breiten immer noch variieren. Einzelne Wolkenphasen-Produkte neigen dazu, zu viele Wolken als flüssig für Temperaturen unter -30°C und zu viele als Eis für Temperaturen über 10°C zu klassifizieren. Bei -30°C liegen die hemisphärischen und die saisonalen Kontraste — relativ zur südlichen Hemisphäre bzw. zum borealen Frühjahr — zwischen +21% und +39% für einzelne Produkte in der Wolkenphase und zwischen +52% und +75% für eine Kombination der Produkte. Diese Kontraste wurden verwendet, um die Effizienz der Staubeiskeime im Modell zu optimieren. Nach erfolgter Optimierung stimmt das Modell besser mit den aus Beobachtungen der geschätzten Kontraste in der Wolkenphase überein und zeigt einen staubbedingten nordhemisphärischen Netto-Strahlungseffekt von $0.14 \pm 0.13 \text{ W m}^{-2}$ durch die Vereisung, der niedriger ist als bisher angenommen. Diese Änderungen sind mit einer Abnahme der Gesamtwassermenge in den Wolken und einer Verstärkung des stratiformen Niederschlags auf Kosten des konvektiven Niederschlags verbunden.

Bibliographic Description

Diego Villanueva

A story of dust and ice — constraining dust-driven immersion freezing in climate models using spaceborne retrievals

University of Leipzig, Doctoral Thesis

May 2021

129 pages, 154 references, 104 figures, 7 tables

Abstract

Clouds and aerosols impact the Earth’s thermostat and precipitation. There is increasing evidence that dust aerosol frequently controls cloud glaciation, modifying clouds’ radiative effect and response to global warming. For realistic climate change projections, it is crucial to improve the simulated pathway between dust immersion freezing and cloud glaciation. However, current freezing schemes, which extrapolate laboratory results to larger atmospheric scales, are poorly constrained. Based on spaceborne observations of cloud-phase and aerosols, we explore whether dust-driven immersion freezing can be improved in a climate model so that the climate impact of dust ice-nuclei can be estimated more accurately. Combining an aerosol model reanalysis with spaceborne retrievals of cloud phase, we estimated the global co-variability between mineral dust aerosol and cloud glaciation. Relying on a spaceborne lidar, a lidar-radar synergy, and a radiometer-polarimeter synergy, we also locate and quantify the hemispheric and seasonal contrast in cloud-phase. Finally, we use these estimations to refine the dust-driven droplet freezing in a climate model. Our results show that observations of cloud-top phase contrasts may be used to evaluate dust-driven droplet freezing in climate models.

In the extratropics, the average frequency of ice cloud increases by +5% to +10% for higher mineral dust mixing-ratios on a day-to-day basis. For similar mixing-ratios of mineral dust, we found that the ice frequency can still vary between latitudes, especially between Hemispheres and between mid- and high-latitudes. By using only retrievals for which satellite products agree on cloud-phase, we find that the cloud-phase transition from liquid to ice occurs within a narrower temperature range. This suggests that individual products tend to classify too many clouds as liquid for temperatures below -30°C and too many as ice for temperatures above -10°C . At -30°C , the hemispheric and seasonal contrasts — relative to the Southern Hemisphere and boreal spring, respectively — lie between +21% to +39% for individual cloud-phase products and between +52% to +75% for a combination of products. We use these contrasts to tune the dust ice-nuclei efficiency in the model, limiting their effect during clean conditions. Consequently, the model agrees better with the estimated cloud-top-phase contrasts and a dust-driven glaciation effect of $0.14 \pm 0.13 \text{ W m}^{-2}$ in the Northern Hemisphere, which is lower than previously assumed. These changes are associated with a decrease in the cloud liquid water path and a weak enhancement of the stratiform precipitation at the expense of convective precipitation. Our results show that observations of cloud-top phase contrasts may be used as a constraint for dust-driven droplet freezing in climate models. Thus, our constraining approach may help to achieve more accurate climate predictions and direct future climate model development.

Contents

1	Introduction	1
1.1	General: Cloud-phase and aerosols	1
1.1.1	Cloud phase and climate	1
1.1.2	Aerosols and clouds	3
1.2	Topic: Dust-driven cloud glaciation	5
1.2.1	Ice-nucleating particles and immersion freezing	5
1.2.2	Mineral dust INP	6
1.2.3	Large scale observations of dust-driven cloud glaciation	7
1.3	Importance: From dust-driven immersion freezing to cloud radiative effect	9
1.4	Approach: Constraining dust-driven immersion freezing in climate models using spaceborne retrievals.	10
2	The day-to-day co-variability between mineral dust and cloud glaciation:	
	A proxy for heterogeneous freezing	13
2.1	Introduction	14
2.2	Data	16
2.2.1	CALIPSO-GOCCP	16
2.2.2	MACC and ERA-Interim reanalyses	16
2.3	Methods	17
2.3.1	Selection of cloud profiles	17
2.3.2	Regridding and rebinning	19
2.3.3	Meteorological regimes	19
2.3.4	Classification of dust loads and day-to-day correlation	20
2.3.5	Data availability and averaging order	21
2.4	Results	22
2.4.1	Case study	22
2.4.2	Temperature dependence	22
2.4.3	Latitude dependence	24
2.4.4	Constraining the influence of static stability and humidity on the dust-cloud-phase relationship	30
2.5	Discussion	32
2.5.1	North-South contrast	32
2.5.2	Assumptions and uncertainties	34
2.6	Conclusions	37

2.7	Appendix: Related cloud products	38
2.7.1	2B-CLDCLASS	38
2.7.2	DARDAR-MASK	39
2.7.3	FPR _{DARDAR,ALT}	39
2.7.4	Case study comparison	39
2.7.5	Temperature comparison	40
2.7.6	Latitude comparison	42
2.S	Supporting Information for "The day-to-day co-variability between mineral dust and cloud glaciation: A proxy for heterogeneous freezing"	43
3	The hemispheric and seasonal contrast in cloud thermodynamic phase from A-Train spaceborne instruments	53
3.1	Introduction	54
3.2	Data and Methods	55
3.2.1	A-Train cloud phase products	55
3.2.2	Collocation and GDP2 ensemble	59
3.2.3	Sample size	60
3.3	Results	62
3.3.1	Agreement	62
3.3.2	Frequency Phase Ratio	63
3.3.3	Hemispheric and seasonal contrast	63
3.3.4	Quantification and attribution	66
3.3.5	Uncertainty	68
3.4	Conclusions	69
3.S	Supporting Information for "Hemispheric and seasonal contrast of cloud phase from the A-Train"	71
4	Constraining the impact of dust-driven droplet freezing on climate using cloud top phase observations	80
4.1	Introduction	81
4.2	Methods	82
4.2.1	Model description	82
4.2.2	Satellite simulator and A-Train observations	82
4.2.3	Freezing schemes	83
4.2.4	Model Simulations	84
4.2.5	Quantifying cloud glaciation and cloud-top-phase contrasts	84
4.3	Results	86
4.3.1	Dust-driven cloud glaciation	86
4.3.2	Satellite constraints to cloud glaciation	86
4.3.3	Other climate models	87
4.3.4	Climate implications	88
4.4	Discussion	89
4.4.1	Dust-INP and meteorology	89

4.4.2	Liquid water depletion and dust-driven glaciation in the LD scheme . . .	89
4.4.3	Droplet freezing and precipitation	90
4.4.4	A misrepresented ice process?	90
4.5	Conclusions	91
4.S	Supporting Information for "Hemispheric and seasonal contrast of cloud phase from the A-Train"	92
	Conclusion	107
	Outlook	109
	References	111
	List of Abbreviations	124
	List of Symbols	126
	List of Figures	127
	List of Tables	129
	Appendix	130
A	Acknowledgements	130
B	List of Publications	131
C	Curriculum Vitae	133
D	Declaration of Independence	134

Chapter 1

Introduction

1.1 General: Cloud-phase and aerosols

1.1.1 Cloud phase and climate

Clouds influence the climate. They control the amount of shortwave radiation reflected back to space and absorb terrestrial radiation that would otherwise escape the atmosphere. Cloud droplets reflect more light compared to ice crystals, as liquid droplets are smaller and their radius is closer to the solar wavelength. Thus, thick low clouds — mostly composed of liquid — usually reflect more solar radiation and have an overall cooling effect on the planet. Thin high clouds — mostly composed of ice — reflect less light and thus tend to warm the climate. Moreover, microphysical processes in clouds control the precipitation cycle. Convective clouds produce high amounts of precipitation in a relatively short time, while stratiform clouds have lower precipitation rates but a longer lifetime. While warm clouds at temperatures higher than 0°C tend to produce rain through droplet-droplet aggregation, cold clouds at temperatures below 0°C precipitate mainly through the ice phase (Mülmenstädt et al., 2015). In addition, due to their latent heat, clouds play a major role in the global energy transport in the atmosphere.

The representation of cloud-phase in climate models impacts how much solar radiation is reflected by clouds. In most state-of-the-art climate models, mid-level clouds reflect too little solar radiation over the Southern Ocean compared to observations (Bodas-Salcedo et al., 2014). As a result, the radiative balance over the Southern Hemisphere is not correctly simulated in climate models, with too much radiation entering the ocean (Trenberth & Fasullo, 2010). This bias in cloud albedo leads to biases in precipitation and energy transport at the mid-latitudes (Hawcroft et al., 2017). The cloud albedo bias is closely related to the frequency of ice clouds in the mixed-phase regime, as liquid clouds reflect more solar radiation (McCoy et al., 2014a, 2014b; Matus & L’Ecuyer, 2017). Thus, to improve the albedo bias in the Southern Ocean, it is crucial to improve the representation of the cloud-phase partitioning in models.

The relation between cloud-phase and cloud albedo affects how clouds respond to global warming. In a warmer climate, the low cloud cover and albedo decrease in the extratropics, resulting in a positive cloud feedback (Zelinka et al., 2020). However, with higher isotherms the sinks




Figure 1.1: Diagram of the negative cloud-phase feedback. In a warmer climate (right side) isotherms are higher (red arrow) and fewer clouds are affected by droplet freezing, which results in a higher cloud liquid water content and solar reflectivity. In models, the magnitude of this feedback depends on the effectivity of cloud glaciation.

of cloud water through cloud glaciation decrease, as fewer clouds remain in the mixed-phase regime, which will be located higher up in the atmosphere. The associated decrease in cloud glaciation dampens the overall positive cloud feedback (Zelinka et al., 2020). Fig. 1.1 indicates how this cloud feedback due to cloud glaciation depends on the cloud ice frequency in climate models. For higher mean-state ice frequencies, this negative cloud-phase feedback is stronger, leading to a weaker overall positive cloud feedback at the extratropics (Zelinka et al., 2020; Tan et al., 2016). Indeed, for most general circulation models, ice frequencies are too high or too low compared with observations, resulting in either too many or too few ice clouds converted to liquid in warmer climates (McCoy et al., 2016). For this reason, the representation of cloud-phase is one of the main sources of uncertainty in climate projections and, therefore, has received increasing attention in the last decades.

In climate models, cloud-phase is closely related to cloud cover, water content, and precipitation, but the physical mechanisms behind are still poorly understood. Climate models with higher ice cloud frequencies have a lower Liquid Water Path (LWP) and higher cloud fraction (McCoy et al., 2016). The latter positive correlation with cloud fraction is rather counterintuitive, as observations suggest that ice cloud frequency should be anticorrelated with cloud cover due to enhanced precipitation through the ice phase (Heymsfield et al., 2010; H. Morrison et al., 2012). In addition, the cloud-phase affects how the cloud water content responds to climate warming. In general, the shift of isotherms to higher altitudes produce an increase in LWP in a warmer climate. However, models with higher ice cloud frequencies suffer a higher LWP increase with global warming in the extratropics (McCoy et al., 2015), as more ice clouds are affected by the shift in the isotherms. The height increase of the mixed-phase regime in a warmer climate contributes 20% to 80% of this increase in LWP for warmer climates depending on the climate model (McCoy et al., 2015). In turn, the LWP increase for warmer climates dominates much of the cloud-phase feedback at the extratropics (Ceppi et al., 2016). Therefore, a better representation of cloud glaciation could help clarify the mechanism behind the cloud-phase feedback.

1.1.2 Aerosols and clouds

Aerosols modify the number and size of cloud droplets and ice particles, which determines the Cloud Radiative Effect (CRE). Aerosols affect cloud hydrometeors by acting as Cloud Condensation Nuclei (CCN) or Ice-Nucleating Particles (INP). Fig. 1.2 illustrates how clouds are modified by CCN and INP. CCN can lead to new droplet formation, increasing the number of cloud droplets and increasing the cloud albedo (Twomey, 1974). As more cloud droplets are present, they compete for the available water vapor leading to a smaller droplet radius, which slows down autoconversion and rain processes, increasing cloud lifetime (Albrecht, 1989). On the other hand, INP — a more rare type of aerosol — can trigger droplet freezing. After droplets freeze, the resulting ice particles tend to grow at the expense of existing cloud droplets, eventually leading to precipitation (Wegener, 1911; Bergeron, 1935; Findeisen et al., 2015). Therefore, cloud glaciation is associated with lower cloud albedo and lower cloud lifetime (Vergara-Temprado et al., 2018), although the magnitude of these changes is still under debate



../sect/intro/fig/aci.png

Figure 1.2: Main types of aerosol-cloud interactions. Both Cloud Condensation Nuclei (CCN) and Ice-Nucleating Particles (INP) can affect the cloud reflectivity and lifetime. Without the ice-phase, the dominant precipitation mechanism is autoconversion, which is slower for smaller cloud droplets. The impact of INP on cloud lifetime and albedo is closely related to the number of cloud droplets per INP.

(IPCC et al., 2007). As a result, aerosol-cloud interactions lead to uncertainty in climate predictions (Bellouin et al., 2020; Forbes & Ahlgrimm, 2014), as both the cloud albedo and cloud lifetime affect the cloud radiative effect and how clouds respond to climate change.

Although they play a key role in cloud-phase and climate, Aerosol-Cloud Interactions (ACI) are still poorly understood. The study of ACI present some difficult challenges. Meteorological factors have usually a higher impact on cloud properties compared to aerosols and can, therefore, confound the correlation between aerosols and clouds (Gryspeerd et al., 2016). For example, relative humidity and static stability are co-varying with aerosols, cloud fraction and cloud-phase (Zamora et al., 2018; J. Li et al., 2017). Additionally, constraining ACI in climate models through mean-state variables alone is insufficient, as there are often multiple model configurations that may lead to the same atmospheric state. Therefore, it has been proposed that observational references for process rates could be a key to improving the representation of ACI (Mülmenstädt et al., 2020). Therefore, new strategies to constrain ACI are urgently needed, which should focus on process rates while considering co-varying meteorology.

1.2 Topic: Dust-driven cloud glaciation

1.2.1 Ice-nucleating particles and immersion freezing

INP can enhance ice nucleation in the cirrus regime through deposition and pore condensation freezing and in the mixed-phase regime through contact and immersion freezing. During deposition and pore condensation freezing, ice crystals form onto the INP. During contact freezing, hydrophobic INP initiate the freezing of a cloud droplet after colliding and for immersion freezing, hydrophilic INP are first activated to cloud droplets that subsequently freeze. Without INP, cloud droplets freeze at temperatures between -40°C and -35°C depending on their droplet radius, as bigger droplets can freeze at higher temperatures. Temperatures lower than -35°C are referred to as the cirrus regime. For such temperatures, INP can lead to ice nucleation by direct deposition of water vapor into INP (deposition freezing) or after water condensates into pores of the INP (pore condensation freezing), even when the humidity lies below water supersaturation. Pore condensation freezing is believed to be much more efficient than deposition freezing but it is still poorly understood (Kanji et al., 2017). Temperatures higher than -35°C are referred to as the mixed-phase regime. In this regime, INP lead to droplet freezing mainly by offering a surface where ice can crystalize inside the droplet (immersion freezing) or at the droplet's surface (contact freezing) (Hoose & Möhler, 2012). Immersion freezing is believed to dominate over contact freezing (Kanji et al., 2017) and thus dominates droplet freezing in mixed-phase clouds.

Immersion freezing rates are controlled by the surface concentration of INP and by temperature. Atmospheric INP concentrations are very low and the background free-tropospheric INP concentration relevant for mixed-phase clouds is estimated to be only about 10 INP/stdL (Lacher et al., 2018). Because freezing can only start on ice-active sites in the aerosol's surface, the droplet freezing rate in a cloud depends on the surface area concentration of INP (Niedermeier et al., 2015; Hartmann et al., 2016). For typical INP, the ice-nucleation efficiency increase by about an order of magnitude after a temperature decrease of about 5 K (Niemand et al., 2012). Therefore, the effect of temperature variations typically dominates over the variability in aerosol concentration, which presents a challenge when studying the role of INP in cloud glaciation.

The study of the role of mineral dust aerosol particles as INP has gained importance in the last decade, due to their ubiquity and ice-nucleating efficiency. Many types of atmospheric particles such as dust, soot, biological and organic aerosols are able to act as INP (Hoose & Möhler, 2012). Consequently, a plethora of laboratory studies have tried to estimate the ice-nucleating efficiency of different aerosols for different freezing modes and different atmospheric conditions (Hoose & Möhler, 2012; Kanji et al., 2017). Due to the ubiquity of dust aerosol, many of these studies have focused on studying the ice-nucleating properties of different types of dust minerals. From the different dust minerals relevant for atmospheric dust, K-feldspar and clay minerals like Montmorillonite and Kaolinite have been found to be particularly effective INP in the immersion mode (Atkinson et al., 2013; Boose et al., 2016; Diehl & Wurzler, 2004; Diehl et al., 2006). To simplify the parameterization of droplet freezing in models, atmospheric dust is

usually represented by a single dust mineral. In terms of their immersion freezing potential, soils in the Northern Hemisphere are better represented by Montmorillonite, while in the Southern Hemisphere they are better represented by Kaolinite (Claquin et al., 1999; Hoose et al., 2008). In remote regions such as the Southern Ocean where marine biogenic INP is dominant, mineral dust is believed to play a secondary role in cloud glaciation (Burrows et al., 2013; Vergara-Temprado et al., 2017; Huang et al., 2018). Nevertheless, we focus on dust because its ubiquity and efficiency as INP suggest that it should dominate over other INP types in most regions over the globe.

1.2.2 Mineral dust INP

The seasonal- and global variability in dust emissions are well-studied, although uncertainties remain on future trends. It has been estimated that land-use change has resulted in higher dust emissions since pre-industrial times (Stanelle et al., 2014). Dust emission peak in both boreal spring (Zender & Kwon, 2005; Cowie et al., 2014; Luo et al., 2015) and austral spring (M. Wu et al., 2020; Kok et al., 2021). Although the main dust sources are located in the Northern Hemisphere and particularly in North Africa, there are important dust sources at the Southern mid-latitudes that deliver dust to large parts of the southern hemisphere (Albani et al., 2012; Johnson et al., 2011; F. Li et al., 2008). Nevertheless, dust concentrations in the Northern Hemisphere are in average between one and two orders of magnitude higher compared to the Southern Hemisphere.

Not only dust concentrations are relevant for immersion freezing, but also dust size. The number concentration of dust aerosols, which is the relevant measure for contact freezing and CCN, is dominated by particle diameters below 0.5 μm . On the other hand, the surface area concentration of dust, the relevant measure for immersion freezing, is controlled by both the fine- (radius smaller than 0.5 μm) and coarse-mode (radius larger than 0.5 μm) (Mahowald et al., 2014). Dust size is also relevant for the aerosol lifetime in the atmosphere, as fine dust has a lower sedimentation rate and stays, therefore, longer in the atmosphere than coarse dust particles that settle quickly to the ground (Seinfeld & Pandis, 1998). However, the fine-to-coarse ratio of dust particles is still not well-represented in climate models, which tend to underestimate coarse dust (Adebiyi & Kok, 2020).


Besides INP concentration, there are several microphysical processes that may enhance dust-driven cloud glaciation. Fig. 1.3 summarizes some of these processes. Through the Wegener–Bergeron–Findeisen (WBF) process (Wegener, 1911; Bergeron, 1935; Findeisen et al., 2015), ice particles grow quickly while cloud droplets are depleted, which can lead to the glaciation of the entire cloud. Some conditions may lead to ice multiplication during or after droplet freezing, in what is known as Secondary Ice Production (SIP; Field et al. (2017)). Although some SIP mechanisms like the Hallett–Mossop process are well understood (Hallett & Mossop, 1974), others — including ice shattering and fragmentation — are still poorly understood (Lauber et al., 2018; Sullivan et al., 2018). Moreover, some INP are thought to act as INP multiple times in a process known as INP-recycling (Solomon et al., 2015). It has also been proposed that

INP could be pre-activated at cirrus temperatures through pore condensation freezing and then act with enhanced efficiency in the Mixed-Phase Clouds regime (Wagner et al., 2016). On the other hand, there are several particle properties that can affect the efficiency of dust ice-nuclei. Some of these properties are illustrated in Fig. 1.4. The INP efficiency of a dust particle is determined by its ice-active sites (Kiselev et al., 2017). The number of such active-sites depends on the particle size and dust mineral type. With decreasing temperature, the number of sites that become ice-active also increases exponentially. In addition, as aerosols age, they frequently gain a soluble coating which may alter their ice-nucleating properties. For example, sulfate coatings are believed to deactivate INP (Cziczo et al., 2009). Aerosols can also act as carriers for smaller aerosols. It has been shown that mineral dust particles mixed with ice-nucleation-active macromolecules (radius of about 10 nm; Fröhlich-Nowoisky et al., 2015) may be abundant in the atmosphere and result in a higher INP efficiency compared to typical dust aerosol (Augustin-Bauditz et al., 2016; O’Sullivan et al., 2014, 2016, 2018; Petters & Wright, 2015; W. Hu et al., 2020).

1.2.3 Large scale observations of dust-driven cloud glaciation

There is a significant large-scale spatiotemporal correlation between cloud glaciation and dust aerosol occurrence. Ice cloud frequency tends to be higher over regions where dust is more frequent (Choi et al., 2010; Tan et al., 2014; J. Li et al., 2017; Kawamoto et al., 2020), especially for temperatures near -20°C . The spatial correlation between dust and cloud ice frequency is particularly high between the hemispheres, with a notably higher cloud ice frequency over the Northern Hemisphere, where the main dust sources are located (Kanitz et al., 2011; Tan et al., 2014). This contrast can be also observed between regions over the ocean in both hemispheres (A. E. Morrison et al., 2011), and for different cloud types (Bruno et al., 2021), suggesting that land-ocean differences in cloud regimes may play a minor role in the contrast. Below clouds, ice production — detected as ice virgae — has also been found to be higher in the Northern Hemisphere as well (Zhang et al., 2018). In the Northern Hemisphere, cloud ice production is also correlated with the location relative to the main dust sources in the “dust belt” of the Northern Hemisphere (Zhang et al., 2012). Within mesoscale cloud systems, regions where heterogeneous nucleation by dust aerosol occur can be distinguished by an increase in cloud top temperature observed from space (R. Li et al., 2017). In addition to the spatial correlation, cloud glaciation has been repeatedly found to be temporally correlated with dust concentration on the day-to-day (Seifert et al., 2010), monthly (Tan et al., 2014), and seasonal scales (Zhang et al., 2015, 2018).

Cloud-phase and aerosols can be detected from various spaceborne instruments. Active spaceborne instruments emit a certain wavelength downwards and detect the reflected signal, which is used to detect cloud droplets, ice particles and aerosols. Lidar instruments use light and are, therefore, sensitive to small particles such as cloud droplets and aerosols, while radar instruments emit radio waves which are more sensitive to large particles such as ice crystals. Passive spaceborne instruments use the solar light that is reflected back to space to retrieve the optical properties of clouds and aerosols. Spaceborne radiometers are able to detect multiple wave-

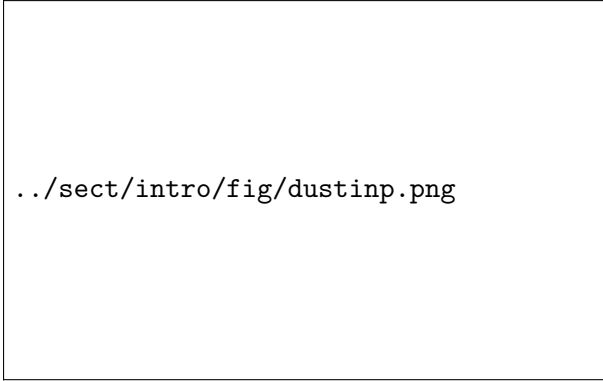


`../sect/intro/fig/micro.png`

Figure 1.3: Microphysical processes relevant for mixed-phase clouds. Dashed arrows correspond to processes that are generally ignored in climate models. WBF: Wegener–Bergeron–Findeisen.

length channels at once, while multi-angle polarimeters can detect the polarization of reflected solar light from different angles. Because such passive instruments take advantage of the solar radiation, their spatial coverage is higher compared to active instruments. However, passive instruments are usually limited to cloud tops, while active instruments can often penetrate deeper into clouds.

There are important biases related to the spaceborne detection of cloud and aerosols. Although a spaceborne lidar can detect the presence of aerosols (Y. Wu et al., 2014), such retrievals are not sensitive to low dust concentration, as they often occur in the Southern Hemisphere (Ridley et al., 2016; Toth et al., 2018). An additional problem is that such dust retrievals from space are not reliable during cloudy conditions, which is when aerosol-cloud interactions occur. On the other side, cloud-phase retrievals are very sensitive to instrument biases. For instance, the spaceborne lidar usually ignores ice virgae below cloud liquid top (Huang et al., 2012). Similarly, the cloud-top-phase retrievals from spaceborne radiometers and polarimeters tend to be biased for thin clouds (Stengel et al., 2020). Therefore, some cloud products combine different spaceborne instruments to retrieve the cloud phase. For example, because spaceborne radars can penetrate through cloud droplets and detect ice, lidar-radar combinations are often used for cloud-phase retrievals (Delanoë & Hogan, 2010; Mioche et al., 2014).




```
../sect/intro/fig/dustinp.png
```

Figure 1.4: Factors controlling the efficiency of dust ice-nuclei. The number of sites on the particle surface that are ice-active depend on the mineral type and increase for lower temperatures and larger particles. Particle coatings may deactivate the ice-nuclei, while aerosol mixtures may provide additional ice-active sites.

1.3 Importance: From dust-driven immersion freezing to cloud radiative effect

The gaps in our understanding of dust-driven cloud glaciation and its representation in climate models contributes to the uncertainty in climate predictions. In climate models, the cloud-phase in the mixed-phase cloud regime is the most important factor controlling the cloud albedo in the Southern Ocean and determines the magnitude of the cloud feedback to climate warming in the extratropics (Bodas-Salcedo et al., 2019; Murray et al., 2021). Moreover, dust-driven immersion freezing is one of the most important mechanisms controlling the cloud-phase in mixed-phase clouds. Therefore, by gaining a better reference for dust-driven immersion freezing we may improve the representation of mixed-phase clouds and, consequently, achieve more accurate climate predictions (Korolev et al., 2017).

Current freezing schemes, which extrapolate laboratory results to larger atmospheric scales, are associated with high uncertainty. Such freezing schemes are based on field measurements, laboratory measurements (See Sect. 4.2.3), or theoretical frameworks, such as classical nucleation theory (for details, see Ickes, 2015, where the schemes and their implementation in ECHAM-HAM are described). Most efforts towards improving the immersion freezing in climate models follow a bottom-up approach, where the freezing processes and INP properties observed in laboratory experiments are extrapolated to larger atmospheric scales (Korolev et al., 2017). However, up to now the evaluation of laboratory-based freezing schemes has been limited to observations of the cloud-phase mean-state (Tan et al., 2016). Such evaluations do not ensure the correct representation of immersion freezing, as other factors also affect the average cloud-phase partitioning (Dietlicher et al., 2019). Moreover, there is no certainty that further laboratory experiments on cloud glaciation will eventually lead to a better representation of cloud glaciation in general circulation models. Fig. 1.5 illustrates the bottom-up approach compared to a top-down approach. The main difference between the approaches is on the horizontal scale of the observations. While laboratory experiments of droplet freezing occur at scales usually smaller than a meter, observations of cloud glaciation from space can detect the cloud top phase over



../sect/intro/fig/approach.png

Figure 1.5: Top-down vs bottom-up approach for constraining cloud glaciation in climate models. Generally, laboratory experiments are extrapolated to the large scales in climate models, while our approach uses satellite observations to determine how droplet freezing should behave in the model.

several hundred meters. Thus, designing a top-down approach for constraining cloud glaciation with global observations could help in evaluating the current bottom-up approach and ensure that the large scale model representation of cloud glaciation is accurate.

1.4 Approach: Constraining dust-driven immersion freezing in climate models using spaceborne retrievals.

The main scientific goal of this dissertation is to constrain the dust-driven immersion freezing parametrization using global observations. To design a top-down approach for improving immersion freezing, we first must ensure that dust-driven cloud glaciation can be observed on a global scale. Therefore, the first scientific question of this dissertation is whether a causal relationship can be found between dust aerosol and cloud-top-phase as observed from spaceborne retrievals. This question eventually leads to the second question of the dissertation: How can we quantify this correlation accurately on the large scale? Finally, we study how this quantification of cloud glaciation on the large scale can constrain droplet freezing parameterization in a climate model.

To quantify cloud-phase and aerosol loading on a global scale, we rely on spaceborne retrievals of cloud-phase and aerosol optical depth. To assess the cloud-top-phase globally, we use a cloud product based on a spaceborne lidar instrument (Y. Hu et al., 2009; Chepfer et al., 2010; Cesana & Chepfer, 2013; Cesana et al., 2015; Choi et al., 2010) and two cloud products that use the synergy between multiple spaceborne instruments (see Sect. 3.2.1). The first of these synergies uses a spaceborne radar and lidar (Ceccaldi et al., 2013; Delanoë & Hogan, 2010; Mioche et al., 2014), while the second uses a spaceborne radiometer and polarimeter (Riedi et al., 2010). To compensate for the lack of reliable spaceborne retrievals of meteorological conditions and profiles of dust concentrations, we use atmospheric reanalyses — which combine observations

and modelling — to estimate meteorological conditions (Dee et al., 2011) and aerosol conditions (Eskes et al., 2015; Inness et al., 2019, see Sect. 2.2.1).

To simulate dust-driven cloud glaciation globally, we use a climate model including immersion freezing and a satellite simulator. We use the state-of-the art aerosol-climate model ECHAM(v6.3.0)-HAM(v2.3) to simulate dust concentrations (Koffi et al., 2016; Tegen et al., 2019) and their effect on clouds (Neubauer et al., 2019), considering size and number of hydrometeors (Dietlicher et al., 2018; H. Morrison & Milbrandt, 2015, see Sect. 4.2.1). For immersion freezing, we use a scheme based on wind-tunnel experiments (Lohmann & Diehl, 2006; Lohmann et al., 2007; Hoose et al., 2008) and an alternative scheme based on cloud chamber experiments (Ickes et al., 2017; Ickes, 2015; Connolly et al., 2009; Huang et al., 2018, see Sect. 4.2.3). Finally, we simulate how the modelled clouds would be observed from space (Bodas-Salcedo et al., 2011, see Sect. 4.2.2).

In this dissertation, we show that dust-driven cloud glaciation can be detected and quantified on the global scale and that this quantification can be used to make immersion freezing more realistic in climate models. In chapter 2 (Villanueva et al., 2020), we find that there is a correlation between dust and cloud ice, which can be observed on a global-scale, suggesting that dust-driven cloud glaciation plays a major role in cloud-phase variability. This correlation persists after considering potential confounding meteorological variables, which increases the confidence in a causal relationship between dust and cloud ice. In chapter 3 (Villanueva, Senf, & Tegen, 2021), we find that this dust-driven cloud glaciation can be quantified using the hemispheric and seasonal contrast of cloud-phase observed from space. The quantification is found to vary between retrieval methods, which is solved by combining several cloud products from different spaceborne instruments. Finally, in chapter 4 (Villanueva, Neubauer, et al., 2021), we use this quantification to constrain dust-driven immersion freezing in a climate model. We find that by increasing dust INP efficiency the model agrees better with observations, suggesting a previous misrepresentation in the simulated pathway to cloud glaciation.

Chapter 2

The day-to-day co-variability between mineral dust and cloud glaciation: A proxy for heterogeneous freezing*

Despite decades of study, the role of dust aerosol in cloud glaciation is still unclear. From space, we can observe whether a cloud is composed of liquid or ice (cloud-phase) and can detect the presence of dust particles. Using this information, we find a temporal correlation between dust aerosol and cloud phase within daily averages at the extratropics. This temporal correlation persists after considering potential co-variant meteorological variables. Moreover, the correlation at the day-to-day scale agrees with previously found spatio-temporal correlations between dust and cloud ice at the inter-hemispheric, regional, and seasonal scale. As a result, our findings support a line of evidence that has repeatedly corroborated a causal relationship between dust aerosol and cloud ice.

*Published as: Villanueva, D., Heinold, B., Seifert, P., Deneke, H., Radenz, M., and Tegen, I.: The day-to-day co-variability between mineral dust and cloud glaciation: a proxy for heterogeneous freezing, *Atmospheric Chemistry and Physics*, 20, 2177–2199. doi: 10.5194/acp-20-2177-2020.

2.1 Introduction

Aerosol-cloud interactions affect the Earth’s climate through different mechanisms. These include impacts of aerosol particles on cloud glaciation that subsequently influence the clouds’ thermodynamic phase, albedo, lifetime and precipitation. Specifically, there is growing evidence for a role of mineral dust aerosol (or of ice-nucleating particles correlated to dust aerosol) in influencing heterogeneous cloud ice formation on a global scale (Boose et al., 2016; Kanitz et al., 2011; Seifert et al., 2010; Tan et al., 2014; Vergara-Temprado et al., 2017; Zhang et al., 2018). Cloud droplets can freeze heterogeneously between 0°C and -42°C after interacting with Ice Nucleating Particles (INP) or already existing ice particles (Hoose & Möhler, 2012). It has been shown that specific aerosol types such as mineral dust and biogenic particles can act efficiently as INP already at temperatures between -10°C and -20°C (Atkinson et al., 2013). Mineral dust aerosol is emitted from arid regions, mainly from the Saharan and Asian deserts. Despite this, several dust sources exist at the Southern mid-latitudes (e.g., Patagonia, South Africa, and Australia) and simulations show that long-range transport of dust, although sporadic, can result in considerable dust concentrations even in remote areas (Albani et al., 2012; Johnson et al., 2011; F. Li et al., 2008; Vergara-Temprado et al., 2017). Mineral dust aerosol is therefore suspected to be a principal contributor to the atmospheric INP reservoir, especially in the Northern Hemisphere, where the mixing-ratio of dust aerosol is typically one to two orders of magnitude larger than in the Southern Hemisphere (Vergara-Temprado et al., 2018).

The dust occurrence-frequency retrieved from spaceborne instruments like the Cloud-Aerosol Lidar with Orthogonal Polarization (CALIOP; Y. Wu et al., 2014) has been previously used to assess the spatial correlation between dust and cloud thermodynamic phase (Choi et al., 2010; J. Li et al., 2017; Tan et al., 2014). Two main problems arise from this approach. First, lidar instruments cannot detect aerosol within and below thick clouds. Second, low dust concentrations usually fall below the lower detection limit of CALIOP. The Aerosol Robotic Network (AERONET; Dubovik et al., 2000), a network of ground-based remote sensing stations, has been used to evaluate and validate the dust retrievals from CALIOP. The stations from the AERONET mission use sun photometers to measure the spectrum of the solar irradiance and sky radiance to determine the atmospheric Aerosol Optical Thickness (AOT). It has been shown that the CALIOP level 2 data misses about half of the dust aerosol events detected by AERONET when the AOT is less than 0.05 (Toth et al., 2018). However, dust loadings simulated by state-of-the-art models show that most of the regions in the Southern Hemisphere have an annual mean AOT lower than 0.01 (Ridley et al., 2016).

Ice particles and cloud droplets may coexist in a so-called mixed phase state (Korolev et al., 2017). Shallow mixed-phase clouds with a liquid-dominated cloud top and ice virgae beneath are very frequent (Zhang et al., 2010) and are generally observed down to temperatures of -25°C (Ansmann et al., 2008; De Boer et al., 2011; Westbrook & Illingworth, 2011). However, ground-based and satellite retrievals are not yet able to accurately estimate the mass ratio of the cloud liquid and ice phase, speciall in these liquid-dominated cloud top layers. Therefore,

the Frequency Phase Ratio (FPR) is often used instead (Cesana et al., 2015; Cesana & Chepfer, 2013; Y. Hu et al., 2010). For satellite retrievals, this is defined as the ratio of ice voxels to total cloudy voxels for a certain volume in the atmosphere. Because most retrievals classify the cloud thermodynamic phase either as pure ice or pure supercooled liquid, the average of the FPR represents the ratio of glaciated clouds with respect to total cloud occurrence. Therefore, the FPR should not be confused with the ice-to-liquid mass ratio within a cloud volume. Cloud phase in the Northern and Southern Hemispheres has been studied in terms of FPR both by ground-based lidar (Kanitz et al., 2011) and by different spaceborne instruments (Choi et al., 2010; A. E. Morrison et al., 2011; Tan et al., 2014; Zhang et al., 2018). These studies found significant differences between the two hemispheres. In these studies, it has been suggested that such differences are related to differences in aerosol and INP concentrations. Moreover, the local FPR measured at various temperatures between 3°C and -42°C by a lidar in Central Europe over a time span of 11 years has been shown to increase for higher dust loadings (Seifert et al., 2010). Furthermore, the cloud thermodynamic phase and aerosol occurrence-frequency — both retrieved from a spaceborne lidar — are spatially correlated, especially at temperatures of around -20°C (Choi et al., 2010; Tan et al., 2014; Zhang et al., 2012, 2015). This spatial correlation has been found under different atmospheric conditions including humidity, surface temperature, vertical velocity, thermal stability and zonal wind speed (J. Li et al., 2017). However, the analysis of the temporal variability of cloud thermodynamic phase has received less attention, especially in remote areas like the Southern Ocean (Vergara-Temprado et al., 2017). Specifically, it is possible to study the temporal correlation between dust aerosol and cloud ice with a daily resolution. This kind of correlation is known as day-to-day correlation (interdaily) to avoid confusion with the intradaily variability (diurnal cycle). Additionally, a more comprehensive and quantitative assessment of the potential effect of mineral dust on cloud glaciation is currently lacking.

In this study, we use a global aerosol reanalysis together with the cloud thermodynamic phase retrievals of the CALIPSO-GOCCP (Global Climate Model Oriented Cloud Calipso Product; Cesana & Chepfer, 2013). We use a ranked correlation approach, separating the cloud phase retrievals into different deciles of dust aerosol loading. Additionally, we separate the retrievals in different humidity-stability regimes to constrain artifacts due to meteorological factors.

In Sect. 2.2, the datasets used for the study are presented. In Sect. 2.3, the processing of the datasets are described. In Sect. 2.4, the main findings are presented, including a case study, the distribution of cloud phase along temperature and latitude, and finally the day-to-day correlation between dust and cloud ice. In Sect. 2.5, the main overlaps and differences with respect to previous findings are discussed and put into context with the conceptual limitations of the approach.

2.2 Data

This section presents an overview of the datasets used in this study. The cloud thermodynamic phase is obtained from the CALIPSO-GOCCP product, the aerosol information from the MACC reanalysis, and the large-scale meteorological conditions from the ERA-Interim reanalysis.

2.2.1 CALIPSO-GOCCP

The CALIPSO-GOCCP v.3.0 product (Cesana & Chepfer, 2013) uses the Attenuated Total Backscatter (ATB), the molecular ATB (ATB_{mol}) and the cross-polarized ATB from CALIOP at 532 nm wavelength to detect cloudy voxels. The lidar has a horizontal resolution of 333 m and a vertical resolution of 30 m, however, the cloud properties in the CALIPSO-GOCCP product are retrieved at a vertical resolution of 480 m. The nadir angle of CALIOP was increased from 0.3° to 3° in November 2007 to reduce specular returns from horizontally oriented ice crystals. In the product, cloudy voxels — of 480 m height — are defined as voxels with a scattering ratio higher than 5 ($SR = ATB/ATB_{\text{mol}} > 5$). Then, the cloud volume fraction at each level is defined as the ratio of cloudy to total voxels within a $2^\circ \times 2^\circ \times 480$ m volume gridbox. The product uses the depolarization ratio of the retrieved signal components to make a decision on cloud-phase (ICE or LIQUID). The decision is based on an empirical threshold for the depolarization ratio of ice particles and is made for each cloudy voxel. From this information, the FPR is calculated as the ratio of ice voxels to the total number of voxels within each $2^\circ \times 2^\circ \times 480$ m volume gridbox. Instead of the 480 m levels, we use the temperature levels of the CALIPSO-GOCCP product, which uses 3 K temperature bins as a vertical coordinate. In this case, the temperature profiles are obtained from the Modern Era Retrospective-analysis for Research and Applications (MERRA; Bosilovich et al., 2011) reanalysis.

2.2.2 MACC and ERA-Interim reanalyses

The Monitoring Atmospheric Composition and Climate reanalysis (MACC; Eskes et al., 2015) is based on Integrated Forecast System (IFS) of the European Center for Medium Range Weather Forecasting (ECMWF) and simulates the emission, transport, and deposition of various aerosol species and trace gases with an output resolution of $1.125^\circ \times 1.125^\circ$ and 60 vertical levels. In this study, we use the dust mixing-ratio and large-scale vertical velocity from the daily MACC reanalysis product on model levels provided by the ECMWF. Additionally, the Relative Humidity (RH) from the ERA-Interim reanalysis daily product (Dee et al., 2011) is used in Sect. 2.5. The cloud properties in the MACC reanalysis are derived from the ECMWF Integrated forecast system (IFS Cycle 36r1 4D-Var). This atmospheric model is analogous to the one used in the ERA-Interim reanalysis (IFS Cycle 31r2 4D-Var). At the time of this study, the new generation of reanalysis based on IFS Cycle 41r was not yet publicly available. However, it is expected that future studies will use the new CAMS (Copernicus Atmosphere Monitoring Service) and ERA5 reanalysis instead of the MACC and Era-Interim reanalysis.

The averaged meteorological parameters (RH, large-scale updraft and isotherm height) used in Sect. 2.5 were weighted by the cloud volume fraction retrieved by the CALIPSO-GOCCP

product (see Sect. 2.2.1). The length is the segment of the satellite track crossing a given gridbox, and the height interval corresponds to each temperature bin (3 K) in this study. More details on the spatiotemporal variability of the cloud volume fraction can be found in the Supporting Information (2.S8).

The dust emission in the MACC model is parameterized as a function of the 10-m wind, vegetation, soil moisture and surface albedo. The dust loadings are corrected by the assimilation of the total column AOT at 550 nm retrieved from the MODIS instrument onboard NASA’s Aqua and Terra satellites. Dry and wet deposition of dust are simulated, as well as in-cloud and below-cloud removal. The freezing efficiency of INPs depends mainly on their surface area concentration (Atkinson et al., 2013; Hartmann et al., 2016; Murray et al., 2011; Niedermeier et al., 2011, 2015; Price et al., 2018).

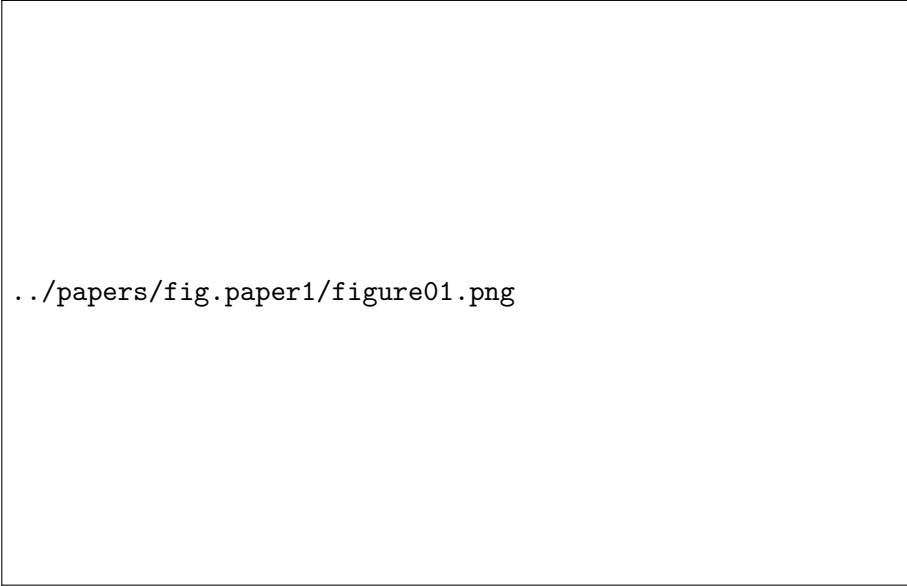
In the MACC reanalysis, dust aerosols are represented by three size bins, with size limits of 0.03, 0.55, 0.9 and 20 μm diameter. In this work, we define the size bin between 0.03 and 0.55 μm as fine-mode dust. The number concentration of dust aerosol is generally dominated by fine-mode dust (particle diameter $< 0.5 \mu\text{m}$). However, the surface area concentration is often determined by both fine and coarse (particle diameter $> 1 \mu\text{m}$) dust particles (Mahowald et al., 2014). Moreover, the atmospheric lifetime of fine-mode dust is longer than that of coarse-mode dust due to the lower dry deposition rates of finer particles (Mahowald et al., 2014; Seinfeld & Pandis, 1998). Because the fine mode contributes to both the number and surface area concentration, it is used as a proxy for the concentration of dust INP. Although mostly focused on the Northern Hemisphere, several studies have evaluated the simulated dust mixing-ratios from the MACC reanalysis with observations. A mean bias of 25% was found between MACC and LIVAS, a dust product based on CALIPSO observations over Europe, northern Africa and Middle East (Georgoulias et al., 2018). Additionally, the correlation between MACC and AERONET was found to range from 0.6 over the Sahara and Sahel to 0.8 over typical regions of dust transport (Cuevas et al., 2015). Using shipborne measurements of long-range dust transport, it was found that the MACC model significantly overestimates the fine-dust fraction compared to observations (Ansmann et al., 2017).

2.3 Methods

In this section, the different processing steps of the datasets presented in Sect. 2.2 is described. Fig. 2.1 presents a flow chart of this processing and a roadmap for the following subsections.

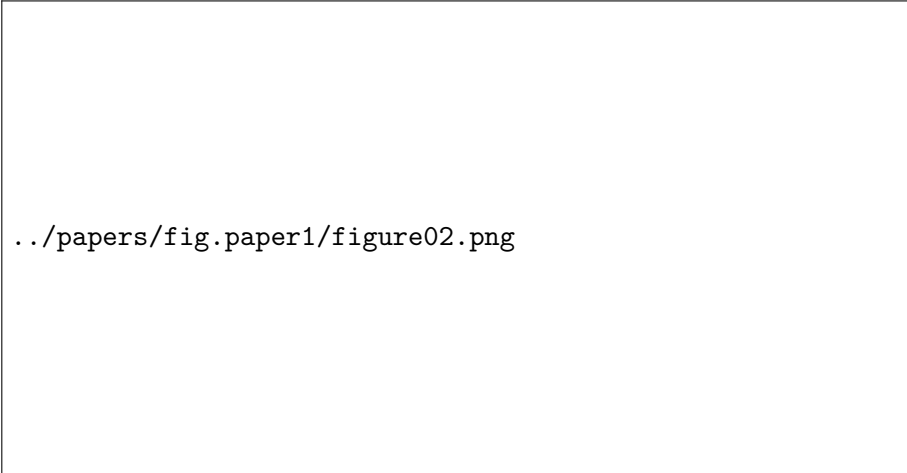
2.3.1 Selection of cloud profiles

In order to exclude the effects of the scattering of sunlight on the cloud phase detection from the CALIOP lidar signal, only night-time retrievals were used. Including convective clouds — as retrieved by the 2B-CLDCLASS product (see Appendix) — does not introduce a significant bias on the results. This low sensitivity to convective clouds is mainly due to the low area fraction represented by such clouds, especially in the mixed-phase regime at the mid-latitudes



../papers/fig.paper1/figure01.png

Figure 2.1: Flow chart showing the processing steps starting from the raw data (satellite retrievals and model reanalysis) to the dataset used for the analysis.



../papers/fig.paper1/figure02.png

Figure 2.2: Seasonal, day-to-day and day-to-day decile concept as used in this study. For this example, the day-to-day analysis of May contains 124 daily datapoints. In step (a) to (b), only the daily values for one month of the year (May) are selected. In step (b) to (c), these daily values are sorted into 10 different deciles. In step (c) to (d), the average dust mixing-ratio and ice frequency for each decile is calculated.

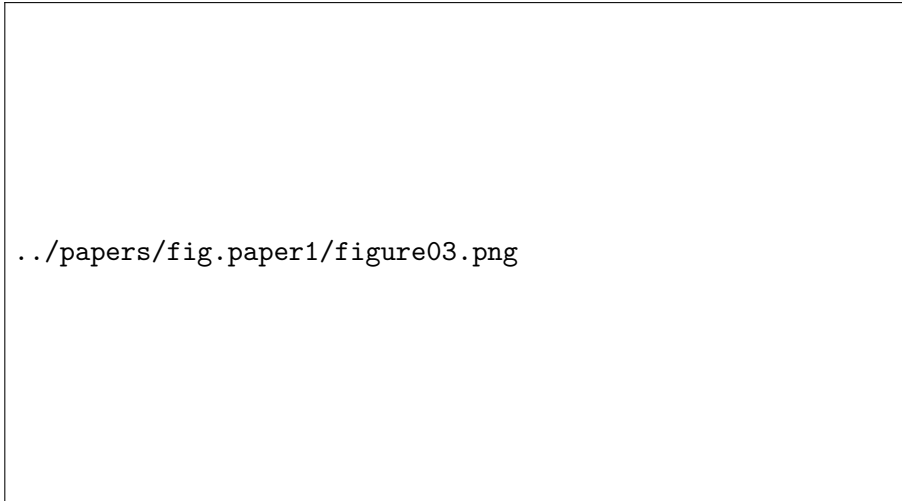


Figure 2.3: Sample size of cloud phase (CALIPSO-GOCCP) of each latitude band for -15°C (range -21°C to 9°C) and -30°C (range -36°C to -24°C) for the period 2007-2010. Each count corresponds to a $1.875^{\circ}\times 30^{\circ}$ gridbox in a 3 K temperature bin at a specific month of the year and inside a specific dust decile. The theoretical maximal sample size for each latitude band is 5760 for a 12 K temperature range.

(less than 5%). Similarly, precipitating clouds had little impact on the results.

2.3.2 Regridding and rebinning

The cloud thermodynamic phase is mainly a function of temperature. Therefore, temperature bins of 3 K each were used as a vertical coordinate throughout the study to constrain the variability of cloud phase. For the MACC and ERA-Interim reanalysis, we rebin the model levels into 3 K intervals, to match the vertical resolution of the CALIPSO-GOCCP product.

For each product, the latitude x longitude space was regridded using the nearest-neighbour method. We regridded the dataset first into a Gaussian T63 grid, then aggregated every 16 gridboxes along the longitude ($1.875^{\circ}\times 30^{\circ}$; latitude longitude gridboxes) to better fill the horizontal gaps between the satellite orbits. The Gaussian T63 grid is commonly used in Global Climate Models (Randall et al., 2007). It also facilitates comparisons with global simulations of cloud thermodynamic phase. In Sect. 2.4.4 and onwards, zonally averaged latitude bands of $30^{\circ}\times 360^{\circ}$ are used to allow a direct comparison with previous studies (Zhang et al., 2018).

2.3.3 Meteorological regimes

Dust aerosol can produce or be accompanied by changes in atmospheric stability and humidity. To disentangle such effects, we constrain the cloud environment using the air relative humidity with respect to liquid and the tropospheric static stability. Depending on the isotherm to be studied, we use the lower troposphere static stability (LTSS) or the upper troposphere static stability (UTSS). These parameters are defined as:

$$\text{LTSS} = T_{700} \cdot \left[\frac{1000}{700} \right]^{R/C_p} - T_{sfc} \cdot \left[\frac{1000}{p_{sfc}} \right]^{R/C_p} \quad (2.1)$$

$$\text{UTSS} = T_{350} \cdot \left[\frac{1000}{350} \right]^{R/C_p} - T_{500} \cdot \left[\frac{1000}{p_{500}} \right]^{R/C_p} \quad (2.2)$$

With T_x and P_x the temperature and pressure at the surface or at x hPa using the pressure levels of the ERA-Interim reanalysis. R is the gas constant and C_p the specific heat capacity of air (Klein & Hartmann, 1993). The static stability (see equations 2.1 and 2.2) is defined as the difference in potential temperature between two pressure levels (Klein & Hartmann, 1993). It represents the gravitational resistance of an atmospheric column to vertical motions. Such vertical motions are traduced in a temperature change rate within the air parcel. Therefore, the static stability can have an important impact on the heterogeneous freezing rates, especially on immersion freezing. We note that the dynamic component of the atmospheric stability is not included in the static stability. Especially in the upper troposphere, atmospheric gravity waves occurring during stable thermal conditions may also result in vertical motions affecting ice production. The static stability and relative humidity are obtained from the ERA-Interim reanalysis.

2.3.4 Classification of dust loads and day-to-day correlation

In contrast to previous studies, in this work we want to isolate the day-to-day correlation between dust aerosol and cloud phase. In order to exclude the spatial component of the correlation, the complete time-span 2007-2010 was used to assess the daily correlation between the MACC dust mixing-ratio and the CALIPSO-GOCCP cloud phase. This correlation was done independently for each volume gridbox — each constrained in latitude, longitude and temperature.

We also need to exclude the seasonal component of the temporal correlation. For this purpose, we process each month of the year independently. This is done as a multiyear selection (e.g., January containing Jan'07, Jan'08, Jan'09 and Jan'10). See Fig. 2.2a-b.

The dust mixing-ratio density distribution is heavily right-skewed, while the cloud phase follows mostly a binary distribution. Because of this non-normality, a typical correlation approach like the Pearson's correlation coefficient will not reflect the genuine relationship between both variables (Hauke & Kossowski, 2011). Therefore, we use a rank correlation approach using the temporal quantiles of the dust loading. Specifically, we use the time deciles of the MACC dust mixing-ratio to sort the daily values of cloud phase independently at each volume gridbox. As a result, each cloud phase value is associated with a specific daily dust rank: from exceptionally dust-free days ("1" for the lowest decile) to exceptionally dusty days ("10" for the highest decile). This step can be understood as sorting of the daily values (See Fig. 2.2b-c), where the neighbouring days are reordered and the timeline is lost. Finally, we average the daily values of dust loading and cloud phase inside each dust decile (See Fig. 2.2c-d). The resulting field contains one extra dimension for each volume gridbox (month, dust decile, temperature, latitude, longitude). Fig. 2.2 presents a visualization of this process.

2.3.5 Data availability and averaging order

The day-to-day correlation approach relies strongly on the available sample size. For small sample sizes, only a few retrievals (daily means within a volume gridbox) can be found for a given dust decile. In this case, the average FPR may still be non-normally distributed, introducing a larger standard deviation. Within a 12 K range, each zonally averaged latitude bin ($1.875^\circ \times 360^\circ$) contains about 1500 to 2000 observational datapoints in the mid-latitudes and about 500 to 1500 datapoints in the high-latitudes (Fig. 2.3). The smallest sample size was found for the high southern latitudes, where it drops down to about 400 at -15°C , which corresponds to 7% of the total possible sample size). In this case, many $1.875^\circ \times 1.875^\circ$ volume gridboxes contain only one retrieval for a given dust decile. Only after aggregating such gridboxes into a $1.875^\circ \times 30^\circ$ resolution, enough retrievals are averaged to obtain a normally distributed variable. Potential reasons for missing data are:

- The satellite swaths (orbits) produce a different density of retrieved profiles at different latitudes.
- Using only night-time data, the sample size in the meteorological summertime (shorter nights) is lower.
- The cloud phase retrievals are less frequent for seasons, regions and heights with low cloud cover (See Supporting Information 2.S8).
- At high latitudes, relatively warm temperatures (e.g., -15°C) exceeding the surface temperature can be found, and therefore no information is available for such temperatures (e.g., over Antarctica in winter).

The averaging order of the dimensions was defined — from first to last — as longitude, month, decile, latitude, temperature. This choice prevents artefacts resulting from too many missing values. Latitude and temperature are averaged last because of the higher associated correlations with cloud phase (Sect. 2.4.2–2.4.3 of this study; Choi et al., 2010; Tan et al., 2014). Each $1.875^\circ \times 30^\circ$ of the newly defined gridboxes contains on average 100 to 200 datapoints at -15°C (within a 12 K range) in the mid-latitudes. Meanwhile, in the subtropics and the high latitudes, the sample size is much more heterogeneously distributed. Near the poles and in subsidence regions, it can drop below 50 datapoints. A detailed view of the spatiotemporal distribution of the sample size for stratiform clouds can be found in the Supporting Information (2.S14). In Sect. 2.4.1, the adjusted ice volume fraction

$$\text{FPR}^* = (2 \cdot \text{FPR} - 1) \cdot cvf \quad (2.3)$$

is used instead of the traditional FPR, with cvf the cloud volume fraction obtained from the GOCCP product. The adjusted FPR^* helps to visualize the cloud thermodynamic phase of significant clouds — with high cvf — in the retrieval. This alternative is only used in the case study to aid the visualization of the cloud ice and liquid.

2.4 Results

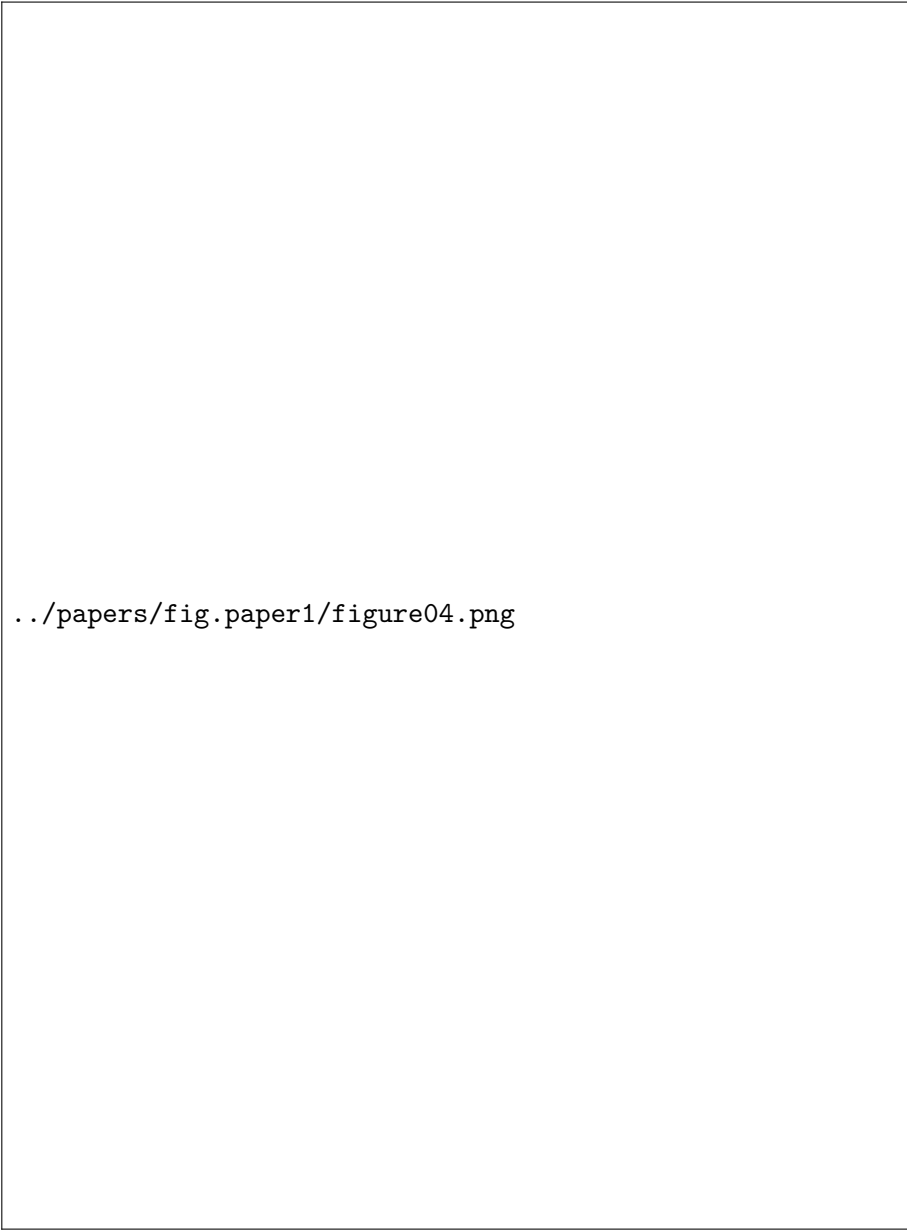
2.4.1 Case study

This section seeks a better understanding of the ice-to-liquid ratio retrieved in the CALIPSO-GOCCP product. We provide a detailed case study of a stratiform cloud scenario. In this scenario, four stratiform cloud types from the CloudSat classification are included: stratocumulus (low-level clouds), altostratus and altocumulus (mid-level clouds), and cirrus (high-level clouds). Although not present in the case study, Nimbostratus are included in the analysis of cloud phase as well and are particularly important in the high latitudes. Stratus clouds are defined for temperatures above 0°C ; therefore, they are not relevant for this study. Finally, the horizontal extension of cumulus and deep-convective clouds is very low compared to the stratiform clouds and can be therefore ignored in our study, especially outside the tropics (Sassen & Wang, 2008). The A-train segment shown in Fig. 2.4 has been already chosen for a previous case study (Huang et al., 2015) due to the variety of cloud types it contains. For this segment, we separate the clouds classified as cirrus and altocumulus (Fig. 2.4a). Similarly, we can also separate altostratus and stratocumulus (Fig. 2.4b). These four cloud types are frequently thin enough to be penetrated by lidar and radar systems. Therefore they are an excellent target to study cloud glaciation processes (Bühl et al., 2016; Zhang et al., 2010). Stratiform clouds are simpler to study than convective clouds because they are affected by weaker updrafts and the microphysical evolution (i.e., ice formation) is less affected by secondary and ice multiplication effects (Westbrook & Illingworth, 2011). Fig. 2.4c shows the mixing-ratio of fine ($0.03\ \mu\text{m}$ – $0.55\ \mu\text{m}$) dust aerosol (MACC reanalysis) for the same vertical plane. As in this case study, the dust loading can vary within several orders of magnitude on the synoptical scale. On the same scale, we can usually observe clouds with different cloud phases (Fig. 2.4d). Therefore, combining many cases, it is possible to assess both the spatial and temporal correlation between both variables. This assessment may shed some light on the potential role of dust aerosol as a driver of cloud glaciation in stratiform clouds.

2.4.2 Temperature dependence

Temperature is the main factor controlling the thermodynamic phase of clouds. Mixed-phase clouds between 0°C and -25°C are usually topped by a liquid layer (Ansmann et al., 2008; De Boer et al., 2011; Westbrook & Illingworth, 2011). Below this layer, there is often a thicker layer containing ice particles. The CALIOP backscatter signal is usually already strongly attenuated at such depths and often cannot detect large ice particles. Therefore, the CALIPSO-GOCCP algorithm usually classifies the whole cloud layer as liquid (Huang et al., 2012, 2015).

Fig. 2.5 shows that the global average FPR as a function of temperature decreases roughly from 100% at -40.5°C to about 20% at -1.5°C and down to 0% at $+1.5^{\circ}\text{C}$. This temperature dependence between -42°C and 0°C is also observed for a wide range of parameterizations in global climate models (Cesana et al., 2015). This pattern can also be found in ground-based measurements (Kanitz et al., 2011), spaceborne lidar measurements (Tan et al., 2014)



../papers/fig.paper1/figure04.png

Figure 2.4: Case study 9:50 UTC Dec 14, 2010 for temperatures between -42°C and $+3^{\circ}\text{C}$. a-b) Cloud volume fraction (GOCCP) for different cloud types (CloudSat cloud classification). c) Fine dust ($0.03\text{-}0.55\ \mu\text{m}$) aerosol mixing-ratio (MACC reanalysis), note the logarithmic scale. d) Adjusted ice occurrence-frequency derived from the CALIPSO-GOCCP product. FPR*: Frequency phase ratio (ice voxels/total voxels; see Equation 2.3). White colours represent clear sky. The fields were collocated in a $1.875^{\circ}\times 1.875^{\circ}$ grid with temperature bins of 3 K each.



Figure 2.5: Global ice cloud occurrence-frequency (2007-2010). The fine-mode dust mixing-ratio from the MACC reanalysis corresponds to the range 0.03-0.55 μm and is presented on a logarithmic scale on the right vertical axis. Each temperature bin spans 3 K. The vertical bars show the mean day-to-day standard deviation between different fine-mode dust deciles.

and aircraft measurements (McCoy et al., 2016). Additionally, the average fine-mode dust mixing-ratio is also shown in Fig. 2.5. At the height of the 0°C isotherm, the mixing-ratio is on average higher than at the -42°C isotherm (note the logarithmic right y-axis). This reflects the fact that, on average, dust mixing-ratios tend to be higher near the dust sources at the surface. However, this does not imply any general relationship between dust and temperature. Moreover, instant vertical profiles of dust loading and temperature may differ greatly from this average, especially in the long-range transport of dust plumes.

2.4.3 Latitude dependence

For both temperature ranges shown in Fig. 2.6 the absolute maximum of FPR is located near the Equator (85% at -30°C and 44% at -15°C). These maxima are probably associated with the enhanced homogeneous freezing in the tropics at temperatures below -40°C and the resulting downward transport of cloud ice — also known as ice detrainment. Similarly, the minima are observed towards the high latitudes. At -30°C , the FPR has two local maxima with values of 76% and 84% near 39°S and 39°N , respectively. At -30°C , the FPR is higher in the Northern Hemisphere than in the Southern Hemisphere, in particular for the high latitudes. This higher FPR coincides with the higher average dust mixing-ratio in the Northern Hemisphere. Such positive spatial correlations between FPR and dust aerosol have been already pointed out using the dust occurrence-frequency derived from CALIOP (Choi et al., 2010; Tan et al., 2014; Zhang et al., 2012).

../papers/fig.paper1/figure06.png

Figure 2.6: Zonal mean of stratiform cloud ice occurrence-frequency for (a) -30°C (range -36°C to -24°C) and (b) -15°C (range -21°C to -9°C) averaged over the period 2007-2010. Each datapoint corresponds to a zonal band of 11.25° width. The average fine-mode dust mixing-ratio of each band is also shown on the right vertical axis (note the logarithmic scale). The average large-scale vertical velocity (updraft) from the MACC reanalysis is also shown (cyan axis on the left of each plot). The vertical bars show the mean day-to-day standard deviation between different fine-mode dust deciles. The curves for dust and updraft are slightly shifted left and right, respectively, to fit all vertical bars.

../papers/fig.paper1/figure07.png


Figure 2.7: Probability histogram at -22°C (range -27°C to -18°C) for 2007 for different conditions of relative humidity against (a) upper troposphere static stability and (b) lower troposphere static stability. All-sky gridboxes are included for the entire globe. The values for relative humidity are taken from the ERA-Interim dataset and the static stability is calculated from the ERA-Interim pressure levels. The magenta and black boxes represent the regimes used in the study.

At -15°C , in the southern high latitudes a local minimum in FPR near 73°S is followed by a steep increase at 84°S . The larger standard deviation in these latitudes is possibly a result of the low sample size in the region, as mentioned in Sect. 2.3. However, the higher FPR in the southern than in the northern polar region is consistent with the fraction of ice clouds reported previously in the literature at -20°C (J. Li et al., 2017). On the other hand, it has been shown that the orographic forcing in Antarctica can lead to high ice water contents for maritime air intrusions (Scott & Lubin, 2016). In other words, maritime air intrusions associated with higher temperatures, higher concentrations of INP and stronger vertical motions could explain the observed pattern in the southern polar regions. However, the low sample size near the South Pole (Fig. 2.3 and Supporting Information 2.S14-b) and the low altitude of the -15°C isotherm (2.S12-b) result in a lower confidence in the results for this region. For example, at -15°C , the zonal standard deviation of the FPR significantly increases from 60°S towards the South Pole — from about ± 0.08 to ± 0.16 in Fig. 2.6a — at the same time that the sample size decreases from 2200 to 300 (Fig. 2.3).

For the clouds studied, the time-averaged large-scale vertical velocity (from the MACC reanalysis, shown in Fig. 2.6) is regionally correlated with the FPR at -15°C . The Pearson correlation coefficient was 0.47 using zonal averages and 0.31 using the $30^{\circ} \times 1.875^{\circ}$ gridbox averages. Moreover, in another study, the spatial correlation between large-scale updraft velocity at 500 hPa was also found to be positively correlated (spatially) to the occurrence-frequency of ice clouds at -20°C (J. Li et al., 2017). In other words, both the dust mixing-ratio and the large-scale vertical velocity appear to be to some extent correlated (spatially) to the FPR. There are some plausible explanations for this correlation:

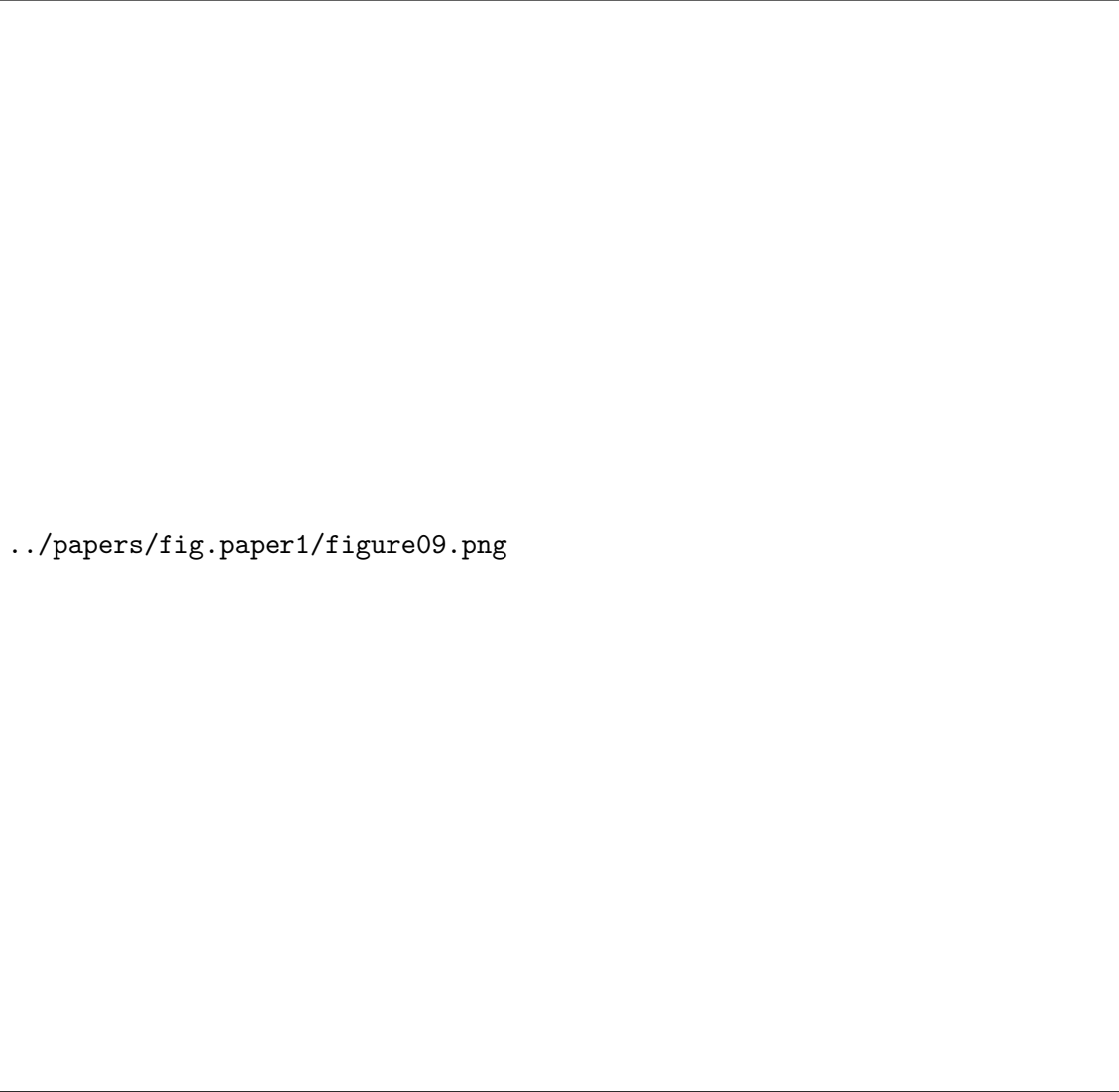
- The spatial correlation can be a result of an enhanced transport of water vapour to higher levels at temperatures below -40°C and the subsequent sedimentation of ice crystals from the homogeneous regime (Convective detrainment of ice).
- The updrafts are associated with higher availability of INP at the cloud level (from below the cloud), and the effect is large enough to mask the enhanced droplet growth typically associated with updrafts.
- The updrafts enhance a certain type of heterogeneous nucleation requiring saturation over liquid water (e.g., immersion freezing). Updrafts generate a local adiabatic cooling, possibly activating INPs that may not have been active before at higher temperatures.

To the authors' knowledge, there is currently no observational constrain to the source of cloud ice in the mixed-phase regime. Namely, the frequency of ice clouds between 0°C and -42°C may be dominated by either convective ice detrainment or by in-situ freezing of cloud droplets. Overall, the relative contribution of heterogeneous and homogeneous freezing — and the different INP types — is still a matter of debate (Dietlicher et al., 2018; Barahona et al., 2017; Sullivan et al., 2016).



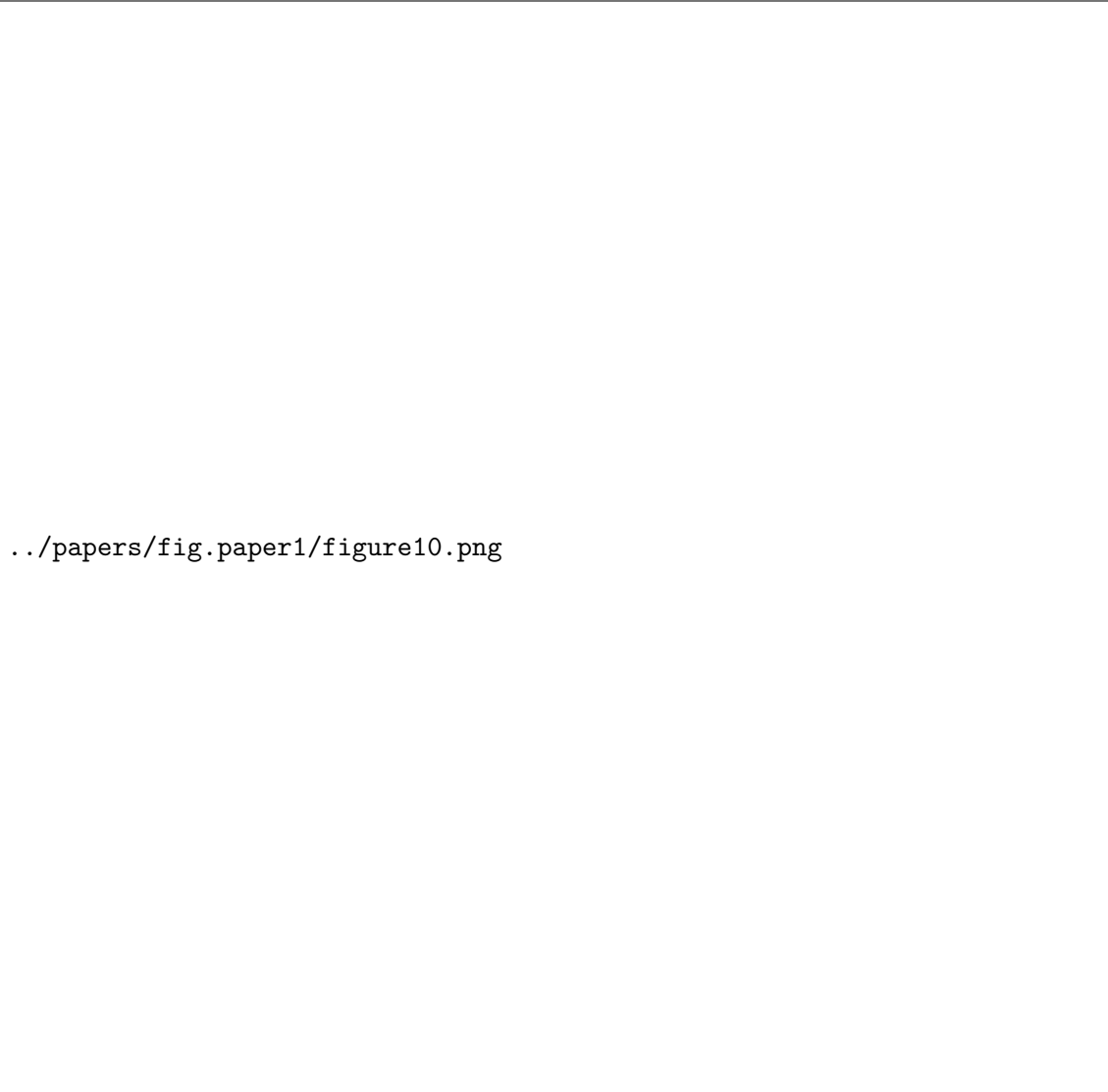
../papers/fig.paper1/figure08.png

Figure 2.8: Average cloud phase (GOCCP) for the mid-latitude and high-latitude bands averaged between -21°C and -9°C in the period 2007-2010 for different regimes of relative humidity (a,c low RH ; b,c high RH) and lower tropospheric static stability (a,b high LTSS ; c,d low LTSS). The horizontal axis corresponds to the different time deciles (day-to-day variability) of fine-mode dust mixing-ratio (MACC) calculated for each 3 K temperature bin and gridbox ($1.875^{\circ}\times 30^{\circ}$) and averaged along each 12 K temperature range and latitude band. The vertical bars are positioned at each dust decile and show the mean zonal standard deviation within each latitude band.



`../papers/fig.paper1/figure09.png`

Figure 2.9: Same as Fig. 2.8 but averaged from -36°C to -24°C and using the upper tropospheric static stability (UTSS).



`../papers/fig.paper1/figure10.png`

Figure 2.10: Same as Fig. 2.8 but averaged from -27°C to -18°C .

2.4.4 Constraining the influence of static stability and humidity on the dust-cloud-phase relationship

In the following sections, the temporal correlation between mineral dust mixing-ratio and cloud ice occurrence-frequency is referred to as the dust-cloud-phase relationship. To study this relationship, we classify the retrievals into different weather regimes to constrain the meteorological influence. The resulting dust-cloud-phase relationship for different regimes may offer a good insight into the processes underlying the dust-cloud-phase relationship. Particularly, how heterogeneous freezing by dust aerosol may affect the cloud thermodynamic phase on a day-to-day time scale.

In other words, to extract the specific influence of mineral dust on cloud glaciation, it is necessary to identify and constrain relevant meteorological confounding factors (Gryspeerd et al., 2016). The atmospheric relative humidity and static stability are good candidates for such a confounding factor (Zamora et al., 2018). Both are correlated with the transport of mineral dust and vary between different cloud regimes. Additionally, relative humidity is, next to the temperature, one of the main factors in the initiation of ice nucleation in laboratory studies (Hoose & Möhler, 2012; Welti et al., 2009).

The effect of humidity and static stability on ice production is not straightforward. In general, moist and unstable conditions are associated with enhanced lifting of air that likely causes nucleation of hydrometeors. Between 0°C and -40°C , the supersaturation of water vapour over liquid enhances the liquid formation. However, the depositional growth of ice is rather inefficient within strong updrafts (Korolev et al., 2017). At temperatures below -40°C , the ice production due to deposition and homogeneous nucleation dominate. The ice particles aloft can result in a higher occurrence of cloud ice in the mixed-phase regime below due to ice sedimentation. To constrain both the atmospheric stability and humidity, a subset of the data must be found within a narrow range of these variables. At the same time, enough data points must still be available to assess the dust-cloud-phase relationship. For this purpose, we use a probability histogram to define the regime bounds such that at least 10% of the data is included in each regime (see Fig. 2.7). For the relative humidity, the bounds are defined at 60, 70 and 80%, for the LTSS at 10, 15 and 20 K, and for the UTSS at 4, 6 and 8 K. The fraction of data inside each regime corresponds to the integral of the probability density within the regime bounds. For example, if the probability density between 4–6 K and 70–80% is 0.01, then 20% of the data is contained between these bounds. The magenta boxes in Fig. 2.7 represent the different stability-humidity regimes used for the lower and upper troposphere.

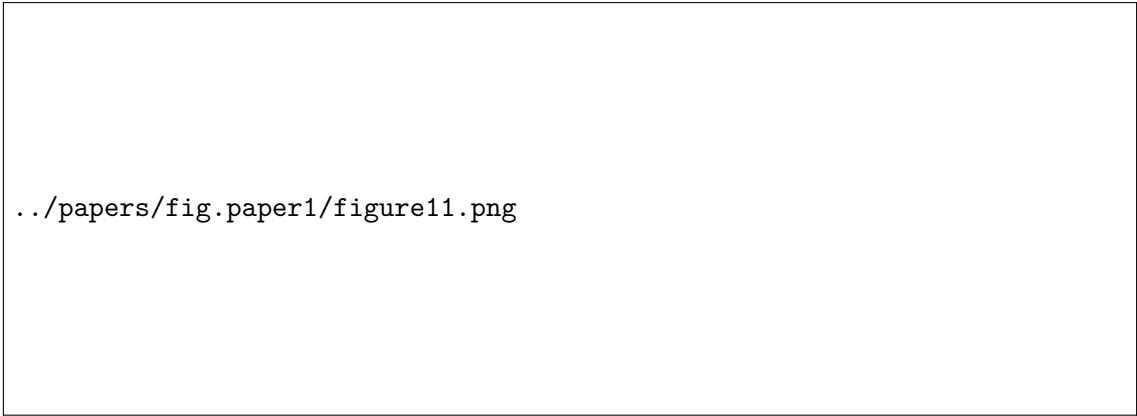
For dust mixing-ratios between 0.1 and $2.0 \mu\text{g kg}^{-1}$ at -15°C , the dust-cloud-phase curve in both mid-latitudes follows a similar logarithmic increase of cloud ice occurrence-frequency of about +6% for low-LTSS and +4% for high-LTSS conditions (see Fig. 2.8). After analysing 11 years of ground-based lidar measurements in Leipzig, Seifert et al. (2010) reported a slightly higher increase by about +10% between -10°C and -20°C for dust concentrations between 0.001 to $2 \mu\text{g m}^{-3}$ (note the different units). In our results at -15°C , the cloud ice occurrence-

frequency tends to be higher for higher relative humidity, and the LTSS seems to have a major effect on the dust-cloud-phase relationship. For high-LTSS conditions (Fig. 2.8a-b), a positive dust-cloud-phase correlation can be observed at all four latitude bands. The slope is similar for the Northern and Southern Hemisphere latitudes and for the mid- and high latitudes.

At high LTSS in the high-latitudes, the range of ice occurrence-frequency values is higher than for the mid-latitudes and small increases in dust mixing-ratio are associated with a strong increase in cloud ice occurrence-frequency. For the high-LTSS regime, the ice occurrence-frequency in the high southern latitudes increases by +8%. In contrast, at mid-latitudes the increase is only about +4%. In both mid- and high latitudes, the cloud ice occurrence-frequency for the same dust mixing-ratio is about +2% to +8% higher in the Southern than in the Northern Hemisphere. This contrast could point to a factor — other than dust aerosol — causing an increased ice occurrence-frequency in the Southern Hemisphere. The contrast could also suggest a potential difference in the sensitivity of cloud glaciation to mineral dust between hemispheres. In the high-RH regime, the difference between Northern and Southern Hemisphere is reduced, as well as the standard deviation of the FPR. This reduction may be due to the higher sample size density in the high-RH regime. For the low-LTSS regime (Fig. 2.8c-d), the cloud thermodynamic phase in the high-latitudes remains mostly constant for increasing dust mixing-ratios. For the same regime, the maximum FPR in the southern mid-latitudes is similar to the minimum in the northern mid-latitudes. This agreement suggests a more consistent sensitivity of cloud glaciation to mineral dust for unstable conditions.

At -30°C , the cloud ice occurrence-frequency in the high southern latitudes remains almost constant for increasing dust mixing-ratios (see Fig. 2.9). For the high-RH regime, the cloud ice occurrence-frequency tends to be higher than in the low-RH regime. This difference is evident for the high southern latitudes for which the cloud ice occurrence-frequency is about +4% higher at the high-RH regime. For dust mixing ratios between 0.1 and $1.5 \mu\text{g kg}^{-1}$, the cloud ice occurrence-frequency at -30°C increase by about +5%. The highest increase is found for the northern latitudes. However, the results from the southern mid-latitudes contradict the notion that the INP activity of mineral dust is of secondary importance in the Southern Hemisphere due to low dust aerosol concentrations (Burrows et al., 2013; Kanitz et al., 2011). Nevertheless, recent studies have acknowledged that the importance of mineral dust in the southern latitudes still cannot be ruled out (Vergara-Temprado et al., 2017).

At -22°C , the cloud ice occurrence-frequency is higher in the high-RH regime (Fig. 2.10), similar to the results at -15°C and -30°C . For high-UTSS conditions, the dust-cloud-phase curves are in closer agreement between the Northern and Southern Hemisphere. This coincidence suggests a similar sensitivity of cloud glaciation to mineral dust for both hemispheres. For mixing ratios between 0.01 and $1.0 \mu\text{g kg}^{-1}$ at -22°C , the ice occurrence-frequency increases by about 25% at high-UTSS conditions and by about 20% at low-UTSS conditions. From the three temperature regimes studied, at -22°C the four latitude bands show the best agreement between Northern/Southern Hemisphere and also between mid- and high-latitudes. With these



../papers/fig.paper1/figure11.png

Figure 2.11: Same as Fig. 2.8 but for a) ERA Interim relative humidity, b) ECMWF-AUX isotherm height and c) MACC large-scale vertical velocity at -15°C . The average of each variable is weighted by cloud volume fraction.

results, the dust-cloud-phase correlation may help clarify not only the day-to-day differences in cloud glaciation but also the differences between latitudes.

At all temperatures studied, higher humidity values were associated with a higher cloud ice occurrence-frequency. Additionally, for similar dust loadings, the cloud ice occurrence-frequency was found to be higher at the mid-latitudes than at the high-latitudes. However, against our expectations, for similar dust loadings the cloud ice occurrence-frequency at -15°C was higher in the Southern than in the Northern Hemisphere.

2.5 Discussion

Some studies have already suggested that the lower occurrence-frequency of cloud ice in the higher latitudes may be associated with lower INP concentrations (J. Li et al., 2017; Tan et al., 2014; Zhang et al., 2012). This hypothesis has been supported mainly by the spatial correlation between the dust relative aerosol frequency and the occurrence-frequency of ice clouds retrieved from satellite observations. However, evidence of the day-to-day co-variability between INP and cloud ice was lacking up to now. Furthermore, by studying the dust-cloud-phase relationship it is possible to extract new information about the differences in cloud glaciation at different latitudes and to connect these differences to previous studies of heterogeneous freezing. Particularly, our results may be used to evaluate our current knowledge of the global differences in the mineralogy of dust aerosol and its freezing efficiency.

2.5.1 North-South contrast

We have found that the ice occurrence-frequency can vary at different latitudes even for similar mixing-ratios of mineral dust. This variability could be explained by differences in the mineralogical composition of the mineral dust aerosol at the Southern and Northern Hemisphere. Clay minerals from the Northern Hemispheres are composed mostly of Illite and Smectite (Claquin et al., 1999). It has been suggested that the freezing efficiency of these minerals can be well

represented by the mineral Montmorillonite (Hoose et al., 2008). In contrast, the Southern clay minerals are better represented by the mineral Kaolinite (Claquin et al., 1999; Hoose et al., 2008), which is less efficient in the immersion mode. The freezing efficiencies of Kaolinite and Montmorillonite are known for both the immersion and contact freezing mode (Diehl et al., 2006; Diehl & Wurzler, 2004). Following this assumption, the immersion freezing rates at -30°C would be about 300 times higher in the Northern than in the Southern Hemisphere. This difference could explain the higher ice occurrence-frequency in the Northern Hemisphere relative to the Southern Hemisphere for similar dust mixing-ratios at -30°C .

For temperatures higher than -25°C , contact freezing starts to dominate over immersion freezing. However, between -25°C and -16°C the contact freezing efficiency is similar for Kaolinite and Montmorillonite. This balance may explain why the ice occurrence-frequency in the Northern Hemisphere is only slightly higher for similar dust mixing-ratios at -22°C . Finally, between -15°C and -4°C , the contact freezing efficiency of Montmorillonite is again higher than for Kaolinite. However, this returned contrast fails to explain the higher ice occurrence-frequency found in the Southern Hemispheres at -15°C .

Nevertheless, at such high temperatures, other dust minerals like feldspar mineral are much more efficient as ice nucleating particles than clay minerals (Atkinson et al., 2013). Moreover, it could be that the effect of such feldspar minerals dominates over the effect of clay minerals at high temperatures. Indeed, such efficient minerals are believed to deplete quickly through heterogeneous freezing. Therefore, only a few of these aerosols would reach lower temperatures. Thus, they are likely more relevant at temperatures above -20°C , where the immersion efficiency of clay minerals quickly decays (Boose et al., 2016; Broadley et al., 2012; Murray et al., 2011).

If feldspar minerals do dominate the heterogeneous freezing due to mineral dust above -20°C , then the higher cloud ice occurrence-frequency in the Southern Hemisphere may be due to a higher fraction (or higher efficiency) of feldspar minerals in the southern dust particles. Some evidence for this has been already found by comparing the immersion freezing efficiency of dust particles from different deserts worldwide (Boose et al., 2016). In these results, the immersion efficiency of dust particles lies mostly between Kaolinite and K-feldspar. The dust samples from sources in the Southern Hemisphere (Australia, Etosha and Atacama milled) have a higher freezing efficiency than most of the samples from the Northern Hemisphere sources including Saharan sources for temperatures below -24°C . Unfortunately, only four of these samples were studied for higher temperatures, between -23°C and -11°C . However, it was again a sample from the Southern Hemisphere (Atacama milled) which exhibited the highest freezing efficiency. We may assume that the higher freezing efficiency of the southern dust sources can be extrapolated to temperatures above -20°C . Then, at -15°C the higher immersion efficiency of southern mineral dust, possibly due to higher feldspar fractions, may explain the higher ice occurrence-frequency in the Southern Hemisphere. The highly efficient particles, most likely feldspar minerals, would be quickly depleted at temperatures around -15°C and

would therefore not interfere with the Kaolinite-Illite(Montmorillonite) differences at -30°C .

Furthermore, such a depletion of highly efficient INP during the transport of dust aerosol may also explain the higher ice occurrence-frequency at the mid-latitudes compared to the high-latitudes for similar mixing-ratios of mineral dust, especially at higher temperatures. The ageing (e.g., internal mixing with sulfate or “coating”) of dust particles may also reduce the freezing efficiency of dust aerosol during the transport from low to high latitudes. The hypotheses explaining the differences in the freezing behaviour of dust between the Northern and Southern Hemisphere are summarized in Table 2.1.

2.5.2 Assumptions and uncertainties

In the analysis presented above, certain assumptions were made to assess the potential effect of mineral dust on cloud thermodynamic phase. In this section, these assumptions and the uncertainties that arise from them, as well as the subsequent limitations of the resulting interpretation will be discussed.

Concerning the vertical resolutions of the different products, the choice of 3 K bins is based on the original 3 K bins of the CALIPSO-GOCCP product. Using a coarser vertical resolution (e.g., 6 K bins) would hinder the assessment of the role of dust as INP. For example, a decrease of 3 K in temperature is roughly equivalent to a fivefold increase in INP concentrations (e.g., Niemand et al., 2012). At the mid- and high-latitudes, the typical standard deviation of the day-to-day dust mixing-ratio corresponds to roughly a fourfold increase from the mean (See Supporting Information 2.S5), therefore, we expect that the variability of dust loading should dominate over temperature variations, given a temperature constraint of about 3 K or less.

As mentioned in Sect. 2.3, we excluded the seasonal component of the dust-cloud-phase correlation by calculating the deciles independently for each month of the year. However, shorter cycles (e.g., weather variability) may still influence the variability of dust and cloud phase. For example, below the -42°C isotherm more liquid clouds are found in convective sectors and more cirrus clouds at the detrainment regions. However, it is still possible to distinguish between dusty and non-dusty conditions at each point of the weather cycle. Consequently, once we average over the weather cycle — using monthly means inside each dust percentile — we expect the dust-cloud-phase relationship to be dominated by the microphysical effect of dust on cloud phase.

Despite the long period (2007-2010) used in the study, a significant fraction of the 5-dimensional space used for our analysis (10 dust deciles, 12 months, 15 temperature bins, 96 latitudes, and 12 longitudes) is sparsely sampled or even contains missing values. In the high-latitudes, a sampling bias exists towards the respective winter seasons because very few night-time retrievals are available in summer. However, the seasonal variability was not found to be a dominating factor in the day-to-day impact of dust mixing-ratio on the FPR (See Supporting Information 2.S19). Furthermore, many factors may contribute to higher standard

deviations for the ice occurrence, including:

- Changes in dynamical forcing (e.g., updrafts) and cloud regimes
- Temperature changes after cloud glaciation (e.g., latent heat release)
- Ice sedimentation from above (cloud seeding), and INPs other than dust
- Cloud vertical distribution within the studied temperature ranges
- Turbulence favouring aerosol mixing and sub-grid temperature fluctuations
- Differences in dust mineral composition, electric charge or size
- Coatings (e.g. Sulfate) affecting aerosol solubility and freezing efficiency
- Subsetting of the data (e.g., only night-time retrievals)

Additionally, some issues arise from the coarse spatial resolution used in our study. A high dust mixing-ratio simulated in a volume gridbox indicated as cloudy by the satellite observations does not ensure that the dust is actually mixed with the cloud. The subgrid-distribution of dust relative to the exact cloud position remains unresolved. Higher dust mixing-ratios should be interpreted as an indicator or a higher probability that a significant amount of dust was mixed with a collocated cloud. This mixing may have happened during or before the observation by the satellite. However, we can assume that both cloud and dust aerosol followed a similar trajectory up to the moment of the observation. Overall, at coarse resolutions, the combination of modelled dust concentrations with satellite-retrieved cloud properties cannot guarantee the mixture of aerosol and clouds (R. Li et al., 2017). Similarly, the atmospheric parameters obtained from the reanalysis may not match the conditions for the exact position of the clouds in the satellite retrievals. However, the atmospheric parameters are expected to match on average the large-scale conditions influencing the aerosol-cloud interactions.

As mentioned in Sect. 2.3, the total AOD from MODIS is assimilated in the MACC reanalysis. In general, we expect this assimilation to produce a fair estimation of the large-scale aerosol conditions on a day-to-day basis. At least for the Northern Hemisphere, this has been already validated with in situ measurements (Cuevas et al., 2015). Both the ERA-Interim and the MACC reanalysis are based on the IFS system. Thus, both the aerosol and meteorological estimations are consistent.

The CALIPSO-GOCCP product relies on CALIOP to determine the presence of clouds. Nevertheless, the reader should be aware that several uncertainties remain. For example, the meteorology in the reanalysis and in the real atmosphere may differ, particularly on the sub-grid scale. In the worst-case that the reanalyses are entirely inconsistent with the retrievals of cloud phase, we expect the result would be the lack of correlation between dust and the ice occurrence (Fig. 2.8-2.10). We have included a reasonably large dataset for the study. Certainly, mismatches between reanalysis and cloud retrievals are possible. However, these would cause

an underestimation — and not an overestimation — of the dust-cloud-phase correlation.

Concerning the interpretation of our results, it cannot be ruled out that the increase in ice cloud occurrence in the Southern Hemisphere for higher dust loading arises from other types of INP such as biogenic aerosol (Burrows et al., 2013; O’Sullivan et al., 2018; Petters & Wright, 2015) or background free-tropospheric aerosol (Lacher et al., 2018), which could be misclassified as mineral dust in the reanalysis. Similarly, a possible correlation between ice cloud occurrence and the atmospheric conditions leading to the emission and transport of mineral dust should be further investigated (e.g., dusty air masses from land are usually warmer and drier). Another interesting explanation of the results presented in this study could involve the mixing of mineral dust particles with ice nucleation active macromolecules (Augustin-Bauditz et al., 2016). Such particles are in the size of few 10 nm (Fröhlich-Nowoisky et al., 2015) and would therefore not be detected if mixed with dust aerosol. Furthermore, biases such as the overestimation of the fine-mode dust aerosol in the MACC reanalysis (Ansmann et al., 2017; Kok, 2011) may shift the mixing-ratios shown in Sect. 2.4.4. However, as long as such biases are not limited to certain meteorological conditions, the cloud phase averaged inside each dust decile should remain unaffected.

In general, meteorological parameters have a larger impact on cloud properties than aerosols do (Gryspeerd et al., 2016). For example, different updraft regimes can change the aerosol-cloud interactions in warm clouds by an order of magnitude. Therefore, it is essential to study how such meteorological parameters relate to the dust aerosol loading. Firstly, the correlation between fine-mode dust mixing-ratio and the RH from the ERA-Interim reanalysis — weighted by cloud volume fraction — was found to be negative (see Fig. 2.11a). We note that the RH from ERA-Interim represents the conditions at a large-scale and not the conditions at a specific location and the moment of the interaction between dust aerosol and supercooled cloud droplets. Still, this relationship is consistent with the intuition that dust is mostly associated with drier air masses.

Second, The significant positive correlation found between dust aerosol mixing-ratio and the height of the isotherms (weighted by cloud volume fraction) points to a possible source of uncertainty (Fig. 2.11b). This correlation could be due to clouds being detected in a higher temperature bin after being glaciated at lower temperatures. Thus erroneously suggesting an enhanced glaciation occurrence frequency at higher temperatures. Therefore, future studies must take into account this possibility when studying the occurrence of ice clouds at a certain isotherm. More details on the spatiotemporal variability of the cloud height can be found in the Supporting Information (2.S12). Lastly, Fig. 2.11c shows a positive correlation between the fine-mode dust and the large-scale vertical velocity from the MACC reanalysis at -15°C . Updrafts favour saturation over liquid water and therefore CCN activation, droplet growth and inhibition of the Wegener–Bergeron–Findeisen process. Therefore, a positive dust-updraft correlation could lead to an underestimation of the dust-cloud-phase relationship.

T°C	Range	FPR North-South	Fine dust mixing-ratio	Hypothesis	Related studies
-15°C	-21 to -9°C (252 to 264 K)	-5 to -3% (high LTSS)	0.1-1 µg/kg	Higher feldspar fraction (or efficiency) from the sources in the Southern Hemisphere.	Boose et al. (2016) Atkinson et al. (2013)
-22°C	-27 to -18°C (246 to 255 K)	±2%	0.03-0.3 µg/kg	A transition regime between the immersion freezing of clay minerals and feldspar, or dominance of contact freezing of clay minerals.	Hoose et al. (2008)
-30°C	-36 to -24°C (237 to 249 K)	+3 to +5%	0.03-0.3 µg/kg	Immersion freezing efficiency of Illite/Montmorillonite (Northern Hemisphere) higher than of Kaolinite (Southern Hemisphere).	Hoose et al. (2008) Claquin et al. (2008) Broadley et al. (2012) Murray et al. (2011)

Table 2.1: Summary of the north-south differences in the cloud phase associated with mineral dust based on the day-to-day statistics for the mid- and high latitudes.

In summary, much of the co-variability between dust, humidity, updrafts, temperature and cloud ice occurrence-frequency is still poorly understood. However, we expect that the constraints on humidity and static stability minimized most of the biases discussed in this section.

2.6 Conclusions

For the first time, an aerosol reanalysis was combined with satellite retrievals of cloud thermodynamic phase to investigate the potential effect of mineral dust as INP on cloud glaciation. We studied this effect on a day-to-day basis at a global scale for the period 2007-2010 focusing on stratiform clouds observed at night-time in the mid- and high latitudes. Our main findings can be summarized as follows:

1. Between -36°C and -9°C , day-to-day increases in fine-mode dust mixing-ratio (from lowest to highest decile) were mostly associated with increases in the day-to-day cloud ice occurrence-frequency (FPR) of about 5% to 10% in the mid- and high- latitudes.
2. The response of cloud ice occurrence-frequency to variations in the fine-mode dust mixing-ratio was similar between the mid- and high- latitudes and between Southern and Northern Hemispheres. Even though dust aerosol is believed to play a minor role in cloud glaciation in the Antarctic region, increases in FPR from first to last dust decile were also present in both the northern and southern high-latitudes
3. Using constraints on atmospheric humidity and static stability we could partly remove the confounding effects due to meteorological changes associated with dust aerosol.

4. The results also suggest the existence of different sensitivities to mineral dust for different latitude bands. The north-south differences in ice occurrence-frequency for similar mineral dust mixing-ratios agree with previous studies on the mineralogical differences between Southern and Northern Hemisphere. A larger fraction of feldspar in the Southern Hemisphere could explain the differences at -15°C , and the higher freezing efficiency of Illite and Smectite (more abundant in the Northern Hemisphere) over Kaolinite (more abundant in the Southern Hemisphere) could explain the differences at -30°C .

We believe these new findings may have an important influence on improving the understanding of heterogeneous freezing and the indirect radiative impact of aerosol-cloud interactions. The authors hope that the results of this work will also motivate further research, including field campaigns in remote regions to study the day-to-day variability of cloud thermodynamic phase and the role of mineral dust in ice formation, satellite-based studies of associated changes in the radiative fluxes, and modelling studies to test the representation and relevance of specific processes involved in ice formation and mineral dust transport. Such studies could help to further improve our understanding of the influence of mineral dust or other aerosol types on cloud glaciation and the climate system.

2.7 Appendix: Related cloud products

Although in our study we used the cloud phase classification from the CALIPSO-GOCCP product, other products are also available. Therefore, we include in the following appendix a detailed comparison between the CALIPSO-GOCCP and the DARDAR-MASK product, which is commonly used in the literature as well.

2.7.1 2B-CLDCLASS

The CloudSat cloud scenario classification (2B-CLDCLASS) was used in Sect. 2.4.1 to identify different cloud types present in the case study. The classification uses the radar reflectivity observed by the Cloud Profiling Radar (CPR) on-board the CloudSat satellite together with the attenuated backscatter signal from CALIOP to classify clouds into 8 different types. These are: low-level (stratocumulus and stratus), mid-level (altostratus and altocumulus) and high-level clouds (cirrus), and clouds with vertical development (deep convection clouds, cumulus, and nimbostratus). The main criteria for the classification of non-precipitating clouds are the radar reflectivity and temperature obtained from the ECMWF-AUX product. The CPR is highly sensitive to large particles (e.g., raindrops) and therefore clouds with a reflectivity larger than a given temperature-dependent threshold can be considered as precipitating (e.g., nimbostratus). This reflectivity threshold is a function of temperature and ranges from -10 to 0 dBZ. The fifth range gate of the CPR (around 1.2 km above ground level) is used for this classification. The standard error of the ECMWF-AUX temperature, which is based on the IFS system of the ECMWF, has been estimated to be around 0.6 K in the troposphere.

2.7.2 DARDAR-MASK

The DARDAR-MASK v1.1.4 product available at the ICARE data center combines the attenuated backscatter from CALIOP (at 532 nm; sensible to small droplets), the reflectivity from the CPR (at 94 GHz; sensible to larger particles) and the temperature from the ECMWF-AUX product to assess cloud thermodynamic phase. The radar voxels have a horizontal resolution of 1.4 km (cross-track) \times 3.5 km (along-track) and a vertical resolution of 500 m, with a nadir angle of 0.16° of the radar beam. A decision about the cloud phase is made for each voxel with a 60 m vertical resolution to take advantage of the lidar resolution. These voxels are collocated with the CloudSat footprints (1.1 km horizontal resolution). If the backscatter lidar signal is high ($>2.10 \times 10^{-5} \text{ m}^{-1} \text{ sr}^{-1}$), strongly attenuated (down to at least 10% in the next 480 m) and penetrates less than 300 m into the cloud, it is assumed that supercooled droplets are present. In this case, the voxel is categorized as supercooled or mixed-phase depending on the radar. A high radar reflectivity is assumed a priori to indicate the presence of ice particles. Otherwise, the voxel is categorized as ice. In some sporadic cases, voxels can also be classified as mixed-phase. For simplicity, we coerce this mixed-phase category into the liquid category. Therefore, when we talk about a mixed-phase cloud we refer exclusively to an atmospheric column with ice voxels immediately below liquid voxels.

2.7.3 $\text{FPR}_{\text{DARDAR,ALT}}$

To assess the differences between the cloud phase from the DARDAR-MASK and CALIPSO-GOCCP products, we defined a new phase ratio based on the DARDAR-MASK classification. In this alternative definition, which we call ALT-DARDAR, only gridboxes ($1.875^\circ \times 30^\circ \times 3 \text{ K}$) fully filled with ice voxels are considered as ice (fully glaciated). Therefore, just a single liquid voxel is enough to define a gridbox as liquid (not fully glaciated). This definition ignores the cloud ice in mixed-phase clouds, which is mostly only detected as such by the DARDAR-MASK product and neglected by the CALIPSO-GOCCP product. However, this neglect of ice in mixed-phase clouds helps to clarify the differences between the products by finding common ground to compare the DARDAR-MASK and CALIPSO-GOCCP products. For $\text{FPR}_{\text{GOCCP}}$ and $\text{FPR}_{\text{DARDAR}}$, the FPR is calculated as the ratio of ice voxels to the total number of voxels within each gridbox. The $\text{FPR}_{\text{ALT,DARDAR}}$ uses gridboxes instead.

2.7.4 Case study comparison

Some major differences can be observed between the three FPR^* variables in Fig. 2.12.d–f. For the altocumulus cloud at 35–40°S and $+3^\circ\text{C}$ to -6°C , the ice virgae falling from the cloud ($\text{FPR}_{\text{DARDAR}}$) are missed in the $\text{FPR}_{\text{GOCCP}}$. Such mixed-phase clouds are reclassified in $\text{FPR}_{\text{ALT,DARDAR}}$ as liquid clouds. A similar case is observed for the stratocumulus clouds at 50–55°S and $+3^\circ\text{C}$ to -6°C , and for the altostratus at 35–45°S below the -20°C isotherm (at higher temperatures). Finally, the cirrus clouds above -33°C remain nearly unaffected by the reclassification in $\text{FPR}_{\text{ALT,DARDAR}}$ as it is classified as fully glaciated. Clouds between 38°S and 44°S, ranging from 6°C to -33°C in temperature, are classified mostly as altostratus by the 2B-CLDCLASS product. These altostratus clouds offer a good opportunity to compare the

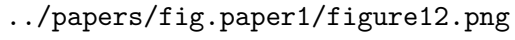
three FPR variables in detail. **FPR_{GOCCP}**: The detected ice virgae below the liquid cloud top suggest that the cloud top did not fully attenuate the lidar signal (not optically thick enough). The number or size of the ice particles near the cloud top probably was not enough to increase the depolarization ratio above the threshold value for the GOCCP algorithm and was therefore classified as liquid. **FPR_{DARDAR}**: In the decision tree of the DARDAR algorithm, there are multiple alternatives for a mixture of cloud droplets and ice particles (e.g., at cloud top) to be classified as ice only:

- a) If the lidar backscatter signal is lower than $2.10 \text{ 5 m}^{-1} \text{ sr}^{-1}$
- b) If not a): If it is weakly attenuated (less than 10 times) or not rapidly attenuated (at a depth larger than 480 m).
- c) If not b): If the layer thickness of the cloud is larger than 300 m. This is equivalent to 5 voxels with a lidar vertical resolution of 60 m.

Therefore, there are many cases where a mixed-phase cloud can be miss-classified as ice only in the DARDAR product and consequently in the $\text{FPR}_{\text{DARDAR}}$ variable. This misclassification may happen, for example, in optically thin stratiform cloud containing liquid. In this specific case, we speculate that c) is the most probable cause because of the large vertical extent of the clouds around 1 to 5 km using a moist adiabatic lapse rate of -6 K km^{-1} for the estimation). **FPR_{ALT,DARDAR}**: In the case of droplets and ice particles coexisting at cloud top, we expect that at some location the cloud droplets will be enough in number for one of the voxels to be classified as liquid (strong attenuation) in the DARDAR-MASK algorithm. If this is the case, the entire volume gridbox value of $\text{FPR}_{\text{ALT,DARDAR}}$ will be LIQUID. We interpret this as a non-completely glaciated cloud. In summary, the GOCCP algorithm is unable to detect ice in mixed-phase clouds, and the DARDAR algorithm tends to classify mixed-phase clouds as ice. Therefore, we avoid using the frequency of cloud ice (FPR) to compare the GOCCP and DARDAR products. Instead, we use the $\text{FPR}_{\text{ALT,DARDAR}}$ as common ground. In $\text{FPR}_{\text{ALT,DARDAR}}$, a significant portion of mixed-phase clouds that would otherwise be classified as ICE is now classified as LIQUID. This replicates the inability of the GOCCP algorithm to detect ice in mixed-phase clouds. In other words, the frequency of completely glaciated clouds, which is represented by $\text{FPR}_{\text{ALT,DARDAR}}$ and $\text{FPR}_{\text{GOCCP}}$, allows a comparison of both algorithms, mostly by ignoring ice virgae in $\text{FPR}_{\text{ALT,DARDAR}}$ when cloud droplets are also present in the same gridbox. This idea is summarized in Table 2.2. It is important to note that the behaviour of $\text{FPR}_{\text{ALT,DARDAR}}$ is highly sensitive to the gridbox volume, i.e. to the horizontal and vertical resolution. Calculated in finer resolutions, the $\text{FPR}_{\text{ALT,DARDAR}}$ will be closer to $\text{FPR}_{\text{DARDAR}}$. With coarser resolutions, the $\text{FPR}_{\text{ALT,DARDAR}}$ will be biased towards the liquid phase because the probability of including an ice voxel in the volume gridboxes will increase. A gridbox volume of $1.875^\circ \times 1.875^\circ \times 3 \text{ K}$ is coarse enough to study stratiform clouds from mid-latitude frontal systems.

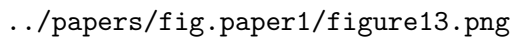
2.7.5 Temperature comparison

For temperatures between -40°C and 1.5°C the $\text{FPR}_{\text{DARDAR}}$ only decreases down to 60% at 1.5°C (see Fig. 2.13). This difference is partly due to the higher sensitivity of the radar to



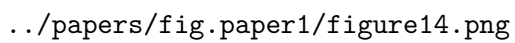
`../papers/fig.paper1/figure12.png`

Figure 2.12: Same as Fig. 2.4d but including DARDAR and ALT-DARDAR products.



`../papers/fig.paper1/figure13.png`

Figure 2.13: Same as Fig. 2.5 but including DARDAR and ALT-DARDAR products.



`../papers/fig.paper1/figure14.png`

Figure 2.14: Same as Fig. 2.6 but including ALTDARDAR products.

ice particles, especially falling ice. Additionally, in the DARDAR algorithm, water can be still classified as ice at $+1.5^{\circ}\text{C}$ due to the melting layer being set to a wet-bulb temperature of 0°C . This threshold allows the detection of ice at temperatures slightly above 0°C dry-bulb temperatures (named simply temperature in this work). For instance, at a relative humidity of 50%, a temperature of about $+2.5^{\circ}\text{C}$ would correspond to a wet-bulb temperature of -2.5°C . Nevertheless, this last effect is not relevant for temperatures below freezing.

In contrast, $\text{FPR}_{\text{ALT,DARDAR}}$ follows very closely the pattern of the $\text{FPR}_{\text{GOCCP}}$ down to -1.5°C . The absolute differences of the global averaged $\text{FPR}_{\text{ALT,DARDAR}}$ and $\text{FPR}_{\text{GOCCP}}$ are less than 10% between -42°C and 0°C . This shows that the temperature dependence of the alternative phase ratio $\text{FPR}_{\text{ALT,DARDAR}}$ and $\text{FPR}_{\text{GOCCP}}$ agree better than for $\text{FPR}_{\text{DARDAR}}$. In average, within a volume gridbox of $1.875^{\circ}\times 1.875^{\circ}\times 3$ K the presence of single liquid voxels in the DARDAR product often coincides with the classification of the entire volume gridbox as liquid in the GOCCP product.

2.7.6 Latitude comparison

As shown in Fig. 2.14.b, at -15°C , the local maxima for $\text{FPR}_{\text{ALT,DARDAR}}$ are similar to $\text{FPR}_{\text{GOCCP}}$ but occur at higher latitudes, at 61°S and 61°N with values 69% and 74%. In comparison, the differences between $\text{FPR}_{\text{GOCCP}}$ and $\text{FPR}_{\text{ALT,DARDAR}}$ at -15°C are much lower than at -30°C . Moreover, the $\text{FPR}_{\text{GOCCP}}$ at -15°C is lower than the $\text{FPR}_{\text{ALT,DARDAR}}$ at the southern mid-latitudes and northern high-latitudes. In conclusion, the DARDAR and CALIPSO-GOCCP products still differ in some important aspects. However, to simplify the reproducibility of our study, we only present the results for CALIPSO-GOCCP, which is already available at a $2^{\circ}\times 2^{\circ}$ horizontal grid and 3 K vertical levels.

Variable	Ice virgae classified as	Ice and liquid in same gridbox (1.875°)	Ice fraction between 0 and -42°C	Explanation	References
$\text{FPR}_{\text{GOCCP}}$	not detected	ice or liquid (depolarization)	0 – 100%	Bias towards liquid cloud tops	Cesana and Chepfer (2013)
$\text{FPR}_{\text{DARDAR}}$	Ice	ice or liquid (radar reflectivity)	60 – 100%	Ice virgae dominate the cloud phase	Delanoë and Hogan (2008,2010)
$\text{FPR}_{\text{ALT,DARDAR}}$	Liquid or Ice (see next column)	liquid	10 – 90%	Ice virgae are mostly ignored in the gridbox if cloud droplets are also present	-

Table 2.2: Summary of the different variables used to assess the Frequency Phase Ratio (FPR).

2.S Supporting Information for ”The day-to-day co-variability between mineral dust and cloud glaciation: A proxy for heterogeneous freezing”

Contents of the supporting information:

2.S1–2.S3: Frequency phase ratio (FPR) variables.

2.S4–2.S7: Dust aerosol data from MACC reanalysis.

2.S8–2.S9: Cloud volume fraction of all clouds and only stratiform clouds (CALIPSO-GOCCP).

2.S10–2.S13: Vertical velocity (MACC), relative humidity (ERA-Interim), isotherm height and temperature (ECMWF-AUX).

2.S14–2.S16: Sample size distribution (FPR_{GOCCP}).

2.S17–2.S20: Day-to-day covariability between ice and dust without meteorological constraints.

All figures are derived using data for 2007–2010. For figures 2.S.1–2.S.14, the subfigures are organized as:

- a) Time average at -15°C (averaged in a 12 K range).
- b) Time-zonal average.
- c) Zonal average at -15°C (averaged in a 12 K range).

For the contour plots, the colour and pattern of the overlaid boxes are a reference for the regression lines in 2.S18 and 2.S19.

../papers/fig.paper1.si/Slide01.png

Figure 2.S1: Frequency Phase Ratio FPR_{DARDAR} .

../papers/fig.paper1.si/Slide02.png

Figure 2.S2: Frequency Phase Ratio $FPR_{ALT_{DARDAR}}$.

../papers/fig.paper1.si/Slide03.png

Figure 2.S3: Frequency Phase Ratio FPR_{GOCCP} .

../papers/fig.paper1.si/Slide04.png

Figure 2.S4: Coarse (0.9–20 μm) dust mixing ratio from MACC [kg kg^{-1}].

../papers/fig.paper1.si/Slide05.png

Figure 2.S5: Standard deviation of coarse (0.9–20 μm) dust mixing ratio from MACC [$\log(\text{kg kg}^{-1})$].

../papers/fig.paper1.si/Slide06.png

Figure 2.S6: Fine (0.03–0.55 μm) dust mixing ratio from MACC [kg kg^{-1}].

../papers/fig.paper1.si/Slide07.png

Figure 2.S7: Standard deviation of fine (0.03–0.55 μm) dust mixing ratio from MACC [$\log(\text{kg kg}^{-1})$].

../papers/fig.paper1.si/Slide08.png

Figure 2.S8: Cloud volume fraction from MACC.

../papers/fig.paper1.si/Slide09.png

Figure 2.S9: Stratiform cloud volume fraction [%] from MACC.

../papers/fig.paper1.si/Slide10.png

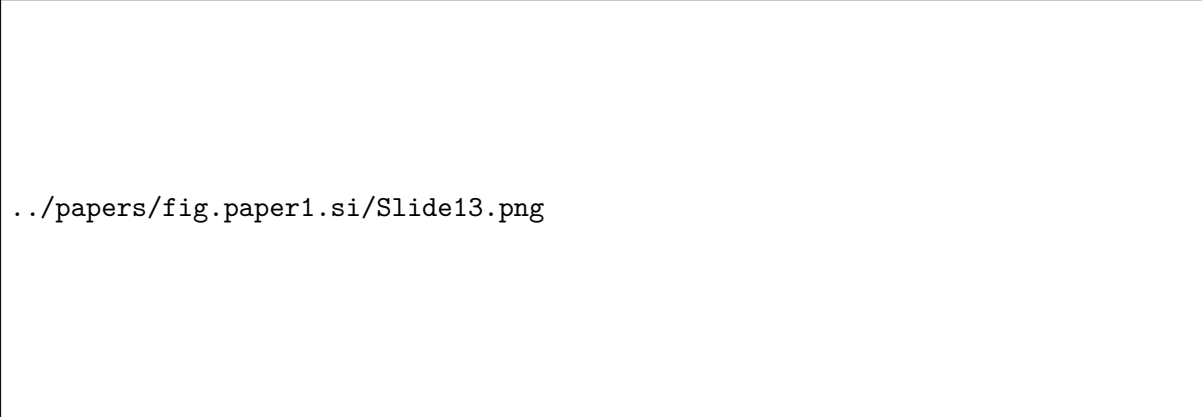
Figure 2.S10: Vertical velocity [Pa s^{-1}] for stratiform clouds from MACC.

../papers/fig.paper1.si/Slide11.png

Figure 2.S11: Relative humidity [%] for stratiform clouds from MACC.

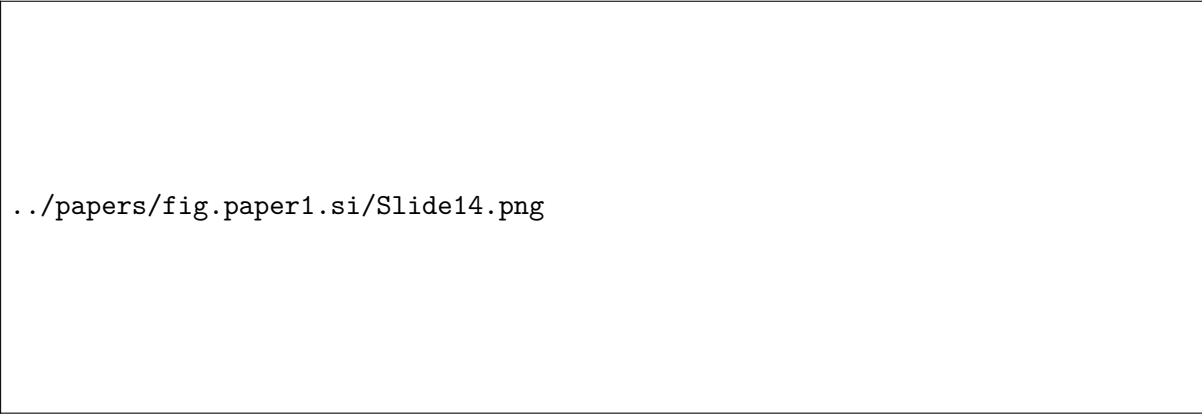
../papers/fig.paper1.si/Slide12.png

Figure 2.S12: Isotherm height [m] from ECMWF-AUX.



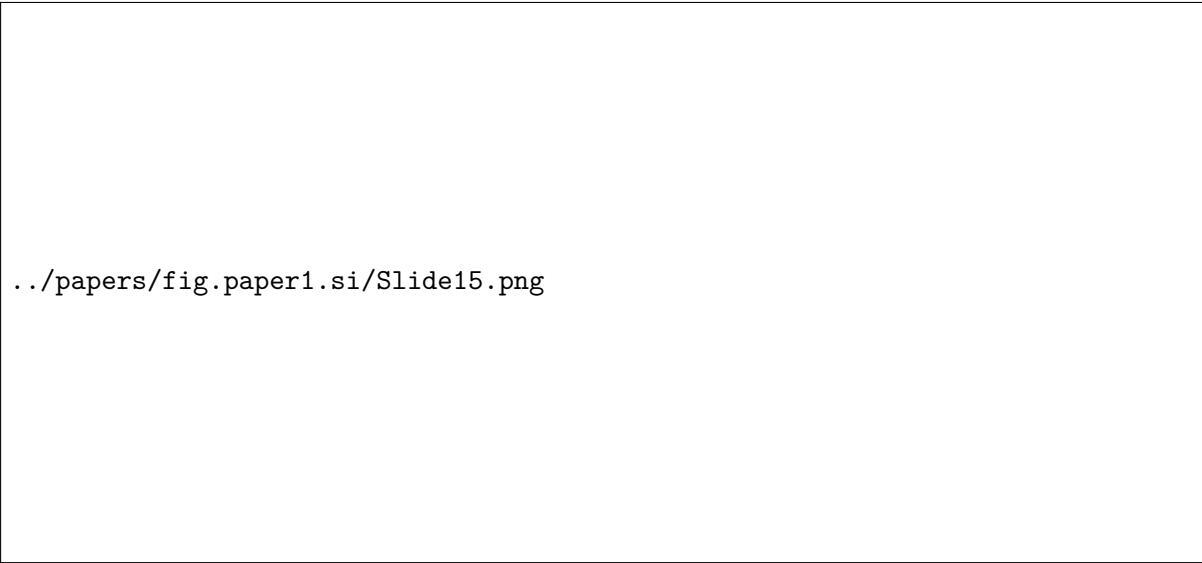
../papers/fig.paper1.si/Slide13.png

Figure 2.S13: Temperature [K] from ECMWF-AUX.




../papers/fig.paper1.si/Slide14.png

Figure 2.S14: Sample size for stratiform clouds [#gridboxes(month, dust decile, temperature, latitude, longitude)].



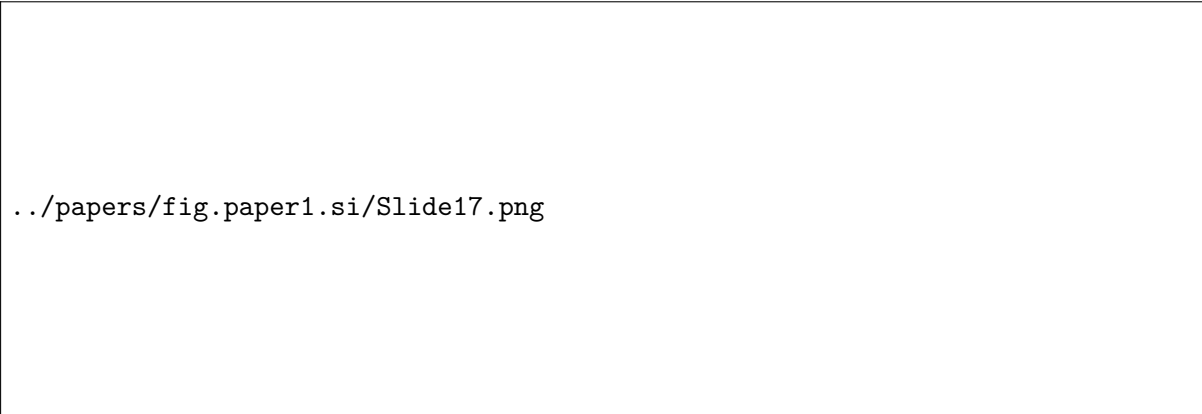
../papers/fig.paper1.si/Slide15.png

Figure 2.S15: Sample size of stratiform clouds [#gridboxes] for different seasons.



../papers/fig.paper1.si/Slide16.png

Figure 2.S16: Sample size [#gridboxes] for a) highest fine dust decile and b) lowest fine dust decile. c) difference between highest and lowest decile.



../papers/fig.paper1.si/Slide17.png


Figure 2.S17: Day-to-day normalized covariance $\frac{COV(FPR,dust)}{STD(dust)}$ [%] between fine dust from MACC and FPR_{GOCCP}.

../papers/fig.paper1.si/Slide18.png

Figure 2.S18: FPR_{GOCCP} [%] vs a) fine and b) coarse dust at -15 °C.

../papers/fig.paper1.si/Slide19.png

Figure 2.S19: FPR_{GOCCP} [%] vs fine dust at a) -30 °C and b) for winter and sommer season at -15 °C.



../papers/fig.paper1.si/Slide20.png

Figure 2.S20: FPR_{GOCCP} [%] over sea and land a) against fine dust from MACC at $-15\text{ }^{\circ}\text{C}$ and b) against temperature. The vertical lines correspond to the standard deviation between a) longitudes and b) months of the year.

Chapter 3

The hemispheric and seasonal contrast in cloud thermodynamic phase from A-Train spaceborne instruments*

The hemispheric contrast in cloud phase is crucial for quantifying the effect of ice-nucleating particles. However, there is still high spread between different retrieval methods, leading to high uncertainty in the magnitude of the hemispheric contrast in cloud phase. To gain a better insight, we combine a spaceborne lidar, radar, radiometer, and polarimeter to derive a high-confidence retrieval of cloud-phase. We used the new product ensemble to quantify the hemispheric and, for the first time, the seasonal contrast in cloud phase. The results show a higher cloud phase in the boreal spring, which coincides with higher dust concentrations. Moreover, the product ensemble showed a much higher seasonal and hemispheric contrast of cloud phase compared to the individual products. In summary, the product ensemble offers a new cloud phase reference, which is less affected by individual instrumental biases.

*Published as: Villanueva, D., Senf, F., and Tegen, I. (2021). Hemispheric and seasonal contrast in cloud thermodynamic phase from A-Train spaceborne instruments. *Journal of Geophysical Research: Atmospheres*, 126, e2020JD034322. doi: 10.1029/2020JD034322.

3.1 Introduction

Where do clouds glaciate? Ice clouds are more frequent in the northern hemisphere than in the southern hemisphere (Kanitz et al., 2011; A. E. Morrison et al., 2011; Tan et al., 2014). Understanding this contrast is of great importance for climate predictions, as liquid clouds reflect more shortwave radiation compared to ice clouds (Trenberth & Fasullo, 2010; Bodas-Salcedo et al., 2014; Matus & L’Ecuyer, 2017; Vergara-Temprado et al., 2018). Specifically, in the southern hemisphere, climate models show that the frequency of liquid clouds is associated with changes in sea surface temperature and the atmospheric cross-equatorial energy transport (Hawcroft et al., 2017). Moreover, there is high variability in the cloud-phase partitioning between climate models, which has been associated with uncertainties in cloud fraction and climate sensitivity (Zelinka et al., 2020; Tan et al., 2016; McCoy et al., 2016).

Previous studies have tried to elucidate the hemispheric and seasonal differences in cloud-phase by using spaceborne retrievals of aerosol loading and cloud-phase from lidar and radar retrievals. Several studies have attributed the north-south contrast in cloud-phase to the hemispheric differences in the concentration of ice-nucleating particles (INP) such as dust aerosol (Choi et al., 2010; Tan et al., 2014; Vergara-Temprado et al., 2017; Zhang et al., 2018). Due to land-ocean distribution, the largest dust sources (such as the Saharan Desert) are located in the northern hemisphere. Additionally, during spring in the northern hemisphere, dust concentrations are generally higher than in fall (Cowie et al., 2014; Luo et al., 2015). In the same season, it has been shown that clouds tend to produce more ice (Zhang et al., 2018). However, this seasonal contrast has received less attention so far.

In general, the spatio-temporal correlation between mineral dust and ice cloud frequency suggests that dust INP may be controlling the north-south contrast in cloud-phase (Seifert et al., 2010; Zhang et al., 2012; Tan et al., 2014; Villanueva et al., 2020). However, dust concentrations are also correlated with other meteorological factors like humidity, thermal stability and vertical velocity, which are in turn correlated to the ice cloud frequency (Sullivan et al., 2016; J. Li et al., 2017). This has led to a debate over whether dust INP or meteorology dominates the observed variability of cloud glaciation. Therefore, assessing the hemispheric and seasonal cloud-phase contrast in detail may lead to a better understanding of dust-driven cloud glaciation.

Most satellite cloud-phase products available are based on passive radiometers (e.g., sorted as Satellite-Instrument-Product: NOAA-AVHRR-PATMOS, Terra-MODIS-C6, and METEOSAT-SEVIRI-CLAAS). Active instruments capable of retrieving cloud-phase, like lidar and radar, are more scarce. From 2007 until 2010, several instruments capable of retrieving cloud-phase were synchronized to follow the same orbit (“A-Train”). During this period, a radiometer, lidar, radar, and a multi-angle radiometer retrieved cloud properties almost without interruption. Each of these instruments has been used individually to assess cloud-phase globally based on different cloud physical features (Y. Hu et al., 2009; Riedi et al., 2010; Huang et al., 2012). Moreover, synergies between them have been proven to be even more successful than the individual products (Riedi et al., 2010; Delanoë & Hogan, 2010). As extension to Villanueva et al. (2020), where only the CALIOP-GOCCP product was used to assess the temporal (daily) variability of cloud-phase, this study combines the different products available from the A-Train

to locate and quantify the seasonal- and hemispheric contrast of cloud top phase. Such a combined quantification has been lacking up to now. These contrasts in cloud-top-phase can then be compared to the variability of dust aerosol to assess the potential role of dust INP. Furthermore, we expect that this new information may serve as a benchmark for improving dust-driven cloud glaciation in climate simulations.

3.2 Data and Methods

3.2.1 A-Train cloud phase products

Fig. 3.1 shows the spaceborne instruments and products from the A-Train used in this study for the period 2007-2010 and the respective flow diagram of how we generate the GDP ensembles (GOCCP-DARDAR-PML2). The Cloud-Aerosol LIdar with Orthogonal Polarization (CALIOP) onboard CALIPSO (Y. Wu et al., 2014) and the Cloud Profiling Radar (CPR) on board CloudSat are both active instruments. In the GCM-Oriented Cloud Calipso Product (CALIPSO-GOCCP v3.0; Cesana & Chepfer, 2013), the lidar depolarization measured by CALIOP is compared against an empirical threshold to retrieve the cloud-phase, where higher depolarization ratios are associated with ice crystals. In the liDAR-raDAR (DARDAR-MASK v2.0) product (Delanoë & Hogan, 2010; Ceccaldi et al., 2013), a decision tree is used to retrieve the cloud-phase, where the main criterion is the cloud detection by the radar reflectivity (Mioche et al., 2014). A higher radar reflectivity is associated with larger particles such as ice crystals. In both the DARDAR and the GOCCP product, the detection of the cloud top is based on the CALIOP attenuated backscattering ratio. The cloud top temperature is then derived from the ECMWF-AUX reanalysis for the DARDAR product and from the GEOS-GMAO reanalysis for the GOCCP product. To avoid artifacts in the lidar due to daylight scattering, only night-time values are included for the GOCCP product. On the other hand, both daytime and nighttime retrievals are included for the DARDAR product.

The MODIS (MODerate resolution Imaging Spectroradiometer) onboard the Aqua satellite and the POLDER-3 (Polarization and Directionality of the Earth Reflectance) onboard the PARASOL satellite are both passive instruments. Different algorithms can be used with different radiometers to retrieve cloud top phase (Pavolonis et al., 2005; Riedi et al., 2010, for the AVHRR and MODIS instrument, respectively). The MODIS ShortWave-InfraRed (SWIR) product uses the ratio between the measured reflectance in the near-infrared and in the visible spectra to retrieve the cloud-phase, where low ratios are associated with ice crystals. The MODIS Thermal-InfraRed (TIR) product uses the Brightness Temperature Difference (BTD) between the 8.5- and 11- μm bands. This difference, also known as BTD[8.5–11], is used to retrieve the cloud-phase, where high positive values are associated with ice crystals. The POLDER-3 instrument can retrieve the polarized and total radiance. Therefore, it can estimate the polarization ratio for different scattering angles. Thus, in the POLAR algorithm, a decreasing polarization with increasing scattering angle is associated with ice crystals. Additionally, a peak in the polarization near 140° (rainbow effect) implies the presence of cloud droplets (Riedi et al., 2010).

The PARASOL and Aqua/MODIS combination (PM-L2) product weights the MODIS-



Figure 3.1: Diagram showing the different cloud-phase products used to derive the GDP ensemble (GOCCP-DARDAR-PML2). The colored boxes correspond to the spaceborne instruments used for each product (colored acronyms) and the colored values represent the wavelength used for the classification. In case of multi-band instruments, the wavelength range is shown. Values in italics denote multi-angle observations of total and polarized radiance. The lower part of the diagrams shows how the products are rebinned and processed to create the GDP2 and GDP3 ensembles.

SWIR, MODIS-TIR and POLDER-3-POLAR products to make a final decision about the cloud-phase at cloud top. For each decision, a confidence level is calculated depending on which products agree on the same cloud-phase. A confidence flag of 0 means that all three products (SWIR, TIR and POLAR) agree with high confidence on the ice-phase and a flag of 200 means that all agree on the liquid-phase. To distinguish between the liquid- and ice-phase, we use only confidences below 25 or above 175. We chose this threshold to optimize the agreement with the active products, focusing on the range of the observed frequency of ice cloud tops. With the 25/175 confidence threshold, the cloud ice frequency ranges from 0.05 to 0.95. Using a 10/190 confidence threshold resulted in an ice frequency range from 0.02 to 0.99 but only 60% of the sample size relative to the 25/175 threshold. In contrast, a 50/150 confidence threshold resulted in a ice frequency range from 0.12 to 0.86 with 150% the sample size relative to the 25/175 threshold. Additionally, Coopman et al. (2020) showed that high confidence thresholds (20/180) result in a higher spatial correlation between cloud droplet size and cloud-phase. Finally, because the PM-L2 product relies on passive instruments, only daytime retrievals are included.

It is very challenging to determine why the cloud products may retrieve a different cloud top phase in a given cloud scenario. However, some known issues have been already been discussed in detail in the literature (Huang et al., 2012, 2015; Riedi et al., 2010).

The most important factors that lead to different decisions are the size of cloud droplets and ice particles, the Cloud Optical Thickness (COT), and underlying clouds or surface. Fig. 3.2 shows some known microphysical settings that may lead to a wrong cloud-top-phase retrieval by some of the cloud products. When the number or size of ice particles at cloud top is high enough, the DARDAR algorithm will classify the top as ice regardless of the number of cloud droplets present (see Fig. 3.2a). Similarly, drizzle droplets can be large enough to be mistakenly classified as ice (Zhang et al., 2018), especially at temperatures above -10°C (see Fig. 3.2b). The POLAR algorithm applied to POLDER-3 is strongly sensitive to the cloud optical thickness (Riedi et al., 2010). For cirrus clouds overlying a liquid cloud, simulations showed that the POLAR algorithm will only retrieve the ice phase if the cloud optical thickness is higher than 2 (see Fig. 3.2c). On the other hand, in the TIR and SWIR algorithm applied to MODIS and included in PM-L2, the retrieved emissivity and reflectance may be dominated by the clouds or surface under the cloud, especially for thin clouds (see Fig. 3.2d). In the GOCCP product, if many small cloud droplets are present, multi-scattering effects may result in a high depolarization ratio, even when no ice is present (Y. Hu et al., 2009, see Fig. 3.2e). The spatial-angular (3D) characteristics of clouds may also influence the retrieved reflectance and radiance from the MODIS and POLDER instruments. For example, the polarization signal from POLDER becomes weak and ambiguous for broken clouds (Riedi et al., 2010).

We obtain the dust aerosol loading from the Copernicus Atmosphere Monitoring Service (CAMS) reanalysis (Inness et al., 2019). In the CAMS reanalysis, dust emission is a function of the wind near the surface (10 m), vegetation, soil moisture, and surface albedo. The simulated dust mixing ratio is corrected by assimilating the aerosol optical thickness at 550 nm retrieved by MODIS. Dust is removed in the model by dry and wet deposition.



Figure 3.2: Diagram showing the known retrieval biases associated to different cloud types for the different products. a) Ice virgae in mixed-phase clouds. b) Drizzle from liquid clouds. c) Cirrus over liquid clouds. d) Thin clouds and surface albedo. e) Multi-scattering effects. Retrievals in italics represent errors.

3.2.2 Collocation and GDP2 ensemble

Similar to the three-member combination of cloud-phase products in the PM-L2 product, we combine the GOCCP, DARDAR and PM-L2 products to create a daily cloud top phase ensemble.

Temporal merging: For each day, we merge both the ascending and descending overpasses temporally from 0 to 0 UTC (For GOCCP only night-time retrievals).

Vertical collocation: For the active products, only the top cloudy pixels from each instant vertical profile were included. Using the cloud top temperature available from each product, we assign each pixel to a 3 K temperature bin between -42°C and 3°C . We note that the cloud top temperature is derived differently for each product. The GOCCP and DARDAR products include an interpolation of atmospheric reanalyses, from which we use the temperature corresponding to the height of the top cloudy pixel. For the PM-L2 product, the cloud top temperature retrieved from MODIS is used instead. Other than for the active retrievals, the depth of the cloud top retrievals from MODIS and POLDER depends on the optical thickness of the cloud and may result in a bias in cloud-top-phase for thin clouds (Stengel et al., 2020). However, a sensitivity study showed that the difference in the ice cloud-top frequency between thin ($\text{COT}<2$) and thick ($\text{COT}>2$) clouds was low (less than $\pm 1\%$).

Horizontal collocation: We regrid all three products to a $2^{\circ}\times 30^{\circ}$ (lat \times lon) grid by averaging the binary cloud-phase flags contained inside each gridbox. Therefore, for the active products, each gridbox is sampled only through the narrow swath(s) crossing it. We refer to this average as the daily Frequency Phase Ratio (FPR_{daily}), the ratio of ice pixels to the total (liquid+ice) cloudy pixels included in each gridbox. The $2^{\circ}\times 30^{\circ}$ grid was chosen to optimize the overlap between the active instruments (narrow swaths) and passive instruments (wide swaths). For a visualization of the collocation method, please refer to the Supporting Information 3.S5–3.S7.

For each product, we use the frequency of ice pixels to classify each volume gridbox as either liquid or ice. After the collocation described above, for each product we obtain a 3-dimensional FPR_{daily} on a $3\text{ K}\times 2^{\circ}\times 30^{\circ}$ space (temperature \times lat \times lon). This FPR_{daily} represents the frequency of ice pixels within each gridbox at each temperature bin. Most of the regridded FPR_{daily} values for the different products lay below 0.1 or above 0.9; namely 75%, 71%, and 81% of the total sample size for the GOCCP, DARDAR, and PM-L2 products, respectively. Therefore, to simplify the combination of products, we rounded the FPR_{daily} of each individual product to the nearest integer (0 for liquid and 1 for ice). As a result, FPR_{daily} follows a binary distribution.

We combine the cloud-phase products by finding the cloud-phase for which most of the products agree. To produce the ensemble of cloud-phase products (see Fig. 3.1), we discard the time-steps where one or more products are missing. Because at least two products will always agree (on either liquid or ice), the cloud-phase is set to the mode between the three products. We refer to this three-member ensemble as the GDP2 ensemble (because at least 2 products agree).

The FPR_{daily} in the GDP2 ensemble corresponds to a daily phase classification dominated by the cloud-top-phase of stratiform clouds, which can be aggregated over time to derive a frequency of ice clouds. The product ensemble will contain missing data for the timesteps were

the cloud-phase products do not overlap. Therefore, the averaging order will play a role in the results. To avoid a bias towards the levels and gridboxes containing more data, we average in the following order: time, longitude, latitude, and temperature. After aggregating the FPR_{daily} within a certain time frequency (monthly in this work), it can be interpreted as the ice cloud-top frequency ($FPR_{monthly}$ or FPR for short). The FPR_{daily} is defined within a $2^\circ \times 30^\circ$ gridbox, so that the aggregated FPR will be dominated by the thermodynamic phase of horizontally broad clouds (i.e., stratiform clouds). The distinction between the binary frequency FPR_{daily} and the monthly-aggregated frequency FPR is important for the uncertainty analysis, because FPR_{daily} follows a binary distribution, while FPR follows a normal distribution for high sample sizes.

3.2.3 Sample size

After the regridding described above, FPR_{daily} follows a binomial distribution. In this distribution, the probability of finding an ice cloud top will be p (0 to 1), which depends mainly on temperature. Therefore, after aggregating (averaging) n measurements of cloud-phase (FPR_{daily}), the standard deviation of the instant ("observed") frequency FPR around the expected ("real") frequency p can be estimated as:

$$\sigma_{FPR} = \sqrt{\frac{p(1-p)}{n}} \quad (3.1)$$

In other words, the sample size will have an impact on the uncertainty in FPR . In addition, the spatio-temporal variability of cloud-phase (e.g., regional differences and seasonal cycle) and retrievals errors will also introduce an inter-monthly spread in the expected frequency p , contributing to the total spread σ_{FPR} .

For the period 2007-2010, a total of 1200 days had at least one retrieval for each cloud-phase product. In other words, for the average gridbox ($2^\circ \times 30^\circ$), the timelines of the individual instruments overlap for 82% of the period. During this period, for the ensemble and the individual products, the sample size is distributed relatively homogeneously between -42°C and $+3^\circ\text{C}$. However, between -10°C and -30°C the sample size decreases by about 25% for the GDP2 ensemble and the DARDAR product (see Supporting Information 3.S1). Fig. 3.3 shows the zonal vertical mean of the sample size, disagreement ratio, and frequency of ice cloud tops for the different phase products. Across latitudes, the sample size is similar in both hemispheres, especially between 75°N/S . The largest sample size is found near 55°N/S and at around 5°N (Fig. 3.3a). These peaks coincide with the average position of the storm tracks and the inter-tropical convergence zone, respectively. The sample size of GOCCP product tends to be higher than in the DARDAR product because GOCCP is not limited by the availability of retrievals from the CPR instrument. However, we only include nighttime retrievals for GOCCP, and therefore the sample size decreases relative to DARDAR above 60°N , especially in summer.

The sample size of the GOCCP and DARDAR products is limited by the narrow swath of CALIOP. In contrast, the broader swath of the POLDER-3 instrument results in a sample size nearly twice as large as for the active products. However, for the GDP2 ensemble, the sample size drops to about a half compared to GOCCP and DARDAR. The sample size of GDP2 depends

```
../papers/fig.paper2/lat.sample-eps-converted-to.pdf
```

```
../papers/fig.paper2/zon.error.quote-eps-converted-to.pdf
```

```
../papers/fig.paper2/lat.fpr-eps-converted-to.pdf
```

Figure 3.3: Zonal-vertical mean of (a) gridbox sample size in days (b) disagreement ratio for the individual cloud-phase products relative to the GDP2 ensemble (c) frequency of ice cloud tops for the different cloud-phase products. Averaged between 0°C and -42°C .

only on the spatio-temporal collocation between the individual gridded products. Therefore, to understand how each of these products affects the ensemble, we must first consider the two-member ensembles (DP: DARDAR and PM-L2; GP: GOCCP and PM-L2; GD: GOCCP and DARDAR). These ensembles are defined only when both members agree on the cloud-phase at cloud top. We define the collocation ratio as the sample size of the two-member ensemble divided by the maximal achievable sample size (assuming a perfect collocation). The collocation ratios are 69, 66, and 33% for the DP, GP, and GD ensembles, respectively. These collocation ratios show that the sample size of GDP2 is strongly limited by the poor collocation between the GOCCP and DARDAR products. We attribute this poor collocation to a cloud top temperature underestimation (of -5 K in average) in the DARDAR product (derived from the ECMWF-AUX reanalysis) relative to the GOCCP product (GEOS-GMAO reanalysis) and to the MODIS retrievals. Additionally, due to the temporal collocation between the products, the GDP ensembles only include scenarios where clouds are detected in the same gridbox during nighttime (by DARDAR and/or GOCCP) and daytime (by DARDAR and/or PM-L2), which further reduces the collocation ratio for the GDP ensembles.

3.3 Results

3.3.1 Agreement

To assess the single products with respect to the GDP2 ensemble, we define the disagreement ratio as the frequency of timesteps where the cloud-phase from a given product is different to that from the ensemble. On average, the GDP2 ensemble disagrees with the GOCCP, DARDAR and PM-L2 products 12%, 18% and 10% of the time, respectively. Because we truncate the cloud-phase in the ensemble to a binary variable (liquid or ice), the GDP2 ensemble (the mode among the products) can either agree with all three products or disagree with at most one (see Supporting Information 3.S8). Adding up the disagreement ratio for to each product, we find that the GDP2 ensemble disagrees with one of the three products 40% of the time and, therefore, all three products agree 60% of the time. However, the disagreement ratio is not evenly distributed across different temperatures. For the single products, the maximum disagreement ratio occurs at the average glaciation temperature (for which the FPR equals 0.5) and drops to zero towards higher and lower temperatures, closely resembling a "bell" curve (see Supporting Information 3.S1).

The highest disagreement is found at -22°C , where the GDP2 ensemble disagrees with the GOCCP, DARDAR and PM-L2 products 26%, 21% and 24% of the time, respectively. Therefore, the ensemble disagrees with one of the products 71% of the time. In other words, at -22°C , we would be almost as lucky trying to find an agreement between three coin tosses (disagreement of 75%) than between the three cloud top phase retrievals. At first, this may suggest that there is no safe way to tell which of the products is making the right decision. However, when independent products agree with each other (in our case, two of them always do), it is because different physical features are consistent with a certain phase. Therefore, it is reasonable to assume that the GDP2 ensemble is more reliable than the individual products. In fact, on average, no single pair of products agrees entirely (the lowest disagreement is 12% +

10% = 22% of the time between GOCCP and PM-L2), which reflects that the products are independent. Therefore, even when one of the products disagrees, the other two still provide a strong criterium to decide the cloud-phase. However, even if all three products always agree, there could be a bias shared by all products. Similarly, if one product always disagrees, it may still be more accurate than the other two.

The disagreement ratio of the single products is similar for both hemispheres (Fig. 3.3b). However, the disagreement ratio of the GOCCP and PM-L2 products is lower in the mid-latitudes than in the subtropics and high-latitudes, while the opposite occurs for the DARDAR product. As a result, in the mid-latitudes, the DARDAR product disagrees roughly twice as frequently with the GDP2 ensemble compared to the GOCCP and PM-L2 products. The PM-L2 product shows the lowest disagreement ratio with the GDP2 product (in the mid-latitudes and subtropics), the lowest bias (relative to GDP2), and the largest sample size. This suggests that, from all three cloud-phase products the PM-L2 product seems to be the most reliable.

3.3.2 Frequency Phase Ratio

The spaceborne lidar may fail to detect large ice particles, while the radar may detect a cloud even with very few ice particles. Therefore, the GOCCP product has the lowest FPR at all altitudes (except for Antarctica), while the DARDAR product has the highest FPR (Fig. 3.3c). The FPR from the PM-L2 product lays mostly between the other two products and agrees better with the GDP2 ensemble, arguably because the PM-L2 also relies on multiple physical features at cloud top to retrieve the cloud-phase.

All three products and the GDP2 ensemble have a higher FPR near the subtropics. For the GOCCP product, the FPR increases towards the equator by about +0.10 starting from 60°S and 70°N. For DARDAR, the FPR increases towards the subtropics (up to 40°S and 40°N) by about +0.20 starting at 70°S and 70°N, respectively. Finally, for PM-L2, the FPR increases by about +0.15 towards the equator but starting from 15°S and 15°N. As the sample size decreases towards Antarctica, fewer samples are available at the highest isotherms, which become underrepresented. Therefore, for all products, the vertical average shows an increase in FPR towards the south pole, with PM-L2 showing the steepest increase.

3.3.3 Hemispheric and seasonal contrast

To assess the north-south contrast, we locate the region containing north-south FPR differences larger than +0.2, which we call the "contrast" region. Specifically, we compare the average position of the contrast region in the temperature-latitude space for the different products. For lower temperatures, the fraction of liquid clouds will be also lower and, therefore, the north-south contrast of FPR tends to decrease, as fewer clouds can glaciate. To assess the magnitude of the contrast despite this tendency, we normalize the hemispheric contrast by the supercooled liquid frequency (SCF) in the southern hemisphere:

$$\Delta FPR/SCF = \frac{FPR_{dusty} - FPR_{clean}}{1 - FPR_{clean}} \quad (3.2)$$

Where *dusty* corresponds to the northern hemisphere (or spring season) and *clean* to the

../papers/fig.paper2/nh.contourNS.dust.hatch-eps-converted-to.pdf

../papers/fig.paper2/nh.contourMonth.dust.hatch-eps-converted-to.pdf

Figure 3.4: Contour plot enclosing the regions in the temperature-latitude space where (a) the normalized north-south difference in FPR at cloud top (Eq. 3.2) is higher than +0.2 and (b) the normalized seasonal difference in FPR between MAM(SON) and SON(MAM) in the northern(southern) hemisphere is higher than +0.1. The hatched region corresponds to the zone where all products have a north-south(seasonal) contrast higher than +0.2(+0.1). The dashed contour encloses the regions where the dust loading is (a) 50 times higher in the northern hemisphere (b) 3 times higher during spring. A Gaussian filter was applied to smoothen the contours.

southern hemisphere (or fall season). Thus, the normalized contrast represents the fraction of liquid clouds in the southern hemisphere that would glaciate in the northern hemisphere environment. Additionally, to compare the cloud-phase with the dust-aerosol contrast, we locate the region for which the dust concentration in the northern hemisphere is on average more than 50 times higher than in the southern hemisphere. Moreover, we note that already above 10°N the dust concentration is at least 10 times higher than in the southern hemisphere (not shown).

Fig. 3.4 shows the location of the hemispheric and seasonal contrast of cloud-phase for the different products and the GDP2 ensemble. For all products, the contrast region is mostly located below -20°C (Fig. 3.4a). This result partly disagrees with other studies based on CALIOP and on the CPR, which have located the highest north-south contrast between -10°C and -15°C (Tan et al., 2014), and between -15°C and -20°C (Zhang et al., 2018). Nevertheless, the radar reflectivity used in Zhang et al. (2018) is meant to detect ice production (size and number) and is not a direct proxy for cloud top phase. On the other hand, the cloud-phase retrievals in Tan et al. (2014) use a different methodology (Choi et al., 2010) than for the GOCCP product (Cesana & Chepfer, 2013). The magnitude of the north-south contrast is also higher than previous estimates, where the contrast was reported to be about $+0.05$ FPR between -20°C and -30°C (Tan et al., 2014, for a more accurate comparison, please refer to the non-normalized contrast in the Supporting Information 3.S2). For the DARDAR and PM-L2 products, the contrast at 60°N/S extends up to about -12°C and -17°C , respectively. This may be related to the dust aerosol contrast, which is higher between 60 – 70°N/S , mainly because of the very low concentrations over the Southern Ocean. However, the most notable difference between the products is the meridional extent of the contrast region. Towards the pole, the contrast region extends up to at least 70°N/S for all products; but towards the equator, the contrast extends down to 15°N/S , 25°N/S , and 40°N/S for the GOCCP, DARDAR and PM-L2 products, respectively.

The North-South contrast in FPR is attributed by several authors to the hemispheric difference in aerosol loading (Kanitz et al., 2011; Tan et al., 2014; J. Li et al., 2017; Zhang et al., 2018; Villanueva et al., 2020). More specifically, it is attributed to the higher concentration of INP-active mineral dust aerosol in the northern hemisphere, mostly from the Sahara and Gobi deserts. However, the dust aerosol concentration in the northern hemisphere varies seasonally, with a peak during spring (Zender & Kwon, 2005; Cowie et al., 2014). For this reason, we also analyzed the average FPR differences between the months of March-April-May (MAM) and September-October-November (SON). We defined the contrast regions where the MAM-SON(SON-MAM) difference in FPR is higher than $+0.1$ in the northern(southern) hemisphere. For the northern(southern) hemisphere, we normalize the seasonal contrast by the fraction of liquid clouds in SON(MAM). Additionally, we locate the regions for which the dust loading is at least three times higher during spring compared to autumn. Similar to the hemispheric contrast, the seasonal cloud-phase contrast is mostly located below -20°C for all products (Fig. 3.4b), in agreement with previous reports (Tan et al., 2014). In the northern mid-latitudes, for DARDAR the seasonal contrast extends up to about -12°C , while for GOCCP it extends only up to -22°C . On the other hand, the meridional location of the seasonal contrast is very similar

between the products, extending mostly from 30°N to 80°N. These contrasts, especially for the GOCCP product, have a "bow-tie" form, which is possibly related to the seasonal contrast of dust-aerosol. In the southern hemisphere, between -31°C and -25°C , the PM-L2 product and the GDP2 ensemble show a seasonal contrast near 40°S.

We can retrieve some interesting features from the location of the hemispheric and seasonal contrast of cloud top phase. First, the GDP2 ensemble agrees best with the DARDAR product on the location of the hemispheric contrast, and with the PM-L2 product on the location of the seasonal contrast. Second, the "overlap" zone, where all three products show a hemispheric or seasonal contrast, lays mostly between -35°C and -25°C and between 40–70°N. At this temperature, most types of mineral dust act as efficient INP (Murray et al., 2011; Broadley et al., 2012; Boose et al., 2016). The overlap zone also coincides with the region where the contrast reaches a maximum for the GDP2 ensemble (see Supporting Information 3.S3). Therefore, this high-contrast region offers a good target for future campaigns looking to study the north-south contrast in cloud glaciation.

3.3.4 Quantification and attribution

We can use the GDP2 ensemble to identify the temperature range where individual cloud-phase products may be biased. In Sect. 3.3.2, it was shown that in the mid-latitudes the DARDAR product overestimates the FPR (by +0.16) relative to the GDP2 ensemble, while the GOCCP product underestimates the FPR (by -0.05). Fig. 3.5 shows the frequency of ice cloud-tops, as well as the magnitude of the hemispheric- and seasonal contrast of cloud-phase in the mid-latitudes. In Fig. 3.5a, we can see that the overestimation of the DARDAR product occurs mainly for temperatures above -25°C , while for the GOCCP product the underestimation occurs mostly for temperatures below -15°C .

By using only retrievals where all products agree on cloud-phase, we find that the cloud-phase transition occurs within a narrower temperature range. We recall that in the GDP2 ensemble, the cloud-phase is defined as long as all three individual products are available, even if they disagree. Alternatively, one can select only volume-gridboxes where all three products agree, which we call GDP3. As mentioned above, all three products agree on average only 60% of the time. For both GDP2 and GDP3, at -22°C half of the cloud-tops are classified as ice (Fig. 3.5a). In the GDP3 ensemble, the cloud top phase transition is steeper and occurs only between -35°C and -10°C , while for GDP2 it occurs between -38°C and 0°C . The difference between the GDP2 and GDP3 ensembles can also be used to identify the clouds which the products disagree upon. As can be seen from the difference in ice frequency between GDP2 and GDP3 (Fig. 3.5a), these are mostly liquid clouds below -22°C and ice clouds above -22°C (as classified in the GDP3 ensemble), especially at -28°C and -16°C , respectively. These clouds may relate to some of the scenarios discussed in Sect. 3.2.1.

The hemispheric and seasonal contrast in cloud-phase tends to increase at lower temperatures. In the mid-latitudes, for temperatures higher than -10°C , the hemispheric and seasonal contrasts in cloud-phase is close to zero for all products (Fig. 3.5b-c). From -10°C to -30°C , both the hemispheric and seasonal contrast increases for all individual cloud products. Moreover, for the GDP2 and GDP3 the increase is higher than for the individual products. For

```
../papers/fig.paper2/temp.fpr-eps-converted-to.pdf
```

```
../papers/fig.paper2/temp.NSnorm-eps-converted-to.pdf
```

```
../papers/fig.paper2/temp.MAMnorm-eps-converted-to.pdf
```

Figure 3.5: (a) Average frequency of ice cloud tops (FPR) at the mid-latitudes 30-60°N/S. (b) Average north-south FPR difference at cloud top normalized by the supercooled liquid frequency (SCF) in the southern hemisphere. (c) Average seasonal FPR difference (MAM – SON) at cloud top at 30-60°N normalized by the SCF during SON. Only values for which the reference SCF is higher than 0.05 are shown.

temperatures below than -30°C , the contrasts tend to decrease for the individual products. This decrease in the seasonal and hemispheric contrast for temperatures below -30°C may be explained by the depletion of INP at higher altitudes.

The increase of cloud-phase contrast at lower temperatures coincides with the increasing effectivity of dust-INP at lower temperatures. From -15°C to -25°C , both the seasonal and hemispheric contrast increase for all products by at least $+0.15$ (Fig. 3.5b-c). This increment is even higher for the GDP2 (hemispheric: $+0.33$; seasonal: $+0.41$) and GDP3 ensemble (hemispheric: $+0.59$; seasonal: $+0.56$). This increase of the contrast for lower temperatures suggests that it may be driven by INP efficiency, which increases exponentially for decreasing temperature. In fact, as previously mentioned, dust INP generally starts to activate within this temperature range (Boose et al., 2016; Kanji et al., 2017; Niemand et al., 2012), and dust loading is higher in the northern-hemispheric spring (Cowie et al., 2014).

In other types of aerosol-cloud-interactions, such as the effect of cloud condensation nuclei on warm clouds, meteorological factors have been shown to dominate over the effect of aerosols (Gryspeerdt et al., 2016). In fact, meteorological factors such as wind speed and thermal stability may vary between hemispheres due to land-ocean distribution and affect the cloud ice frequency (J. Li et al., 2017). However, we also observe a cloud-phase contrast between spring and fall in the Northern Hemisphere, which is unlikely to be explained by the seasonal variability of such meteorological factors.

3.3.5 Uncertainty

For the individual products, the uncertainty associated with the hemispheric cloud-phase contrast arise mainly from retrieval issues in the GOCCP product and from the seasonal variability in PM-L2. Table 3.1 summarizes the uncertainty associated with each product. For $2^{\circ}\times 30^{\circ}$, the uncertainty in FPR is higher for GOCCP (± 0.13 ; sample size $n=64640$) than for DARDAR (± 0.05 ; $n=58289$). This higher uncertainty in GOCCP appears to be associated with a lower FPR from CALIOP during 2007, before the off-nadir angle was adjusted to decrease the specular reflection from ice crystals, which resulted in a bias in the detection of cloud-phase (Avery et al., 2020, see also Supporting Information 3.S9). In addition, the uncertainty for PM-L2 (± 0.04 ; $n=662690$) is similar to DARDAR despite a much higher sample size. This suggests that the error introduced from the monthly aggregation of FPR_{daily} (binary distributed; see Eq.3.1) cannot alone explain the differences in the spread of FPR for the different products. Table 3.2 summarizes the uncertainty associated with the hemispheric contrast in cloud-phase. The uncertainty in $\Delta FPR/SCF$ increases relative to FPR, partially due to the accumulation of error from both hemispheres. Particularly, for PM-L2, the standard deviation of $\Delta FPR/SCF$ is almost three times higher compared to FPR. We attribute this high uncertainty to the higher summer-winter variability of FPR in the PM-L2 product at $30\text{-}60^{\circ}\text{S}$ (See Supporting Information 3.S10), which leads to very low or negative hemispheric contrasts during boreal summer.

For the GDP ensembles, low sample sizes seem to result in a high uncertainty in the cloud-phase contrast. For the GDP2 ensembles ($2^{\circ}\times 30^{\circ}\text{grid}$), the uncertainty associated with FPR and $\Delta FPR/SCF$ is inside the range observed for the individual products. However, the uncertainty associated with GDP3 is higher than for GDP2, probably due to a lower sample size (see again

Grid lat×lon	n $2^\circ \times 2^\circ$	$2^\circ \times 30^\circ$	FPR $2^\circ \times 2^\circ$	$2^\circ \times 30^\circ$	de-trended (2008-2009)
GOCCP:	83097	64640	0.45 ± 0.12	0.41 ± 0.13	0.52 ± 0.03
DARDAR:	77774	58289	0.62 ± 0.05	0.61 ± 0.05	0.63 ± 0.02
PM-L2:	662690	157020	0.60 ± 0.04	0.56 ± 0.04	0.63 ± 0.05
GDP-2:	1070	15632	0.66 ± 0.16	0.52 ± 0.08	0.64 ± 0.05
GDP-3:	262	4027	0.75 ± 0.24	0.55 ± 0.14	0.74 ± 0.09

Table 3.1: Table showing the sample size n and Frequency Phase Ratio (FPR) of the individual cloud products and the GDP ensembles for two different grid choices. The dataset includes the samples within the 30-60°N latitude band, at -22°C. The estimated error corresponds to the monthly standard deviation during 2007-2010. For the de-trended dataset, the error corresponds to the standard deviation between the 12 monthly differences between 2008 and 2009.

Grid lat×lon	$\Delta FPR/SCF$ $2^\circ \times 2^\circ$	$2^\circ \times 30^\circ$	de-trended (2008-2009)
GOCCP:	0.16 ± 0.11	0.15 ± 0.13	0.22 ± 0.06
DARDAR:	0.23 ± 0.08	0.25 ± 0.10	0.27 ± 0.07
PM-L2:	0.20 ± 0.19	0.21 ± 0.21	0.20 ± 0.16
GDP-2:	0.43 ± 0.36	0.31 ± 0.11	0.36 ± 0.12
GDP-3:	0.79 ± 0.40	0.52 ± 0.17	0.58 ± 0.16

Table 3.2: As Table 3.1, but for $\Delta FPR/SCF$, the normalized hemispheric contrast (30-60° N/S).

Eq.3.1). Similarly, the uncertainty for the GDP ensembles increases for finer grids, because the lower horizontal overlap between products in such grids results in a lower sample size. Due to this lower sample size, the uncertainty in FPR is about twice as high for the $2^\circ \times 2^\circ$ grid compared to the $2^\circ \times 30^\circ$ grid for both GDP2 and GDP3. For the normalized hemispheric contrast $\Delta FPR/SCF$, the uncertainty is about three times as high for $2^\circ \times 2^\circ$ compared to $2^\circ \times 30^\circ$. In summary, the GDP2 ensemble within a $2^\circ \times 30^\circ$ grid produces the most accurate estimation of the hemispheric contrasts (± 0.11).

The variability from the seasonal cycle affects the uncertainty in FPR, but not the uncertainty in $\Delta FPR/SCF$ from the GDP ensembles. To estimate the uncertainty associated with the de-trended dataset, we use the difference between each month of the year during 2008-2009. This excludes the seasonal variability and errors associated with the GOCCP product during 2007, as well as missing data from PM-L2 during 2010 (See Supporting Information 3.S9). Therefore, the variability of the de-trended dataset can better represent the uncertainty associated with each product. For all individual products, the de-trended dataset has a lower uncertainty in FPR and $\Delta FPR/SCF$. For PM-L2 the uncertainty of the de-trended FPR and $\Delta FPR/SCF$ is at about twice as high compared to GOCCP and DARDAR. For the GDP2 and GDP3 ensembles, only the uncertainty in FPR decreases after de-trending, while the uncertainty in $\Delta FPR/SCF$ does not change significantly. This suggests that for GDP2 and GDP3 the uncertainty in the hemispheric contrast is less affected by the seasonal variability and trends in the individual products.

3.4 Conclusions

Throughout the analysis, we used an ensemble of the GOCCP, DARDAR and PM-L2 cloud top phase products as a reference to assess the confidence on the individual products. We attribute

the differences between the FPR from the individual products to retrieval biases associated with each instrument. Such biases are related to the retrieval methods and the wavelength used, but also to cloud optical properties like particle size and optical depth.

We have shown that the GDP ensembles and the individual products mostly agree on the existence and location of the hemispheric and seasonal contrast in cloud top phase. These contrasts are centered near -30°C and between 50° – 60°N . At -30°C , using the GDP ensemble we find that, on average, half of the liquid cloud tops found in the southern mid-latitudes glaciate in the northern mid-latitudes. We find similar results for the seasonal contrast (spring relative to fall), though only in the northern hemisphere. In addition, the magnitude of the cloud-phase contrasts seems to be underestimated by the individual products. The location of the hemispheric and seasonal contrasts in cloud top phase are consistent with the contrasts in dust aerosol loading, which provides additional evidence of the global role of aerosol in controlling the variability of cloud-phase. By constraining the spatio-temporal variability of cloud-phase, we expect to improve the general understanding of the atmospheric differences between hemispheres. The new metric for quantifying the contrasts may help to elucidate the differences in cloud-phase and the radiative balance between hemispheres, as well as their relationship with aerosols and cloud glaciation. By locating the north-south and seasonal contrast of cloud top phase, we also provide a potential target for future in-situ campaigns looking to clarify the processes behind cloud glaciation.

In future studies, the hemispheric and seasonal contrast in cloud-phase may be used to constrain cloud glaciation, heterogeneous freezing rates, and the impact of dust INP in global climate models. Additionally, this new benchmark can be used to evaluate different climate models and different parameterizations of heterogeneous freezing from a large-scale perspective.

3.S Supporting Information for "Hemispheric and seasonal contrast of cloud phase from the A-Train"

Data Set 3.S1: GDP Ensemble dataset on $2^\circ \times 30^\circ$ grid

<https://catalogue.ceda.ac.uk/uuid/f742c505c935467ebb4cf89a611a4436>

This dataset contains a collocation of the three different A-Train cloud phase products on a $2^\circ \times 30^\circ$ grid (latxlon). The top pixels of each product were selected and binned into 3 K temperature intervals. The GDP2 ensemble was produced using the mode between the three different binary classifications (ice/liquid), provided that all three products are available at each timestep. The GDP3 ensemble is a subselection of the GDP2 ensemble, containing only timesteps where all three products agree. The GP(GOCCP-PM-L2), DP(DARDAR-PM-L2) and GD(GOCCP-DARDAR) ensembles contain only timesteps where two products agree.

../papers/fig.paper2.si/temp.sample-eps-converted-to.pdf

../papers/fig.paper2.si/temp.error-eps-converted-to.pdf

Figure 3.S1: Global average of the (a) Sample size in days (b) Disagreement ratio for the individual cloud-phase products relative to the GDP2 ensemble against temperature.

```
../papers/fig.paper2.si/NS.nonnorm-eps-converted-to.pdf
```

```
../papers/fig.paper2.si/NS.two-eps-converted-to.pdf
```

Figure 3.S2: Contour plot enclosing the regions in the temperature-latitude space where the absolute (non-normalized) north-south difference in FPR at cloud top is higher than +0.1. The hatched region corresponds to the zone where all products have a north-south contrast higher than +0.1. A Gaussian filter was applied to smoothen the contours. The GP(GOCCP-PM-L2), DP(DARDAR-PM-L2) and GD(GOCCP-DARDAR) ensembles contain only timesteps where two products agree. The dotted contour encloses differences higher than +0.3.

../papers/fig.paper2.si/NS.gdp2-eps-converted-to.pdf


../papers/fig.paper2.si/MAM.gdp2-eps-converted-to.pdf

Figure 3.S3: Contour plot in the temperature-latitude space for (a) the normalized north-south difference in FPR at cloud top and (b) the normalized seasonal difference between MAM(SON) and SON(MAM) in the northern(southern) hemisphere. The contrasts are normalized by the supercooled liquid frequency in (a) the southern hemisphere (b) SON(MAM) season in the northern(southern) hemisphere. A Gaussian filter was applied to smoothen the contours.

../papers/fig.paper2.si/temp.double.ensemble-eps-converted-to.pdf


../papers/fig.paper2.si/temp.double.products-eps-converted-to.pdf

Figure 3.S4: Average north(Spring only)-south FPR difference at cloud top normalized by the supercooled liquid frequency (SCF) in the southern hemisphere. For the northern hemisphere only March, April and May are included. Only values for which the reference SCF is higher than 0.05 are shown.



../papers/fig.paper2.si/bin.grid-eps-converted-to.pdf

Figure 3.S5: Diagram showing the horizontal binning of the satellite retrievals from 0 UTC to 0 UTC.



../papers/fig.paper2.si/bin.ray-eps-converted-to.pdf

Figure 3.S6: Diagram showing how the cloud top phase is selected, averaged and truncated within a gridbox (See Fig. 3.S5).

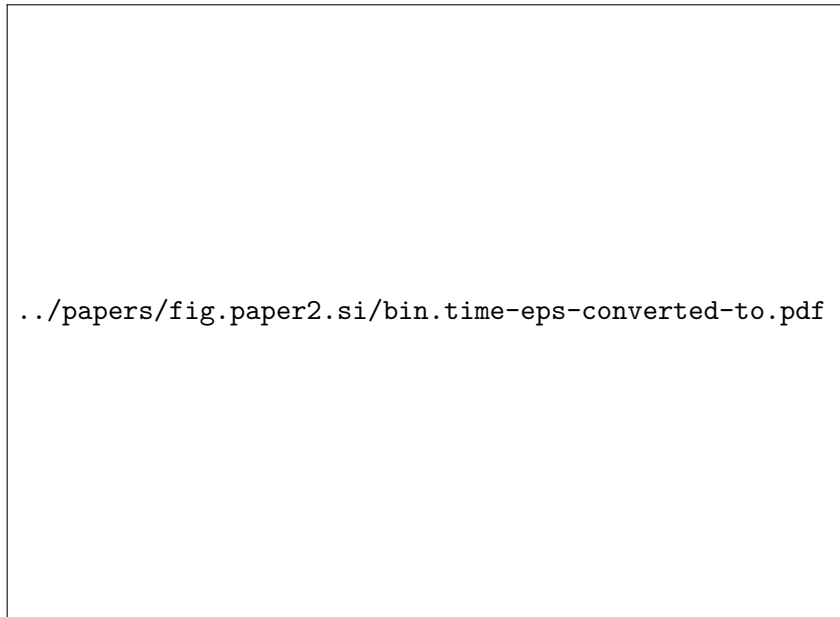


Figure 3.S7: Diagram showing how the profiles of cloud top phase are averaged in time within a gridbox.

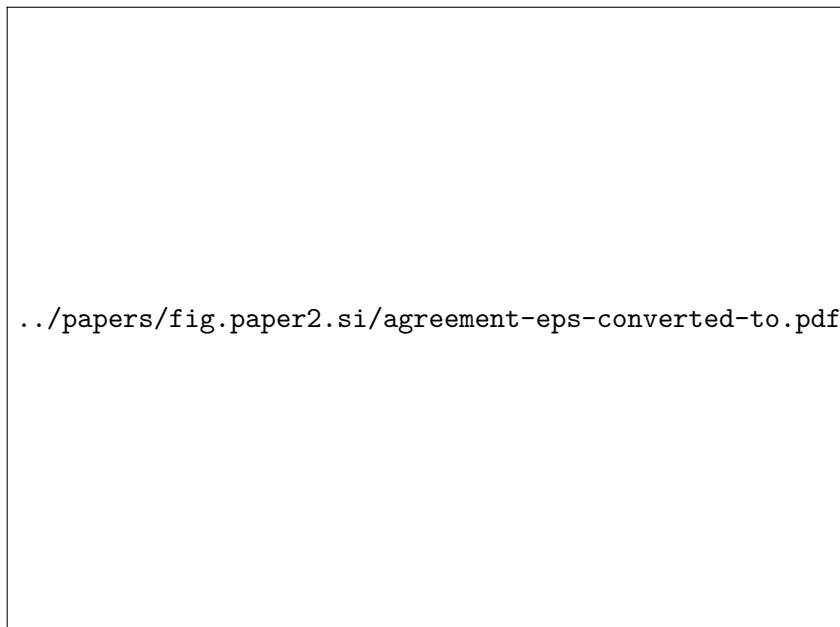


Figure 3.S8: Visualization of the different possible agreements between the individual cloud phase products and the GDP ensembles.

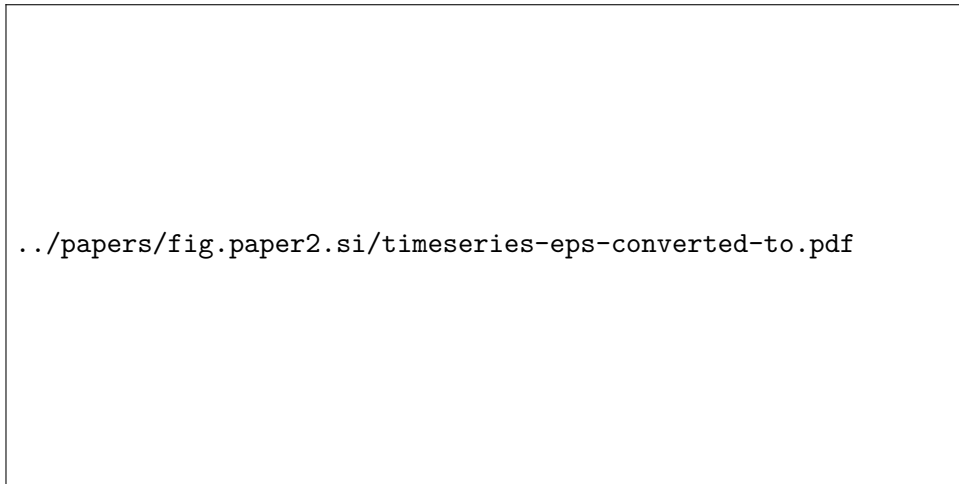


Figure 3.S9: Timeseries of the ice cloud frequency 2007-2010 at -22°C and 30-60°N.



Figure 3.S10: Timeseries of the ice cloud frequency 2007-2010 at -22°C and 30-60°S.

Chapter 4

Constraining the impact of dust-driven droplet freezing on climate using cloud top phase observations*

After decades of development, atmospheric models still struggle when simulating aerosol-driven cloud glaciation, leading to high uncertainty in climate predictions and weather forecasts. So far, research has followed a bottom-up approach: measuring the freezing efficiency of various aerosol types in the laboratory and extrapolating their behaviour into the real atmosphere, which results in poor agreements with observations of cloud-phase variability. Although we use the same theoretical framework for droplet freezing, we use a simplified top-down approach: In the model, only dust aerosol acts as ice-nuclei, and its efficiency is used as a tuning parameter. We find that by assuming that dust aerosol freezes at about 10 K warmer temperatures compared to what is currently assumed in the model, the spatio-temporal variability of cloud-phase agrees much better with observations. This agreement further improves if only high concentrations of dust are allowed to trigger freezing, which prevents much of the dust-driven cloud glaciation during clean conditions. We find that the default model led to an overestimation of the indirect radiative effect due to dust ice-nuclei compared to the tuned-model, which uses the top-down approach proposed here. In conclusion, our approach presents a pragmatic alternative to the current bottom-up approach for constraining dust-driven cloud glaciation, which will help to direct future modelling efforts in the right direction.

*Chapter based on: Villanueva, D., Neubauer, D., Gasparini, B., Ickes, L., and Tegen, I. (2021). Constraining the impact of dust-driven droplet freezing on climate using cloud top phase observations. Accepted to Geophysical Research Letters (with modifications).

4.1 Introduction

Aerosol-cloud interactions, especially for ice and mixed-phase clouds, are a major source of uncertainty for predicting weather and climate change (Forbes & Ahlgrimm, 2014; McCoy et al., 2016; Bellouin et al., 2020). On average, clouds cool the planet; however, the Cloud Radiative Effect (CRE) depends strongly on the number and size of hydrometeors (Seinfeld et al., 2016). Particularly, cloud optical thickness is tied to the hydrometeor surface area. Thus, a cloud with a large number of small hydrometeors will be more reflective compared to a cloud of the same condensed water content composed of a small number of large hydrometeors (Twomey, 1974). Moreover, a cloud composed of larger hydrometeors will be shorter-lived: the larger hydrometeors will precipitate faster out of the atmosphere (Albrecht, 1989).

Ice Nucleating Particles (INP) can trigger droplet freezing between 0°C and -35°C (Hoose & Möhler, 2012); subsequently, ice particles grow at the expense of depleting liquid cloud droplets (Wegener, 1911; Bergeron, 1935; Findeisen et al., 2015). The number of ice particles is typically orders of magnitude smaller compared to the number of cloud droplets and their size is several times larger than the typical cloud droplet size. Therefore, at temperatures warmer than -35°C , INP-driven droplet freezing is associated with less reflecting clouds and a warming effect on climate (IPCC et al., 2007; Lohmann & Diehl, 2006; Yun et al., 2013; Yun & Penner, 2013; Shi & Liu, 2019).

In climate models, droplet freezing schemes are either based on field measurements (e.g., DeMott et al., 2010), laboratory measurements (e.g., Lohmann & Diehl, 2006; Niemand et al., 2012), or theoretical frameworks, such as Classical Nucleation Theory (CNT; Hoose et al., 2010; Ickes et al., 2017). In this study, we compare two laboratory-based freezing schemes for immersion freezing that have been already tested with the ECHAM-HAM climate model (Hoose et al., 2008; Ickes, 2015; Huang et al., 2018).

Although many natural and anthropogenic aerosols are known to act as INP, most evidence suggests that cloud glaciation is dominated by mineral dust (Tan et al., 2014; Vergara-Temprado et al., 2017; Zhang et al., 2018; Villanueva et al., 2020; Kawamoto et al., 2020). Ice cloud frequency and mineral dust concentrations observed from space are higher in the Northern Hemisphere, as well as during boreal and austral spring (Y. Hu et al., 2010; Cowie et al., 2014; Tan et al., 2014, 2014; Villanueva, Senf, & Tegen, 2021; Zhang et al., 2018; M. Wu et al., 2020; Bruno et al., 2021). In addition, dust emissions may have increased by about 25% since pre-industrial times due to land use change (Stanelle et al., 2014). Therefore, to better understand the impacts of current atmospheric dust and of climate change, it is essential to better constrain the radiative effect of dust-driven cloud glaciation (Shi & Liu, 2019).

Previous studies have relied on atmospheric state observations of dust-loading (Shi & Liu, 2019) and ice cloud frequency (Tan et al., 2016) to constrain cloud glaciation. However, it has been postulated that observational constraints on process rates can lead to a better estimation of aerosol-cloud interactions (Mülmenstädt et al., 2020). Therefore, in this study we use the hemispheric and seasonal contrast of cloud-top-phase based on satellite observations to constrain dust-driven immersion freezing and its impact on climate in ECHAM-HAM.

../papers/fig.paper3/diagram-eps-converted-to.pdf

Figure 4.1: Diagram explaining the strategy behind each group of simulations towards improving the simulated contrast in cloud-top-phase. First row: freezing ("frz") scheme; second row: simulations that are compared within each group; third row: parameter of interest for each group; fourth row: constrained parameter from each comparison providing the best agreement with observations.

4.2 Methods

4.2.1 Model description

For our study, we use a state-of-the-art atmospheric model able to represent aerosol-cloud interactions with sufficient detail. The aerosol-climate model ECHAM(v6.3.0)-HAM(v2.3) (Neubauer et al., 2019; Tegen et al., 2019) is coupled to the Predicted bulk Particle Properties (P3) microphysical scheme newly implemented in ECHAM- HAM (H. Morrison & Milbrandt, 2015; Dietlicher et al., 2019, 2018) with the "2M" tuning configuration (Dietlicher et al., 2018). The nudged simulations were performed for the period 2003-2012 using 31 vertical model layers, a horizontal resolution of 1.875° (T63), and interactively computed dust emissions (Tegen et al., 2019, see Supporting Information Text 4.S2).

4.2.2 Satellite simulator and A-Train observations

To enable a direct comparison between model and observations, we use a satellite simulator and two different satellite phase products. The CFMIP Observation Simulator Package (COSP; Bodas-Salcedo et al., 2011) was used in the model to recreate the satellite retrievals of cloud-phase. The GCM-Oriented CALIPSO Cloud Product (CALIPSO-GOCCP; Chepfer et al., 2010; Cesana & Chepfer, 2013) is a cloud-phase product based on spaceborne lidar retrievals and is the counterpart to the COSP simulator. To account for potential biases in the GOCCP product and provide a margin of error for the observations, we also included the GDP (GOCCP-DARDAR-PML2) product ensemble (Villanueva, Senf, & Tegen, 2021).

4.2.3 Freezing schemes

The heterogeneous freezing scheme in the reference version of ECHAM-HAM is the Lohmann-Diehl scheme (LD; Lohmann & Diehl, 2006; Hoose et al., 2008), which is based on wind tunnel experiments. In this parameterization, the immersion freezing rate J_{imm} depends on the dust particle number concentration in the soluble mode $N_{imm,dust}$, temperature (T), Turbulent Kinetic Energy (TKE) and on the number concentration of ambient Cloud Condensation Nuclei (CCN; Lohmann et al., 2007). The immersion freezing rate is calculated as:

$$J_{imm} = N_a \cdot c_{dust} \frac{N_{imm,dust}}{CCN} e^{N_a \cdot (273.15 \text{ K} - T)} \frac{dT}{dt} \frac{\rho_{air} \cdot q_l}{\rho_l} [\text{m}^{-3} \text{s}^{-1}], \quad (4.1)$$

$$\frac{dT}{dt} = \frac{\omega_{largescale} - 0.7\sqrt{TKE} \cdot \rho_{air} \cdot g}{c_p \cdot \rho_{air}}. \quad (4.2)$$

with $\omega_{largescale}$ the large-scale term from the vertical velocity, q_l the cloud liquid water mass-mixing ratio, ρ_{air} the air density, ρ_l the cloud droplet density, g the gravitational constant, c_p the specific heat of air, and $N_a = 1 \text{ K}^{-1}$. The freezing efficiency ($c_{dust} = 32.3$) is assumed to have the freezing efficiency of montmorillonite in the reference configuration (Hoose et al., 2008).

The second freezing scheme used in this study is based on cloud chamber experiments (NS; e.g., Connolly et al., 2009; Niemand et al., 2012; Ickes et al., 2017; Huang et al., 2018). In this parameterization, the fraction of frozen droplets FF increases linearly with the dust particle surface area A_j and the ice active surface site density of natural dust n_s , which depends on the aerosol characteristics N_A and N_B , with:

$$FF \approx A_j \cdot n_s(T), \quad (4.3)$$

$$n_s(T) = e^{N_A \cdot (273.15 \text{ K} - T + N_B)} [\text{m}^{-2}]. \quad (4.4)$$

Similar to the LD scheme, we set the temperature dependence ($N_A = 1 \text{ K}^{-1}$) and temperature offset ($N_B = -5 \text{ K}$) as observed for montmorillonite (see Supporting Information 4.S1). In addition, to assess the sensitivity of the freezing scheme to different INP efficiencies, we increased the temperature offset N_B for which dust can trigger immersion freezing by +10 K for simulations **NS10K** and **NS-Tuned**. The temperature shift is equivalent to increasing INP concentrations by about four orders of magnitude (see Eq. 4.4).

Although both the LD and NS schemes represent the same process of immersion freezing, the LD scheme predicts a freezing rate while the NS scheme predicts a fraction of frozen droplets. The NS scheme is deterministic and time-independent, so that droplet freezing stops after the predicted number of frozen droplets is reached (Ickes, 2015). In contrast, in the LD scheme, the freezing rate is a time-dependent prognostic quantity and does not consider the number of already frozen droplets (Hoose et al., 2008).

In general, climate models do not keep track of INPs directly. Therefore, INPs that have been already activated are not removed for future iterations. Consequently, it may be useful to introduce a threshold to limit droplet freezing in clean conditions. In such conditions, the few INP that may have been present are probably already depleted or deactivated by aging processes such as sulfate coating (Cziczo et al., 2009).

4.2.4 Model Simulations

We can separate the simulations in this study in three major groups, each addressing a different aspect of the immersion freezing parameterization: scheme type (group I), INP efficiency (group II), and dust threshold (group III). Fig. 4.1 shows this structure, together with the tuning strategy behind it. Additional simulations for group II and group III with different parameter values can be found in the Supporting Information (Table 4.S1 and Fig. 4.S3–4.S5).

In the **NoFRZ** simulation, heterogeneous freezing is turned off, but droplets are converted to ice at -35°C (homogenous freezing). The **LD** and **NS** simulations use the LD and NS scheme, respectively, and assume the INP efficiency of the clay mineral montmorillonite. In the **NS10K** simulation, shifting N_B by $+10\text{ K}$ causes dust-INP to freeze at temperatures 10 K warmer compared to the **NS** simulation. The **NS-Tuned** simulation is based on the **NS10K** simulation, but only dust number concentrations higher than 10^6 kg^{-1} are considered for droplet freezing.

4.2.5 Quantifying cloud glaciation and cloud-top-phase contrasts

To isolate the impact of each freezing parameterization on cloud-top-phase, we compare each simulation with a reference scenario, where droplets only freeze at temperatures colder than -35°C . We define the fraction of *dust-driven* glaciated cloud tops (“glaciated fraction”) as the difference between the Cloud-top Ice Frequency (CIF) for each simulation and the **NoFRZ** simulation, normalized by the frequency of liquid clouds in **NoFRZ** at each temperature.

$$\text{Glaciated fraction} = \frac{CIF_{simulation} - CIF_{NoFRZ}}{1 - CIF_{NoFRZ}} \quad (4.5)$$

We focus on the mid-latitudes, since here the hemispheric and seasonal variability of cloud-phase is higher (Villanueva, Senf, & Tegen, 2021; Zhang et al., 2018), and the radiative effect of dust-INP is stronger compared to the high-latitudes and subtropics (between -35°C and 0°C ; Shi & Liu, 2019; Lohmann & Diehl, 2006).

To quantify and evaluate the hemispheric and seasonal contrast in cloud-top-phase against observations, we normalize the contrast in cloud-top ice frequency (spring–fall or north–south) by the liquid cloud frequency in the “clean” part of the contrast (i.e., where dust loading is low, as during fall or in the Southern Hemisphere). To avoid artifacts from low sample sizes, we only use the observed cloud-top-phase contrast for temperatures where the liquid cloud frequency is higher than 10%.

$$\text{Cloud-phase contrast} = \frac{CIF_{dusty} - CIF_{clean}}{1 - CIF_{clean}} \quad (4.6)$$

$$dusty - clean = \begin{cases} north - south, & \text{hemispheric} \\ spring - fall, & \text{seasonal} \end{cases} \quad (4.7)$$

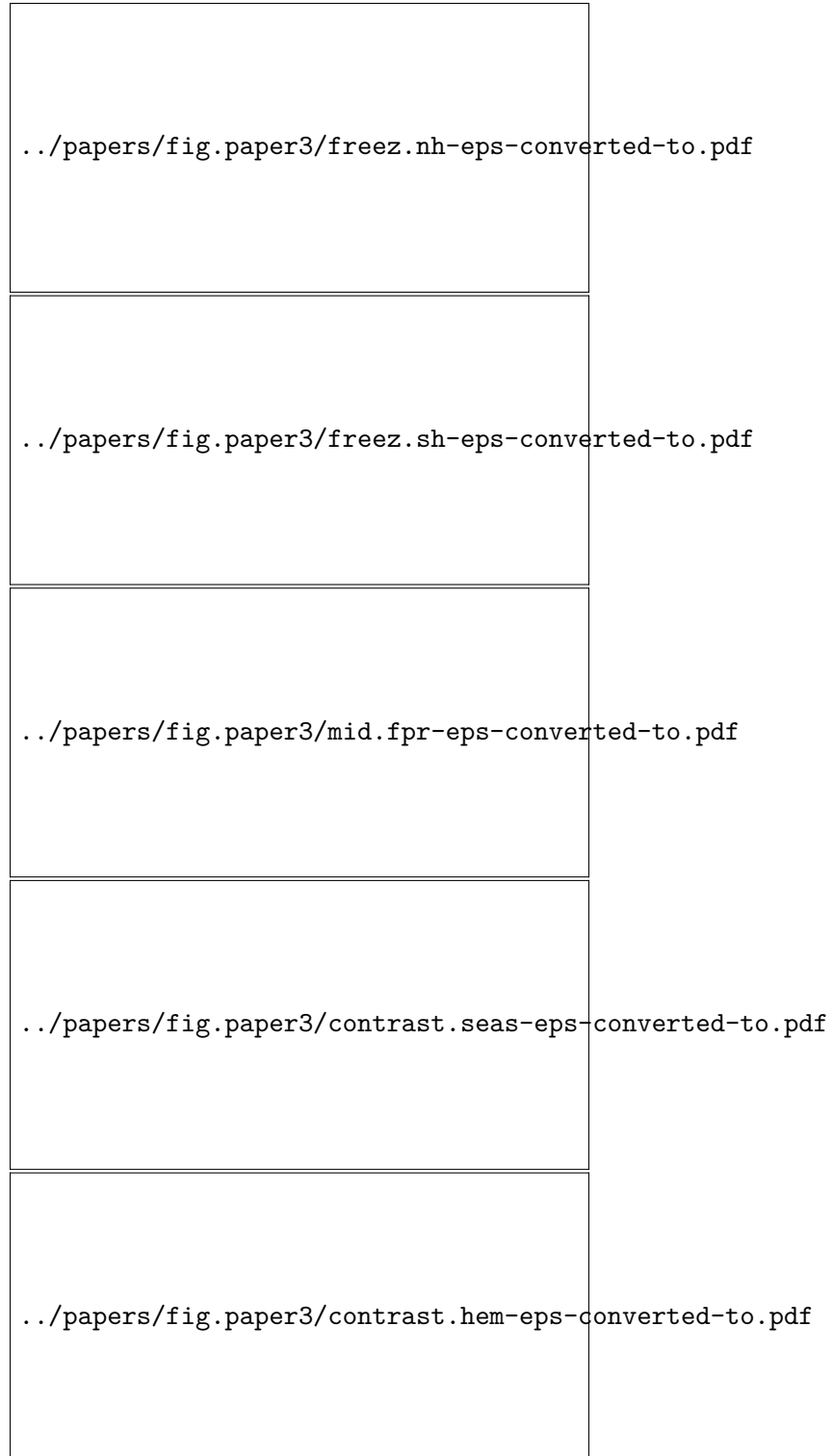


Figure 4.2: (a–b) Fraction of the liquid clouds (in the NoFRZ simulation) that glaciate in each simulation at (a) 30–60°N and (b) 30–60°S. (c) Cloud-top Ice Frequency (CIF) at the mid-latitudes. (d) Fraction of clouds additionally glaciated at 30–60°N during spring (compared to fall) normalized by the fraction of liquid clouds during fall. (e) Fraction of clouds additionally glaciated at 30–60°N (compared to 30–60°S) normalized by the fraction of liquid clouds at 30–60°S. The limit of the observations corresponds to the GOCCP product and GDP ensemble (dashed), respectively (2007-2010). Each datapoint corresponds to a 3 K temperature bin.

4.3 Results

4.3.1 Dust-driven cloud glaciation

The dust loading at each hemisphere and the choice of freezing scheme affects how many clouds glaciate, especially for temperatures colder than -15°C . Fig. 4.2a–b shows the fraction of cloud liquid tops that glaciate due to dust-INP for each simulation in the mid-latitudes. For temperatures colder than -35°C , all droplets are forced to freeze in the model, causing the dust-driven glaciated fraction to drop (not shown). For temperatures warmer than -15°C , the INP efficiency is often too low for dust aerosol to glaciate liquid clouds and the glaciated fraction drops to zero as well. Between $30\text{--}60^{\circ}\text{N}$, the fraction of dust-driven glaciated clouds tops is almost identical for the **LD** and **NS** simulations, increasing from -25°C until -35°C (Fig. 4.2a). In addition, for all simulations, fewer cloud tops glaciate at $30\text{--}60^{\circ}\text{S}$ compared to $30\text{--}60^{\circ}\text{N}$ (Fig. 4.2b). However, for **LD** this hemispheric difference in cloud glaciation is weaker compared to the simulations using the **NS** scheme (Fig. 4.2e). This hemispheric contrast in **NS** is a result of the higher aerosol dust loading in the Northern Hemisphere, which is the only variable controlling the droplet freezing rate in the **NS** scheme besides temperature. In contrast, the **LD** scheme is less sensitive to contrasts in dust loading (discussed in Sect. 4.4.2).

In terms of temperature difference, a shift in dust-INP efficiency is translated to an even stronger shift in dust-driven cloud glaciation. For the **NS** simulation, at $30\text{--}60^{\circ}\text{N}$, the highest fraction of cloud tops glaciate at -34°C , where about 40% glaciate. For **NS10K**, the temperature where as many (40%) liquid cloud tops glaciate is $T_{40\%} = -21^{\circ}\text{C}$, about +13 K warmer than for **NS**. Recalling Sect. 4.2.4, in the **NS10K** simulation dust leads to droplet freezing at warmer temperatures (+10 K) compared to **NS**. However, dust concentrations — and therefore droplet freezing — increase at warmer temperatures, enhancing the difference in the dust-driven cloud glaciation temperature $T_{40\%}$ between **NS** and **NS10K**.

In ECHAM-HAM, the increase in dust-driven glaciation for lower temperatures is weaker after setting a threshold for dust concentration, such that only high dust concentrations can lead to droplet freezing. At -35°C , in simulation **NS10K** the glaciated fraction converges to about 50% in both hemispheres (Fig. 4.2a–b). Using 10^6 kg^{-1} as a threshold of dust particle concentration for initiating freezing, starting at -25°C the glaciated fraction in **NS-Tuned** decreases compared to **NS10K** and remains rather constant for lower temperatures. Specifically, the glaciated fraction caps at 43% and 21% for the northern and southern mid-latitudes, respectively. The impact of the threshold in **NS-Tuned** is higher at lower temperatures and in the Southern Hemisphere, where dust concentrations tend to be lower.

4.3.2 Satellite constraints to cloud glaciation

In ECHAM-HAM, the mean state cloud ice frequency is dominated by ice formation at temperatures colder than -35°C , while the seasonal and hemispheric contrasts in cloud-top-phase are dominated by dust-driven droplet freezing between -35°C and -15°C . Fig. 4.2c–e shows the simulated frequency of ice cloud-tops *CIF* and the hemispheric and seasonal contrast in cloud-top-phase together with observations. Both the modeled and observed *CIF* increase from

0–10% to 90–100% between 0°C and –35°C (Fig. 4.2c). Between –35°C and –15°C, *CIF* is higher for the GDP than for the GOCCP observations. In the same temperature range, *CIF* varies by up to 30% between the **NoFRZ**, **NS**, **LD**, **NS-Tuned**, and **NS10K** simulations (ordered from lower to higher *CIF*). Between –35°C to 0°C, most of the ice clouds from the different simulations persist in the **NoFRZ** simulation. This implies that most of such ice clouds, especially for temperatures between –35°C and –15°C, have their origin at lower temperatures where cloud droplets can freeze without INP (Dietlicher et al., 2019). For our tuning strategy, this means that the droplet freezing parameterization alone can not explain the disagreement in the frequency of ice cloud-tops between model and observations (discussed in Sect. 4.4.4c; see also Supporting Information Fig. 4.S2a). However, the seasonal and the hemispheric contrasts are controlled by dust-driven droplet freezing. Indeed, in the model both contrasts are negligible without heterogeneous freezing (Fig. 4.2d–e; discussed in Sect. 4.4.1).

The contrast in cloud-top-phase improves compared to observations after tuning the model by choosing the NS scheme over the LD scheme, by increasing the dust-INP efficiency, and by including a dust threshold. The observed seasonal (Fig. 4.2d) and hemispheric (Fig. 4.2e) contrasts of cloud-top-phase increase between –15°C and –30°C from 0–5% up to 20–30% for the GOCCP and up to 50–60% for the GDP observations. In this temperature range, the contrasts increase with decreasing temperatures for the **NS**, **LD** and **NS-Tuned** simulations (ordered from lower to higher contrast). For temperatures colder than –15°C, **NS** results in a better agreement with the observed phase contrasts compared to **LD**, especially against the GDP observations. Furthermore, the hemispheric and seasonal contrasts are higher for the **NS-Tuned** simulation than for **NS** at all temperatures, leading to a better agreement with observations. Firstly, the higher INP efficiency in **NS10K** shifts the temperature range of the cloud-top-phase contrast to warmer temperatures. The **NS10K** simulation was selected from a wider range of simulations (N_B steps of 2.5 K) because it produces the best agreement with the observed cloud-top-phase contrasts between –15°C and –30°C (see Supporting Information 4.S3 and 4.S5). We choose this range because for temperatures warmer than –15°C, INP efficiency is too low to trigger glaciation; while for temperatures colder than –30°C, liquid clouds are too rare to derive a robust contrast in cloud-phase. Secondly, the implementation of a dust threshold in **NS-Tuned** increases the magnitude of the cloud-top-phase contrast by inhibiting droplet freezing in clean environments. We tested several thresholds, from which 10^6 kg^{-1} resulted in the best agreement with the observed cloud-top-phase contrasts, especially between –15°C and –30°C (see Supporting Information 4.S4). As a result, **NS-Tuned** agrees better with the high-contrast (GDP) reference compared to **NS** for both the seasonal and hemispheric contrasts.

4.3.3 Other climate models

Using another state-of-the-art climate model, we found that the NS scheme with enhanced dust-INP efficiency improves the cloud-phase contrast in a similar way as observed in ECHAM-HAM. To validate our constrain approach, we run several simulations including **NS** and **NS10K** with the E3SM aerosol-climate model (Rasch et al., 2019) for one year. In the E3SM model, the best agreement with the observed contrasts was found for the **NS10K** simulation (see Supporting

Simulations Latitude: 30–60°	NoFRZ °N	Δ LD °N	σ_{LD} °N	Δ LD °S	$\Delta_{NS-Tuned}$ °N	$\sigma_{NS-Tuned}$ °N	$\Delta_{NS-Tuned}$ °S
IWP, g m^{-2}	63.44	3.08	0.16	3.34	<u>6.26</u>	0.33	2.95
LWP, g m^{-2}	158.40	-30.65	0.76	-25.20	<u>-19.79</u>	0.96	-9.81
Net CRE, W m^{-2}	-34.12	1.48	0.16	1.55	<i>0.14</i>	0.13	<i>0.12</i>
CC, %	69.60	<u>-1.22</u>	0.15	<i>-0.25</i>	<u>-1.43</u>	0.22	<i>-0.23</i>
SW CRE, W m^{-2}	-56.17	3.23	0.18	2.92	<u>2.12</u>	0.19	1.11
LW CRE, W m^{-2}	22.04	-1.74	0.09	-1.37	<u>-1.98</u>	0.13	-0.98
P_{strat} , $10^{-1} \text{ mm d}^{-1}$	1.57	0.12	0.03	0.12	<u>0.24</u>	0.02	0.13
P_{cnv} , $10^{-1} \text{ mm d}^{-1}$	0.77	<i>-0.01</i>	0.02	-0.04	<u>-0.10</u>	0.02	<i>-0.01</i>
N_i , 10^8 m^{-2}	11.36	<u>-0.52</u>	0.13	-0.33	<i>-0.04</i>	0.30	<i>-0.17</i>
N_c , 10^{10} m^{-2}	8.69	<u>-1.60</u>	0.05	-0.63	<u>-1.10</u>	0.09	-0.34

Table 4.1: Changes in key microphysical parameters due to dust-INP at the mid-latitudes. Calculated as the difference of the LD and NS-Tuned simulations compared to the NoFRZ simulation. The table also highlights for which variables the change due to dust-INP is not significant (within $\pm 2\sigma$; in italics), remarkably asymmetric (at least 150% at 30–60°N relative to 30–60°S; underlined), and particularly high (at least $\pm 10\%$ relative to the average at 30–60°N; in bold). The error σ corresponds to the inter-annual (2003–2012) standard deviation of the annual-field averages at 30–60°N.

Information Fig. 4.S2).

4.3.4 Climate implications

Besides the changes in the ice cloud frequency, the dust-driven droplet freezing parameterization impacts key microphysical parameters related to radiation and precipitation. Table 4.1 summarizes these changes due to dust-INP, compared to **NoFRZ**. Although the magnitude of these changes varies, the sign of the changes is the same for both hemispheres and for all freezing parameterizations.

Dust-driven droplet freezing increases the Ice Water Path (IWP) and reduces the cloud Liquid Water Path (LWP) depending mainly on the freezing scheme used. At 30–60°N, the increase in IWP relative to **NoFRZ** (Δ IWP) is about twice as high for **NS-Tuned** compared to **LD**, which is consistent with the increase in cloud glaciation discussed in Sect. 4.3.1. Although dust-driven cloud glaciation and Δ IWP are higher for **NS-Tuned** than for **LD**, Δ LWP is lower in magnitude for **NS-Tuned** compared to **LD**, which is a rather counterintuitive result (discussed in Sect. 4.4.2). For **LD**, Δ LWP and Δ IWP are symmetric between hemispheres (the differences are below $\pm 20\%$ between 30–60°N and 30–60°S). In contrast, for **NS-Tuned** Δ LWP and Δ IWP are about twice as high at 30–60°N compared to 30–60°S.

The change in Cloud Cover (CC) due to dust-INP is similar for both simulations but highly asymmetric between hemispheres: -1.3% on average at 30–60°N and -0.2% at 30–60°S. However, Δ CC is too small to explain the large changes in shortwave (SW) CRE and longwave (LW) CRE. For **LD**, the increase in SW CRE due to dust-INP is about twice in magnitude compared to the decrease in LW CRE, suggesting a reduction of more reflective clouds (SW CRE > LW CRE), which explains the higher Net Δ CRE. In contrast, for **NS-Tuned** both Δ SW CRE and Δ LW CRE are similar in magnitude (within $\pm 15\%$), suggesting a reduction of less reflective clouds (SW CRE \sim LW CRE).

Dust-driven droplet freezing leads to a weak increase in Net CRE at the mid-latitudes. Similar to Δ LWP, the Net Δ CRE is higher for **LD** than for **NS-Tuned** (discussed in Sect. 4.4.2). However, for **NS-Tuned** Δ CRE is closer to previous estimates (0.34 W m^{-2} between 30 and

70°N; Shi & Liu, 2019). In agreement with this previous study, we find a cooling effect (of at least -0.5 W m^{-2}) for all simulations northern from 70°N related to a decrease in CC and LW CRE, because clouds there have on average a warming effect (SW CRE < LW CRE; see Supporting Information 4.S8 and 4.S11). In contrast to previous estimates, we found the dust-driven glaciation effect ΔCRE to be symmetric (within $\pm 20\%$) within hemispheres.

Due to dust-INP, stratiform precipitation P_{strat} is enhanced at the expense of convective precipitation P_{conv} . For **LD**, P_{strat} increases by about $+0.012 \text{ mm d}^{-1}$ (+8%, see also Supporting Information 4.S12). At 30–60°N, in **NS-Tuned** P_{strat} is enhanced by $+0.024 \text{ mm d}^{-1}$ (+15%), while P_{conv} decreases by -0.010 mm d^{-1} (–13%, discussed in Sect. 4.4.3).

The droplet number concentration N_c decreases due to dust-INP in agreement with the depletion in LWP. However, despite an increase in IWP the concentration of ice particles N_i decreases (discussed in Sect. 4.4.3).

In **NS-Tuned**, the magnitude of the cloud microphysical changes is dominated by the increase in dust-INP efficiency, while the large hemispheric asymmetry is due to the implementation of the dust threshold for droplet freezing. For the cloud water path, cloud cover, cloud radiative effects, and droplet concentration, the changes in both hemispheres are two to three times higher in **NS10K** compared to **NS** (See Supporting Information, Table 4.S2). For **NS-Tuned**, the changes due to dust-INP at 30–60°N are slightly lower (by –10% or less in magnitude) compared to **NS10K**. In contrast, at 30–60°S the changes for **NS-Tuned** are significantly lower (by –30% or more) compared to **NS10K** (see also Supporting Information 4.S13).

4.4 Discussion

4.4.1 Dust-INP and meteorology

Our simulations suggest that meteorology plays rather a minor role on cloud-phase variability. The results presented in Sect. 4.3.2 suggests that the hemispheric and seasonal changes in meteorology (including wind, humidity, and temperature) do not affect the downward transport of ice clouds formed at temperatures colder than -35°C (without INP). In other words, the cloud-top-phase contrasts are controlled by the variability of cloud glaciation at temperatures warmer than -35°C (with INP). Furthermore, if dust-INP concentrations are held constant, the cloud-phase contrasts vanish as well (see Supporting Information 4.S7), suggesting that cloud glaciation at temperatures warmer than -35°C is controlled by dust-INP rather than by meteorology.

4.4.2 Liquid water depletion and dust-driven glaciation in the LD scheme

The stronger decrease in LWP in **LD** compared to **NS** is closely related to the variability of CCN. To explain the strong decrease in LWP due to dust-driven cloud glaciation in **LD**, we studied the effect of TKE and CCN on droplet freezing. In the LD scheme, both a higher TKE or a lower CCN leads to higher droplet freezing (see Eq. 4.1 and 4.2). Sensitivity tests showed that the variability in TKE only plays a minor role on LWP. However, setting CCN to

a constant — so that the cloud-top ice frequency is similar to the default **LD** simulation — results in a weaker LWP reduction and weaker CRE increase due to dust-INP (see Supporting Information 4.S6 and 4.S10). This suggests that the CCN variability is responsible for the higher LWP depletion and higher CRE in **LD**, perhaps due to an unrealistic enhancement in droplet freezing during conditions of low CCN.

In addition, the lower hemispheric contrast in cloud-phase for **LD** compared to **NS** is unrelated to TKE and CCN and probably related to the prognostic formulation (time-dependent) of the LD scheme. Other than for **NS**, the number of frozen droplets in **LD** can keep increasing with time as dust-INP are not depleted in the model after freezing (see Sect. 4.2.3).

4.4.3 Droplet freezing and precipitation

The high increase in P_{strat} at the expense of P_{conv} in **NS-Tuned** may be associated to the timing of droplet freezing events. If low INP concentrations are allowed to freeze droplets, the downward transport of ice particles may be too low for the hydrometeors to reach the surface without evaporating along the way, but will still deplete the water content of the cloud. In contrast, if low INP concentrations are not allowed to trigger freezing, more liquid content will be available for future droplet freezing events, which would lead more frequently to precipitation. This may also result in a lower water vapor content below the cloud at low dust conditions. Thus, during convection drier air would be entrained, which could explain the inhibition of P_{conv} . Alternatively, droplet freezing could change the temperature gradient, leading to a more stable atmosphere, suppressing convection.

The slight decrease in N_i due to dust-INP may be related to a lower number of droplets available for freezing at temperatures colder than -35°C , because they already freeze earlier at warmer temperatures. For temperatures warmer than -35°C , ice particles will grow by depleting existing cloud droplets. Therefore, despite an increase in IWP, heterogeneous freezing may cause N_i to decrease as fewer cloud droplets reach temperatures colder than -35°C .

4.4.4 A misrepresented ice process?

As found with ECHAM-HAM and confirmed with the E3SM model, a higher INP efficiency (**NS10K** compared to **NS**) leads to a better agreement between the cloud-phase contrasts and observations. Along the pathway between dust emission and cloud glaciation, several reasons could explain this behavior:

a) INP load

The ECHAM-HAM has shown a good agreement with both ground-based and spaceborne observations of dust loading (Koffi et al., 2016; Tegen et al., 2019; Shi & Liu, 2019). Although biases in dust loading or size distribution may affect droplet freezing (Adebiyi & Kok, 2020; Shi & Liu, 2019), we consider it unlikely that such biases would account for more than an order of magnitude in INP concentrations.

b) INP-to-Ice

Very efficient dust-INP like K-feldspar can freeze at temperatures about $+7.5\text{K}$ warmer compared to common dust-INP like montmorillonite (see Supporting Information Fig. 4.S1). However, the assumption of montmorillonite as unique dust-INP is based on well-researched

soil mineralogical composition (Hoose et al., 2008; Claquin et al., 1999). Therefore, including additional dust mineral types (e.g, K-feldspar) in the simulation of INP concentrations would only lead to a weak improvement, because such efficient dust-INP are relatively rare. Alternatively, secondary ice production (Field et al., 2017; Lauber et al., 2018) could result in more ice particles per INP than expected. There are additional processes, such as INP pre-activation (Wagner et al., 2016) or INP-recycling (Solomon et al., 2015), which could also lead to an increased number of frozen droplets. In addition, dust aerosol could include other substances such as biogenic material, which could enhance its ice-nucleating efficiency (Augustin-Bauditz et al., 2016; O’Sullivan et al., 2014, 2016).

c) Ice-to-Cloud Glaciation

There could be a misrepresentation in the processes linking the ice number concentration with the glaciation of a mixed-phase cloud. For example, if the WBF process is underestimated, a higher droplet freezing will be needed in the model for clouds to glaciate. Additionally, collision and transport processes, such as ice-ice aggregation, riming, ice fragmenting and ice sedimentation also affect the number and size of ice particles in the cloud and how fast the cloud will glaciate (Korolev et al., 2017). However, these processes are parameterized differently in ECHAM-HAM and E3SM but both models lead to similar cloud-phase contrasts, suggesting that the model formulation of such processes could play a minor role.

d) INP tracking

In addition to a higher INP efficiency, setting a dust concentration threshold for droplet freezing in **NS-Tuned** inhibited much of the cloud glaciation in clean conditions such as in the southern mid-latitudes, leading to more realistic cloud-phase contrasts. This suggests that — at least during low dust concentrations — INP concentrations may be overestimated due to the lack of INP depletion in climate models.

4.5 Conclusions

We showed that dust-driven droplet freezing can be constrained in climate models using satellite observations of regional and seasonal contrasts in cloud ice frequency. We consider this an improvement from previous tuning strategies where only mean atmospheric state quantities like cloud ice frequency or dust-INP concentrations are constrained.

Observations of cloud-phase contrast may provide a constraint for the effect of dust-INP on radiation and precipitation. With the NS-Tuned simulation, which is constrained by observations, the simulated radiative effect of cloud glaciation is much lower ($+0.14 \pm 0.13 \text{ W m}^{-2}$) than for the default LD scheme ($+1.48 \pm 0.16 \text{ W m}^{-2}$) at 30–60°N. These new constraints on the impact of dust-INP on climate may help to better understand climate change under varying aerosol loadings and direct modeling efforts in the right direction.

4.S Supporting Information for "Hemispheric and seasonal contrast of cloud phase from the A-Train"

Supporting Information for "Can observations of cloud-phase constrain the impact of dust-driven droplet freezing on climate?"

This supporting information includes mainly the results for simulations that were omitted in the main article but may offer important information to understand the sensitivity of the freezing schemes to different parameters.

Text 4.S1. Additional acknowledgements: BG acknowledges support by the Swiss National Science Foundation project P400P2_191112 and by the National Science Foundation under Grant AGS-1549579. This project has received funding from the European Union's Horizon 2020 research and innovation programme under grant agreement No 821205. This research was partially supported as part of the Energy Exascale Earth System Model (E3SM) project, funded by the U.S. Department of Energy, Office of Science, Office of Biological and Environmental Research.

The ECHAM-HAMMOZ model is developed by a consortium composed of ETH Zurich, Max Planck Institut für Meteorologie, Forschungszentrum Jülich, University of Oxford, the Finnish Meteorological Institute, and the Leibniz Institute for Tropospheric Research and managed by the Center for Climate Systems Modeling (C2SM) at ETH Zurich.

Text 4.S2. Additional details on ECHAM-HAM: For the simulations, vorticity, divergence, and surface pressure were nudged using the ERA-Interim reanalysis (see also Supporting Information 4.S8 and 4.S9). Sea surface temperature and sea ice cover were taken from observations. The P3 scheme avoids additional categories for ice hydrometeors and conversion processes between these categories, improving the representation of ice formation pathways.


Text 4.S3. E3SM model description: Exascale Earth System Model (E3SM) is a general circulation model developed by the US Department of Energy (J. Golaz et al., 2019). The model uses a spectral finite element dynamical core and is used at ne30 horizontal resolution (about 1°), in combination with 72 vertical levels. The atmospheric component of E3SM was branched from the CAM5 model (Neale et al., 2004), but has evolved since by adding new ways of coding and new physical parameterizations related to clouds and aerosols (Xie et al., 2018; Rasch et al., 2019). E3SM includes an updated cloud microphysical scheme (Gettelman & Morrison, 2015), a four-mode version of the aerosol model (Liu et al., 2016), and Cloud Layers Unified by Binormals parameterization (J.-C. Golaz et al., 2002; Larson & Golaz, 2005) that replaces the separate shallow convection, turbulent transport, and cloud macrophysics schemes.

Simulation name	Freezing scheme	Comments	
NoFRZ LD	Off LD	No heterogeneous freezing Default (montmorillonite)	
lowAer avgAer	LD LD	$CCN=10^6 \text{ kg}^{-1}$ $CCN=10^7 \text{ kg}^{-1}$	
lowTKE avgTKE	LD LD	$CCN=10^7 \text{ kg}^{-1}, \sqrt{TKE} = 5 \cdot 10^{-2} \text{ kg}^{-1}$ $CCN=10^7 \text{ kg}^{-1}, \sqrt{TKE} = 5 \cdot 10^{-1} \text{ kg}^{-1}$	
conINP_100%	LD	$\frac{N_{imm,dust}}{CCN} = 100\%$	
conINP_10%	LD	$\frac{N_{imm,dust}}{CCN} = 10\%$	
conINP_1%	LD	$\frac{N_{imm,dust}}{CCN} = 1\%$	
CNT	CNT	"Natural" dust (E3SM only)	
			$N_B [K]$
NS	NS	montmorillonite ($N_A = 1 \text{ K}^{-1}$)	-5
NS2.5K	NS		-2.5
NS5K	NS		0
NS7.5K	NS		+2.5
NS10K	NS		+5
NS-Tuned	NS	N_{dust} threshold (10^6 kg^{-1})	+5
Dust > 1e5	NS	N_{dust} threshold (10^5 kg^{-1})	+5
Dust > 1e6	NS	N_{dust} threshold (10^6 kg^{-1})	+5
Dust > 1e7	NS	N_{dust} threshold (10^7 kg^{-1})	+5

Table 4.S1: Simulations with the ECHAM-HAM model included in the Supporting Information. N_B corresponds to the temperature offset for immersion freezing, with higher offsets corresponding to more efficient INP.

Sim	NoFRZ 30–60°N	Δ NS10K 30–60°N	σ	Δ NS10K 30–60°S	Δ NS 30–60°N	σ	Δ NS 30–60°S
IWP, g m^{-2}	63.44	6.57	0.34	4.47	<u>1.29</u>	0.20	0.65
LWP, g m^{-2}	158.40	-22.39	0.86	-15.33	<u>-7.07</u>	1.16	-4.41
Net CRE, W m^{-2}	-34.12	<u>0.15</u>	0.12	-0.06	<u>-0.28</u>	0.08	-0.03
CC, %	69.60	<u>-1.68</u>	0.15	-0.32	<u>-0.17</u>	0.14	-0.10
SW CRE, W m^{-2}	-56.17	2.48	0.19	1.71	0.73	0.20	0.49
LW CRE, W m^{-2}	22.04	-2.32	0.15	-1.77	<u>-1.01</u>	0.13	-0.52
P_{strat} , $10^{-1} \text{ mm d}^{-1}$	1.57	<u>0.02</u>	0.01	0.02	<u>0.01</u>	0.01	0.01
P_{cnv} , $10^{-1} \text{ mm d}^{-1}$	0.77	-0.01	0.01	-0.01	-0.01	0.01	-0.01
N_i , 10^8 m^{-2}	11.36	-0.14	0.31	-0.30	<u>-0.41</u>	0.30	-0.18
N_c , 10^{10} m^{-2}	8.69	<u>-1.33</u>	0.08	-0.57	<u>-0.43</u>	0.08	-0.17

Table 4.S2: Table containing the changes of key variables relative to the NoFRZ simulation. The table also highlights for which variables the change due to dust-INP is significant (within $\pm 2\sigma$; in italics), remarkably asymmetric (least 150% at 30–60°N relative to 30–60°S; underlined), and particularly high (at least $\pm 10\%$ relative to the average at 30–60°N; in bold). The σ corresponds to the inter-annual (2003-2012) standard deviation of the field average at 30–60°N.



../papers/fig.paper3.si/AB-eps-converted-to.pdf

Figure 4.S1: Ice Nucleating Active Site (INAS) concentration for the different simulations. The slope and offset for montmorillonite ($N_A = 0.914 K^{-1}$ and $N_B = -2.706 K^{-1}$) and K-feldspar ($N_A = 1.026 K^{-1}$ and $N_B = 2.003 K^{-1}$) are taken from Ickes et al. (2017).

```
../papers/fig.paper3.si/ecsm.mean.png
```

```
../papers/fig.paper3.si/ecsm.MAM.png
```

```
../papers/fig.paper3.si/ecsm.contrast.png
```

Figure 4.S2: Same as Fig. 4.2c-e, but for the E3SM model. Analog to groups I and II in Fig. 1, but for the E3SM model.

```
../papers/fig.paper3.si/eff.mean.png
```

```
../papers/fig.paper3.si/eff.MAM.png
```

```
../papers/fig.paper3.si/eff.contrast.png
```

Figure 4.S3: Sensitivity study of dust INP efficiency for droplet freezing with the ECHAM-HAM showing all simulations considered for group II (Fig. 4.1).

../papers/fig.paper3.si/thresh.mean.png

../papers/fig.paper3.si/thresh.MAM.png

../papers/fig.paper3.si/thresh.contrast.png

Figure 4.S4: Sensitivity study of dust thresholds for droplet freezing with the ECHAM-HAM showing all simulations from group III (Fig. 4.1).

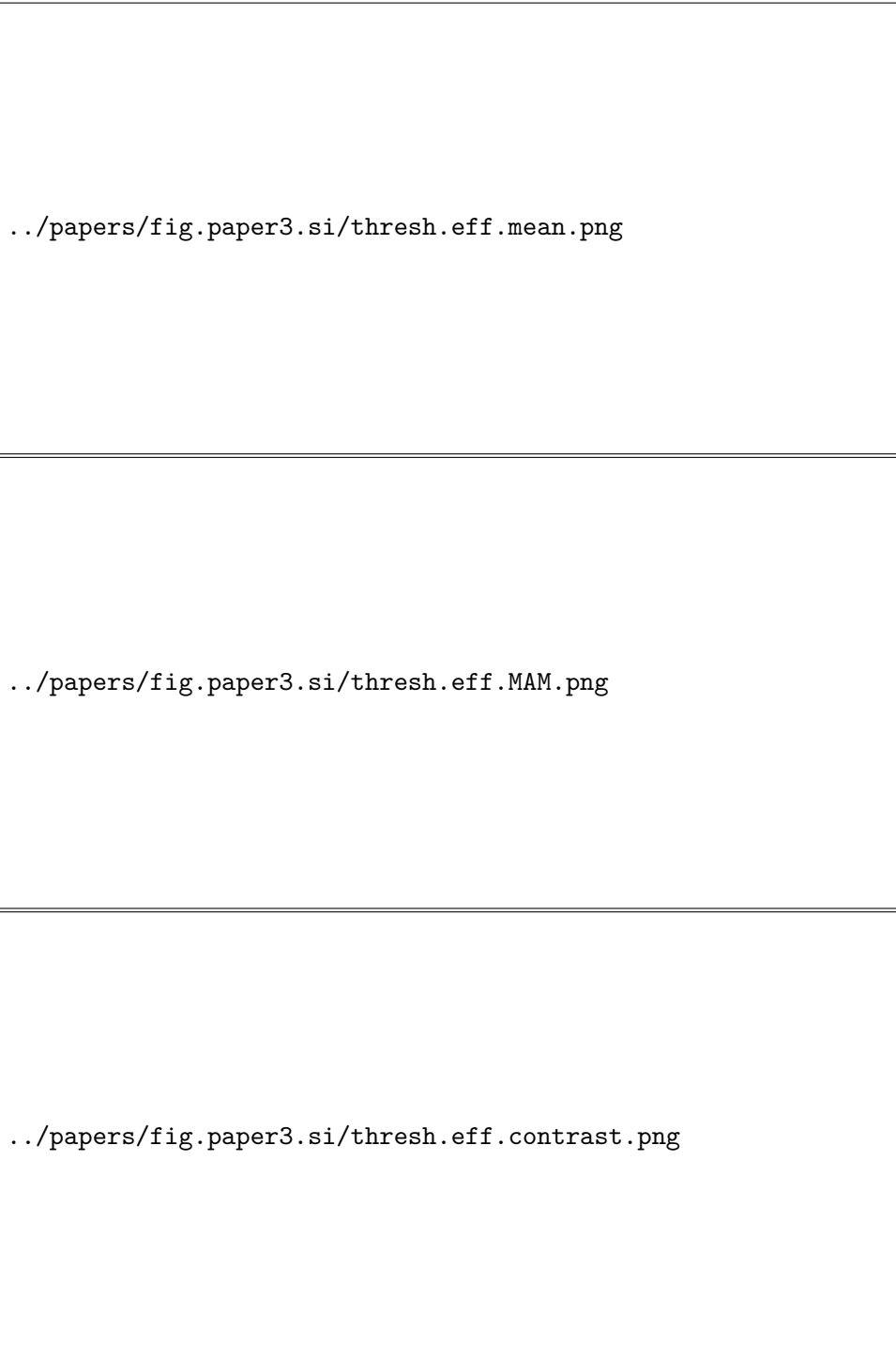


Figure 4.S5: Sensitivity study of dust INP efficiency for droplet freezing with the ECHAM-HAM with a dust threshold of 10^{-6} kg^{-1} . This shows the effect of switching the order of groups II and III (Fig. 4.1) in the tuning strategy by first setting the dust threshold and then finding the appropriate efficiency for dust INP.

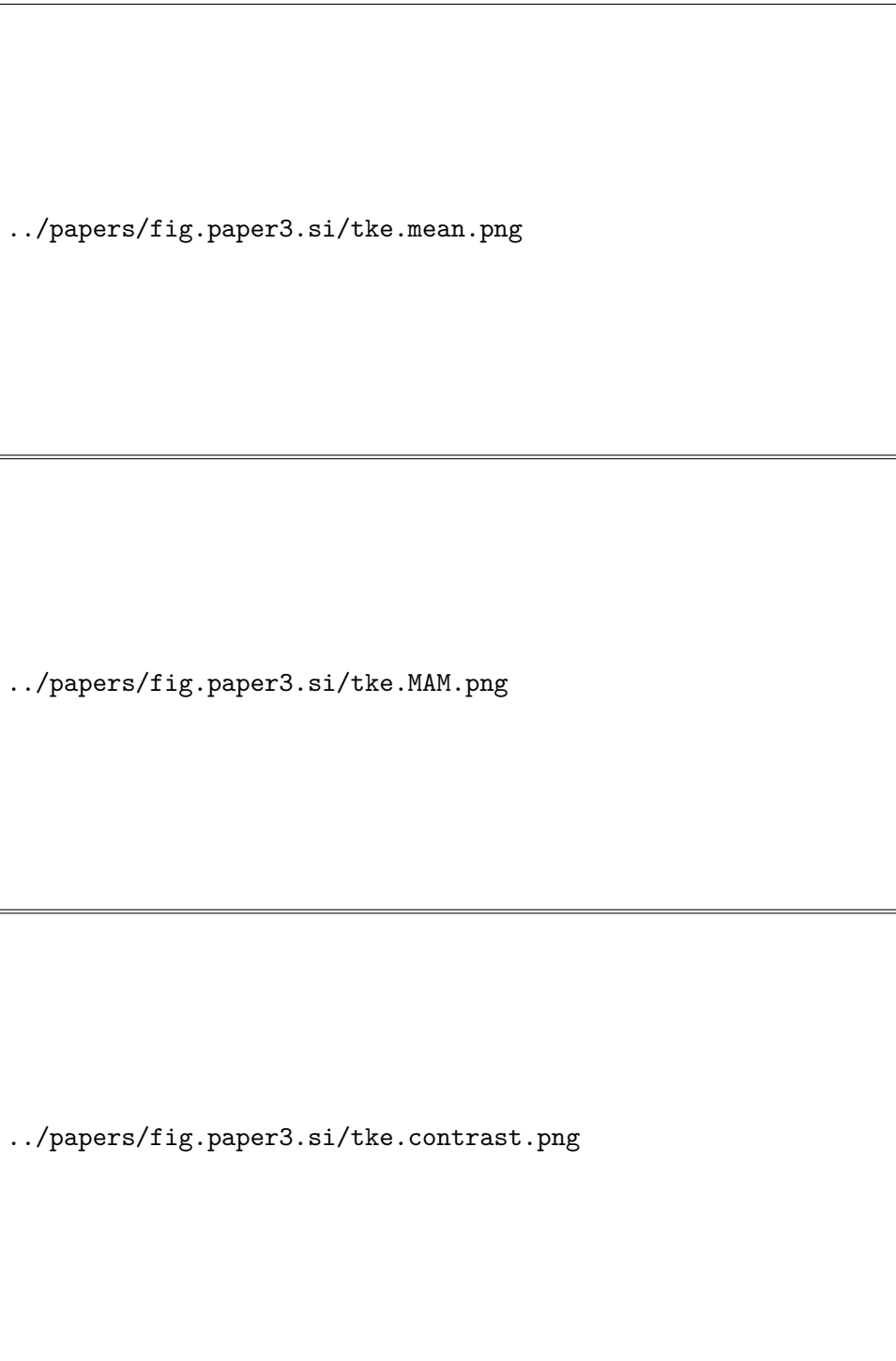


Figure 4.S6: Sensitivity study of the LD scheme using constant CCN and constant TKE values (See Table 4.S1).

../papers/fig.paper3.si/conINP.mean.png

../papers/fig.paper3.si/conINP.MAM.png

../papers/fig.paper3.si/conINP.contrast.png

Figure 4.S7: Sensitivity study of the LD scheme using constant aerosol values for $\frac{N_{imm,dust}}{CCN}$ (See Table 4.S1).

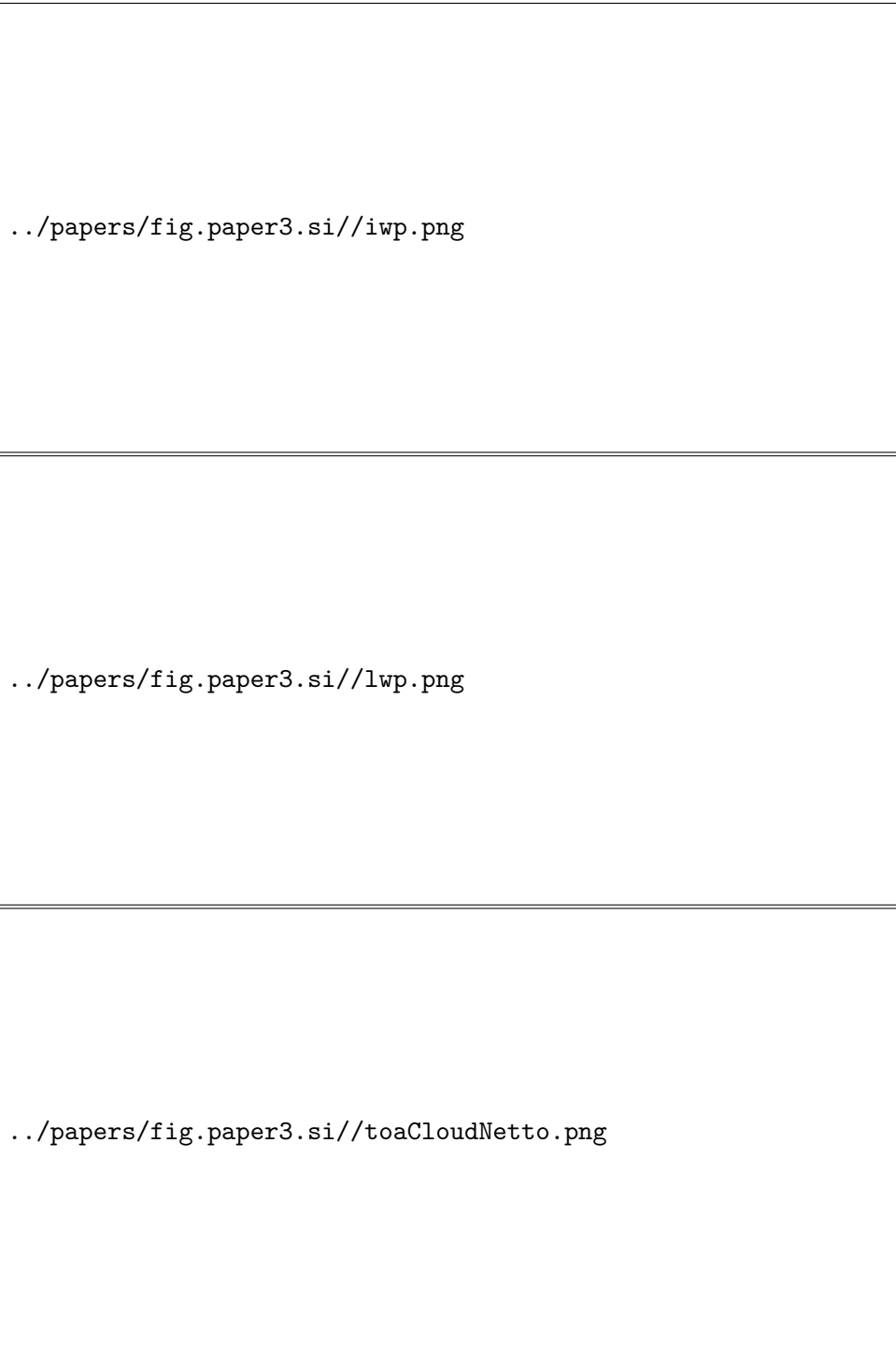


Figure 4.S8: Dust-driven change in: (a) Ice Water Path (IWP) (b) Liquid Water Path (LWP) (c) Cloud Forcing at the Top Of the Atmosphere (TOA; positive values associated to warming). For the runs of the main study (Fig. 4.1). Nudged simulations for 2003-2012.

../papers/fig.paper3.si/iwp.free.png

../papers/fig.paper3.si/lwp.free.png

../papers/fig.paper3.si/toaCloudNetto.free.png

Figure 4.S9: Same as Fig. 4.S8 but for the free-runs (not nudged) simulations for 2003-2012.

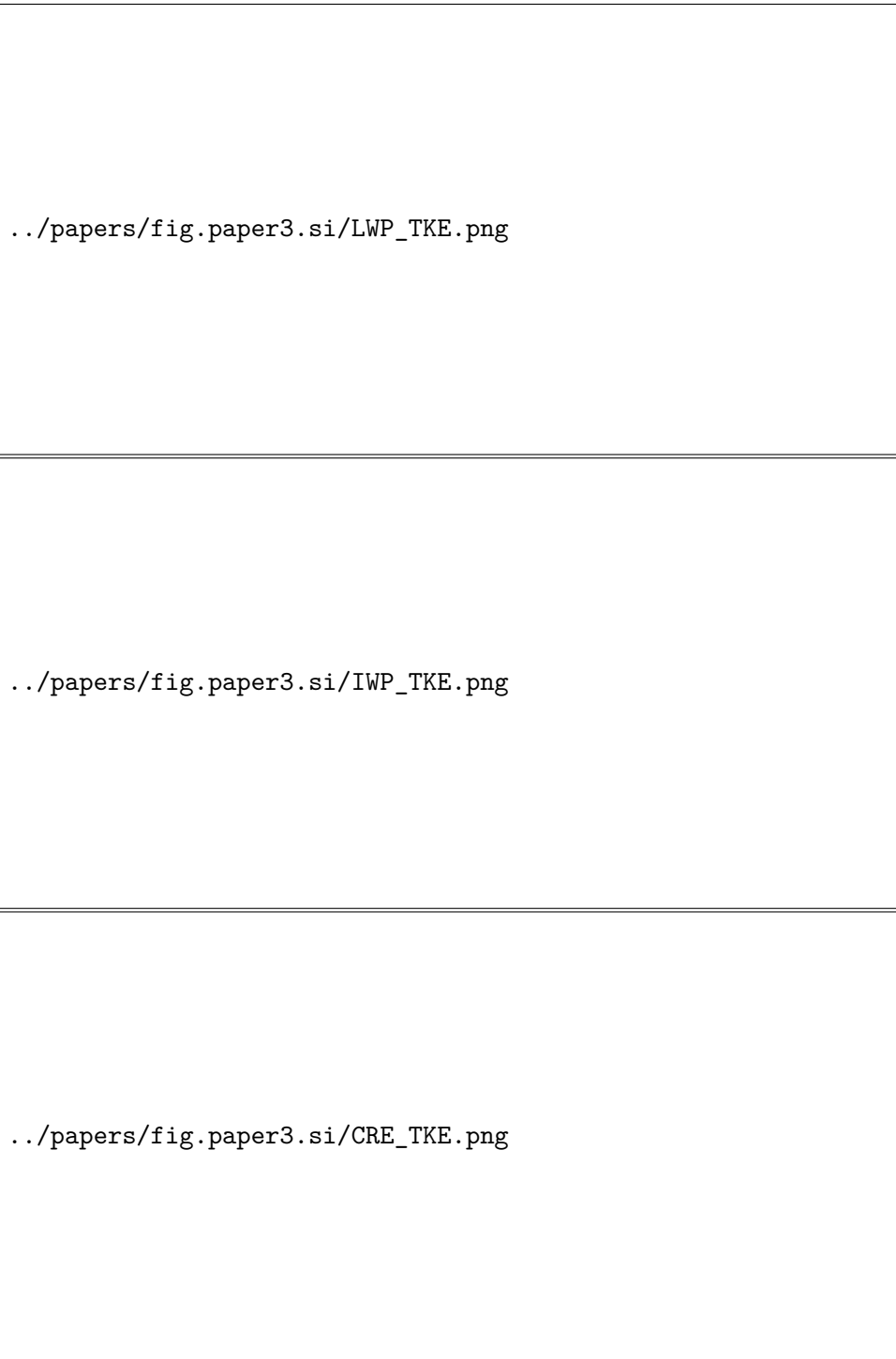


Figure 4.S10: Same as Fig. 4.S8 but for the runs using the LD scheme with TKE and *CCN* set constant (see Table 4.S1). Free-run simulations for 2003-2012.

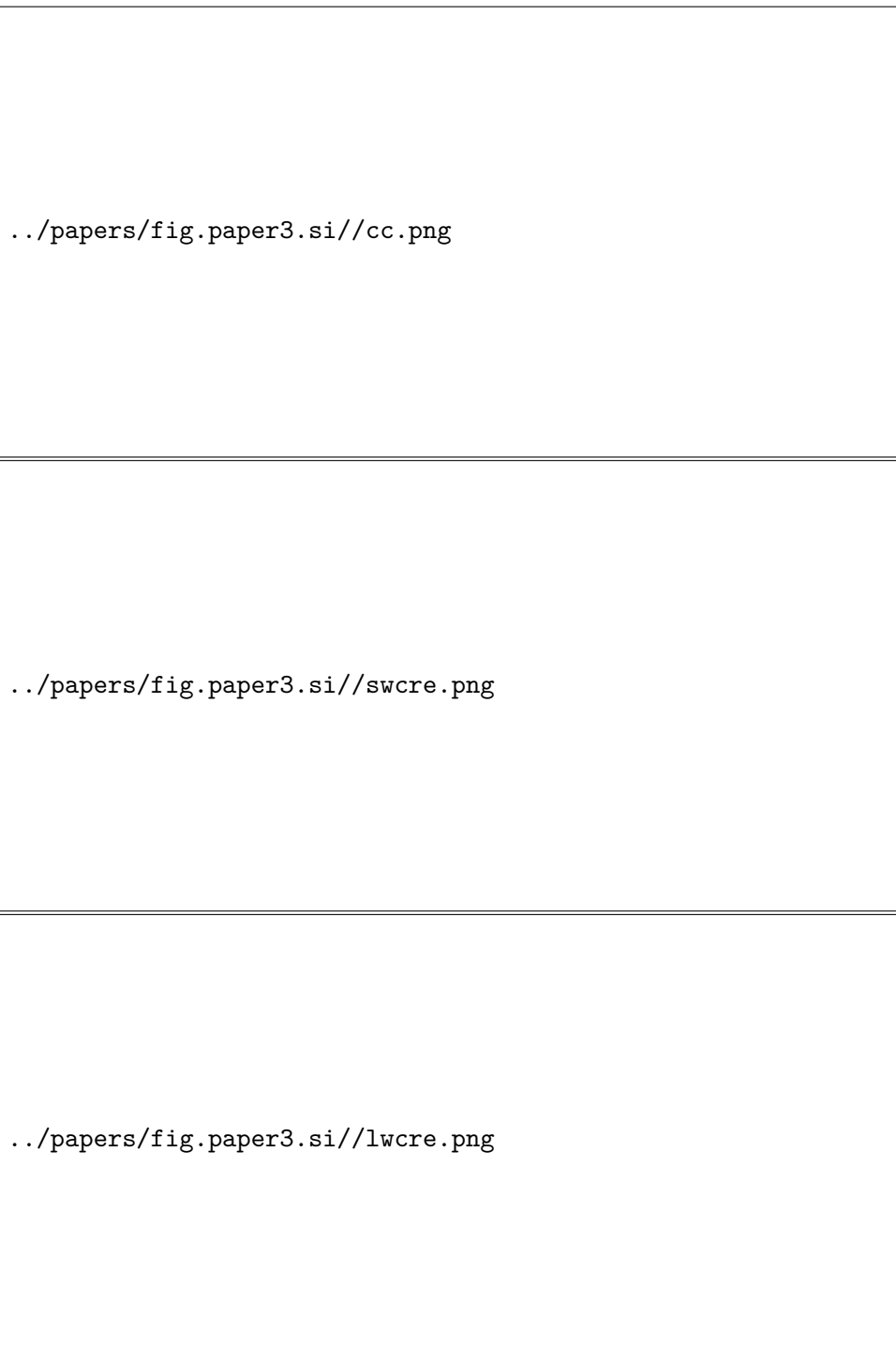


Figure 4.S11: Dust-driven change in: (a) Cloud Cover (b) Shortwave Cloud Radiative Effect (c) Longwave Cloud Radiative Effect For the runs of the main study (Fig. 4.1). Nudged simulations for 2003-2012. Calculated as the difference relative to the NoFRZ simulation.



Figure 4.S12: Dust-driven change in: (a) Stratiform Precipitation (b) Convective Precipitation For the runs of the main study (Fig. 4.1). Nudged simulations for 2003-2012. Calculated as the difference relative to the NoFRZ simulation.



Figure 4.S13: Dust-driven change in: (a) Ice number concentration (b) Droplet number concentration For the runs of the main study (Fig. 4.1). Nudged simulations for 2003-2012. Calculated as the difference relative to the NoFRZ simulation.

Conclusion

Do dust aerosols control the global variability of cloud-phase?

The north-south contrast in ice frequency can be explained by the higher average dust loading in the Northern Hemisphere. After constraining the influence of humidity and atmospheric stability, we observed an increase in the frequency of ice clouds for higher dust concentrations in both hemispheres. This correlation suggests that the higher ice cloud frequency in the Northern Hemisphere can be explained by its higher average dust loading.

For conditions with similar dust loadings at opposite latitudes, the differences in ice frequency may be explained by differences in ice-nuclei efficiency. For similar mixing-ratios of mineral dust, we found that the ice frequency can still vary between latitudes, especially between hemispheres and between mid- and high-latitudes. This variability could be explained by differences in the mineralogical composition of the dust aerosol at both hemispheres. For example, feldspar minerals are likely more relevant at temperatures higher than -20°C , where the immersion efficiency of clay minerals quickly decay. Thus, we speculate that the higher cloud ice occurrence-frequency in the Southern Hemisphere at -15°C for similar dust loadings may result from a higher fraction (or higher efficiency) of feldspar minerals. Furthermore, depletion or ageing of highly efficient dust ice-nuclei during its transport may also explain the higher ice occurrence-frequency at the mid-latitudes compared to the high-latitudes for similar mixing-ratios of mineral dust, especially at temperatures higher than -20°C .

The variability of the cloud-phase contrasts with temperature suggests that dust ice-nuclei may be controlling the global variability of cloud-phase. Both the hemispheric and seasonal contrasts in cloud-phase are higher at regions where the contrast in dust loading is higher. Moreover, the cloud-phase contrasts tend to increase at lower temperatures. This increase of cloud-phase contrast at lower temperatures coincides with the expected increase in dust ice-nuclei effectivity with temperature. In addition, the observed cloud-phase contrast between spring and fall in the Northern Hemisphere is unlikely to be explained by the seasonal variability of confounding meteorological factors, increasing the confidence in dust aerosol as the driver of cloud-phase variability.

A new reference for cloud-top thermodynamic phase

We use a satellite cloud product ensemble to assess the variability of cloud-phase with higher confidence and to study how individual products may be biased. By using only retrievals where

satellite products agree on cloud-phase, we find that the cloud-phase transition occurs within a narrower temperature range. This suggests that individual products tend to classify too many clouds as liquid for temperatures lower than -30°C and too many as ice for temperatures higher than -10°C .

Can we estimate the effect of dust-driven glaciation on climate?

To achieve a more realistic dust-driven glaciation on a climate model, we tune the dust ice-nuclei efficiency and limit their effect during clean conditions. We find that a higher dust ice-nuclei efficiency leads to a better agreement between simulated cloud-phase contrasts and observations. Along the pathway between dust emission and cloud glaciation, several reasons could explain this behavior. For example, secondary ice production could result in more ice particles per ice-nuclei than expected. There are other processes, such as ice-nuclei pre-activation or ice-nuclei recycling, which could also lead to an increased number of frozen droplets. In addition, dust aerosol could include other substances such as biogenic material, which could enhance its ice-nucleating efficiency. Besides a higher ice-nuclei efficiency, setting a dust concentration threshold for droplet freezing in the new model configuration inhibited much of the cloud glaciation in clean conditions such as in the southern mid-latitudes, leading to more realistic cloud-phase contrasts. This suggests that — at least during low dust concentrations — ice-nuclei concentrations may be overestimated due to the lack of ice-nuclei depletion in climate models.

Using the tuned configuration of our climate model, we could estimate the effects of dust ice-nuclei on climate at the mid-latitudes. Dust-driven droplet freezing increases the cloud ice water path and reduces the cloud liquid water path, leading to an increase in the cloud radiative effect. Droplet number concentration decreases in agreement with the depletion in liquid water path due to dust ice-nuclei. Dust ice-nuclei also lead to a weak increase in the warming effect of clouds and a decrease in cloud cover. After tuning, the model agrees better with the estimated cloud-top-phase contrasts and results in a dust-driven glaciation effect of $0.14 \pm 0.13 \text{ W m}^{-2}$ in the Northern Hemisphere, which is lower than previously thought. In addition, stratiform precipitation is enhanced at the expense of convective precipitation due to dust ice-nuclei. In the new configuration of the freezing scheme, the magnitude of these cloud microphysical changes is dominated by the increase in dust ice-nuclei efficiency, while the hemispheric asymmetry of these changes is a result of the droplet freezing limitation for clean conditions.

Outlook

Meteorological and aerosol contribution to cloud-phase variability.

It was shown that humidity and static stability cannot alone explain the correlation between dust loading and cloud-phase. However, other factors that covary with dust loading and cloud-phase could still be interfering. Atmospheric conditions associated with the emission and transport of mineral dust may be correlated with cloud-phase. For example, dusty air masses from land are usually warmer and drier compared to oceanic air masses. Although not discussed in this thesis, there is a contrast in cloud-phase between summer and winter conditions which may be explained by the meteorological differences between seasons. By studying this contrast, it may be possible to better understand how meteorology affects the cloud-phase and how to better separate the meteorological with the aerosol contributions to cloud-phase variability.

More than dust: Black carbon and marine organic ice-nuclei.

In order to assess the influence of aerosols on cloud-phase, a strong and extended perturbation of aerosol loading is needed. Otherwise, the effect of aerosols may be masked by other background aerosols or meteorology. Thus, in this dissertation, we use the natural seasonal and hemispheric perturbations in atmospheric dust-loading as a natural laboratory. To study other types of aerosols, we must assess similar strong perturbations of aerosol loading. For marine organic aerosol, the regional and seasonal variability associated with the biological productivity in the ocean could be also exploited. For anthropogenic aerosol, finding strong perturbations may be challenging. However, extreme emission events such as wildfires could be used to study the effect of black carbon and extrapolate its behavior to anthropogenic combustion aerosols.

Improving the representation of dust-driven cloud glaciation in climate models.

It was speculated in Chapter 2 that the differences in ice frequency at opposite latitudes for similar dust loadings could be explained by regionally different dust ice-nuclei efficiencies. This hypothesis could be tested with a climate model by assuming different dust ice-nuclei efficiencies for different regions while including accurate tracking and depletion of ice-nuclei. Such tracking of ice-nuclei is crucial for the representation of droplet freezing during clean conditions at low temperatures. Furthermore, ice processes that may enhance droplet freezing, such as ice multiplication, ice-nuclei pre-activation, and ice-nuclei recycling should also be implemented in the climate model to assess their impact on dust-driven cloud glaciation. In addition, the

mean-state ice frequency in ECHAM-HAM is strongly biased for warmer temperatures compared to satellite observations and compared to other state-of-the-art models like E3SM. Tuning parameters like ice-ice aggregation strongly affect this bias but also control the cloud radiative effect. Thus, a new tuning strategy for ice processes is needed. Such a tuning strategy should aim at achieving both a realistic cloud radiative effect and an accurate mean-state ice frequency.

Climate sensitivity, cirrus regime, and geoengineering potential.

The cloud-phase feedback has been identified as one of the main sources of uncertainty for the projections of global warming. We could extend our simulations to study the effect of dust-driven glaciation on the cloud phase feedback to a warmer climate and its contribution to the climate sensitivity. We could also extend the analysis and modelling strategy to study the variability in ice number concentration and cloud fraction in the cirrus regime (below -35°C) and its relation to different ice-nuclei. In addition, the impact of cloud seeding from cirrus into the mixed-phase regime could also be evaluated. Finally, besides aiming for an accurate prediction of global warming, a better understanding of aerosol-driven droplet freezing may improve our knowledge on the potential climate impacts of anthropogenic aerosols and, eventually, evaluate the effect of potential geoengineered ice-nuclei injections seeking to mitigate global warming.

References

- Adebiyi, A. A., & Kok, J. F. (2020). Climate models miss most of the coarse dust in the atmosphere. *Science Advances*, *6*(15). doi: 10.1126/sciadv.aaz9507
- Albani, S., Mahowald, N. M., Delmonte, B., Maggi, V., & Winckler, G. (2012). Comparing modeled and observed changes in mineral dust transport and deposition to Antarctica between the Last Glacial Maximum and current climates. *Climate Dynamics*, *38*(9-10), 1731–1755. doi: 10.1007/s00382-011-1139-5
- Albrecht, B. A. (1989). Aerosols, cloud microphysics, and fractional cloudiness. *Science*, *245*(4923), 1227–1230. doi: 10.1126/science.245.4923.1227
- Ansmann, A., Rittmeister, F., Engelmann, R., Basart, S., Jorba, O., Spyrou, C., ... Kanitz, T. (2017). Profiling of Saharan dust from the Caribbean to western Africa - Part 2: Shipborne lidar measurements versus forecasts. *Atmospheric Chemistry and Physics*. doi: 10.5194/acp-17-14987-2017
- Ansmann, A., Tesche, M., Althausen, D., Müller, D., Seifert, P., Freudenthaler, V., ... Dubovik, O. (2008). Influence of Saharan dust on cloud glaciation in southern Morocco during the Saharan Mineral Dust Experiment. *Journal of Geophysical Research Atmospheres*. doi: 10.1029/2007JD008785
- Atkinson, J. D., Murray, B. J., Woodhouse, M. T., Whale, T. F., Baustian, K. J., Carslaw, K. S., ... Malkin, T. L. (2013). The importance of feldspar for ice nucleation by mineral dust in mixed-phase clouds. *Nature*, *498*(7454), 355–358. doi: 10.1038/nature12278
- Augustin-Bauditz, S., Wex, H., Denjean, C., Hartmann, S., Schneider, J., Schmidt, S., ... Stratmann, F. (2016). Laboratory-generated mixtures of mineral dust particles with biological substances: Characterization of the particle mixing state and immersion freezing behavior. *Atmospheric Chemistry and Physics*. doi: 10.5194/acp-16-5531-2016
- Avery, M. A., Ryan, R. A., Getzewich, B. J., Vaughan, M. A., Winker, D. M., Hu, Y., ... Verhappen, C. A. (2020). Caliop v4 cloud thermodynamic phase assignment and the impact of near-nadir viewing angles. *Atmospheric Measurement Techniques*, *13*(8), 4539–4563. doi: 10.5194/amt-13-4539-2020
- Barahona, D., Molod, A., & Kalesse, H. (2017). Direct estimation of the global distribution of vertical velocity within cirrus clouds. *Scientific Reports*. doi: 10.1038/s41598-017-07038-6
- Bellouin, N., Quaas, J., Gryspeerdt, E., Kinne, S., Stier, P., Watson-Parris, D., ... Stevens, B. (2020). Bounding global aerosol radiative forcing of climate change. *Reviews of Geophysics*, *58*(1), e2019RG000660. doi: 10.1029/2019RG000660
- Bergeron, T. (1935). On the physics of cloud and precipitation. *Proceedings of the Fifth Assembly of the International Union of Geodesy and Geophysics*, *2*, 156–178.

- Bodas-Salcedo, A., Mulcahy, J. P., Andrews, T., Williams, K. D., Ringer, M. A., Field, P. R., & Elsaesser, G. S. (2019). Strong dependence of atmospheric feedbacks on mixed-phase microphysics and aerosol-cloud interactions in hadgem3. *Journal of Advances in Modeling Earth Systems*, *11*(6), 1735-1758. doi: 10.1029/2019MS001688
- Bodas-Salcedo, A., Webb, M. J., Bony, S., Chepfer, H., Dufresne, J.-L., Klein, S. A., ... John, V. O. (2011). Cosp: Satellite simulation software for model assessment. *Bulletin of the American Meteorological Society*, *92*(8), 1023-1043. doi: 10.1175/2011BAMS2856.1
- Bodas-Salcedo, A., Williams, K. D., Ringer, M. A., Beau, I., Cole, J. N. S., Dufresne, J.-L., ... Yokohata, T. (2014). Origins of the Solar Radiation Biases over the Southern Ocean in CFMIP2 Models*. *Journal of Climate*, *27*(1), 41-56. doi: 10.1175/JCLI-D-13-00169.1
- Boose, Y., Welti, A., Atkinson, J., Ramelli, F., Danielczok, A., Bingemer, H. G., ... Lohmann, U. (2016). Heterogeneous ice nucleation on dust particles sourced from nine deserts worldwide - Part 1: Immersion freezing. *Atmospheric Chemistry and Physics*, *16*(23), 15075-15095. doi: 10.5194/acp-16-15075-2016
- Bosilovich, M. G., Robertson, F. R., & Chen, J. (2011). Global energy and water budgets in MERRA. *Journal of Climate*. doi: 10.1175/2011JCLI4175.1
- Broadley, S. L., Murray, B. J., Herbert, R. J., Atkinson, J. D., Dobbie, S., Malkin, T. L., ... Neve, L. (2012). Immersion mode heterogeneous ice nucleation by an illite rich powder representative of atmospheric mineral dust. *Atmospheric Chemistry and Physics*. doi: 10.5194/acp-12-287-2012
- Bruno, O., Hoose, C., Storelvmo, T., Coopman, Q., & Stengel, M. (2021). Exploring the cloud top phase partitioning in different cloud types using active and passive satellite sensors. *Geophysical Research Letters*, *48*(2). doi: 10.1029/2020GL089863
- Bühl, J., Seifert, P., Myagkov, A., & Ansmann, A. (2016). Measuring ice-and liquid-water properties in mixed-phase cloud layers at the Leipzig Cloudnet station. *Atmospheric Chemistry and Physics*. doi: 10.5194/acp-16-10609-2016
- Burrows, S. M., Hoose, C., Pöschl, U., & Lawrence, M. G. (2013). Ice nuclei in marine air: Biogenic particles or dust? *Atmospheric Chemistry and Physics*. doi: 10.5194/acp-13-245-2013
- Ceccaldi, M., Delanoë, J., Hogan, R. J., Pounder, N. L., Protat, A., & Pelon, J. (2013). From cloudsat-calipso to earthcare: Evolution of the dardar cloud classification and its comparison to airborne radar-lidar observations. *Journal of Geophysical Research: Atmospheres*, *118*(14), 7962-7981. doi: 10.1002/jgrd.50579
- Ceppi, P., Hartmann, D. L., & Webb, M. J. (2016). Mechanisms of the negative shortwave cloud feedback in middle to high latitudes. *Journal of Climate*, *29*(1), 139 - 157. doi: 10.1175/JCLI-D-15-0327.1
- Cesana, G., & Chepfer, H. (2013). Evaluation of the cloud thermodynamic phase in a climate model using CALIPSO-GOCCP. *Journal of Geophysical Research Atmospheres*, *118*(14), 7922-7937. doi: 10.1002/jgrd.50376
- Cesana, G., Waliser, D. E., Jiang, X., & Li, J. L. (2015). Multimodel evaluation of cloud phase transition using satellite and reanalysis data. *Journal of Geophysical Research*, *120*(15), 7871-7892. doi: 10.1002/2014JD022932

- Chepfer, H., Bony, S., Winker, D., Cesana, G., Dufresne, J. L., Minnis, P., . . . Zeng, S. (2010). The GCM-oriented CALIPSO cloud product (CALIPSO-GOCCP). *Journal of Geophysical Research Atmospheres*, *115*(5). doi: 10.1029/2009JD012251
- Choi, Y.-S., Lindzen, R. S., Ho, C.-H., & Kim, J. (2010). Space observations of cold-cloud phase change. *Proceedings of the National Academy of Sciences*, *107*(25), 11211–11216. doi: 10.1073/pnas.1006241107
- Claquin, T., Schulz, M., & Balkanski, Y. J. (1999). Modeling the mineralogy of atmospheric dust sources. *Journal of Geophysical Research Atmospheres*. doi: 10.1029/1999JD900416
- Connolly, P. J., Möhler, O., Field, P. R., Saathoff, H., Burgess, R., Choularton, T., & Gallagher, M. (2009). Studies of heterogeneous freezing by three different desert dust samples. *Atmospheric Chemistry and Physics*, *9*(8), 2805–2824. doi: 10.5194/acp-9-2805-2009
- Coopman, Q., Riedi, J., Zeng, S., & Garrett, T. J. (2020). Space-based analysis of the cloud thermodynamic phase transition for varying microphysical and meteorological regimes. *Geophysical Research Letters*, *47*(6), e2020GL087122. doi: 10.1029/2020GL087122
- Cowie, S. M., Knippertz, P., & Marsham, J. H. (2014). A climatology of dust emission events from Northern Africa using long-term surface observations. *Atmospheric Chemistry and Physics*, *14*(16), 8579–8597. doi: 10.5194/acp-14-8579-2014
- Cuevas, E., Camino, C., Benedetti, A., Basart, S., Terradellas, E., Baldasano, J. M., . . . Schulz, M. (2015). The MACC-II 2007-2008 reanalysis: atmospheric dust evaluation and characterization over northern Africa and the Middle East. *Atmospheric Chemistry and Physics*, *15*(8), 3991–4024. doi: 10.5194/acp-15-3991-2015
- Cziczo, D. J., Froyd, K. D., Gallavardin, S. J., Moehler, O., Benz, S., Saathoff, H., & Murphy, D. M. (2009). Deactivation of ice nuclei due to atmospherically relevant surface coatings. *Environmental Research Letters*, *4*(4). doi: 10.1088/1748-9326/4/4/044013
- De Boer, G., Morrison, H., Shupe, M. D., & Hildner, R. (2011). Evidence of liquid dependent ice nucleation in high-latitude stratiform clouds from surface remote sensors. *Geophysical Research Letters*. doi: 10.1029/2010GL046016
- Dee, D. P., Uppala, S. M., Simmons, A. J., Berrisford, P., Poli, P., Kobayashi, S., . . . Vitart, F. (2011). The ERA-Interim reanalysis: configuration and performance of the data assimilation system. *Quarterly Journal of the Royal Meteorological Society*, *137*(656), 553–597. doi: 10.1002/qj.828
- Delanoë, J., & Hogan, R. J. (2010). Combined CloudSat-CALIPSO-MODIS retrievals of the properties of ice clouds. *Journal of Geophysical Research Atmospheres*, *115*(4). doi: 10.1029/2009JD012346
- DeMott, P. J., Prenni, A. J., Liu, X., Kreidenweis, S. M., Petters, M. D., Twohy, C. H., . . . Rogers, D. C. (2010). Predicting global atmospheric ice nuclei distributions and their impacts on climate. *Proceedings of the National Academy of Sciences of the United States of America*, *107*(25), 11217–11222. doi: 10.1073/pnas.0910818107
- Diehl, K., Simmel, M., & Wurzler, S. (2006). Numerical sensitivity studies on the impact of aerosol properties and drop freezing modes on the glaciation, microphysics and dynamics of clouds. *Journal of Geophysical Research Atmospheres*. doi: 10.1029/2005JD005884
- Diehl, K., & Wurzler, S. (2004). Heterogeneous Drop Freezing in the Immersion Mode: Model

- Calculations Considering Soluble and Insoluble Particles in the Drops. *Journal of the Atmospheric Sciences*. doi: 10.1175/1520-0469(2004)061(2063:hdfiti)2.0.co;2
- Dietlicher, R., Neubauer, D., & Lohmann, U. (2018). Prognostic parameterization of cloud ice with a single category in the aerosol-climate model ECHAM(v6.3.0)-HAM(v2.3). *Geoscientific Model Development*, 11(4), 1557–1576. doi: 10.5194/gmd-11-1557-2018
- Dietlicher, R., Neubauer, D., & Lohmann, U. (2019). Elucidating ice formation pathways in the aerosol–climate model echam6-ham2. *Atmospheric Chemistry and Physics*, 19(14), 9061–9080. doi: 10.5194/acp-19-9061-2019
- Dubovik, O., Smirnov, A., Holben, B. N., King, M. D., Kaufman, Y. J., Eck, T. F., & Slutsker, I. (2000). Accuracy assessments of aerosol optical properties retrieved from Aerosol Robotic Network (AERONET) Sun and sky radiance measurements. *Journal of Geophysical Research Atmospheres*, 105(D8), 9791–9806. doi: 10.1029/2000JD900040
- Eskes, H., Huijnen, V., Arola, A., Benedictow, A., Blechschmidt, A. M., Botek, E., . . . Zerefos, C. (2015). Validation of reactive gases and aerosols in the MACC global analysis and forecast system. *Geoscientific Model Development*, 8(11), 3523–3543. doi: 10.5194/gmd-8-3523-2015
- Field, P. R., Lawson, R. P., Brown, P. R. A., Lloyd, G., Westbrook, C., Moiseev, D., . . . Sullivan, S. (2017). Secondary Ice Production: Current State of the Science and Recommendations for the Future. *Meteorological Monographs*, 58, 7.1-7.20. doi: 10.1175/AMSMONOGRAPHS-D-16-0014.1
- Findeisen, W., Volken, E., Giesche, A. M., & Brönnimann, S. (2015). Colloidal meteorological processes in the formation of precipitation. *Meteorologische Zeitschrift*, 24(4), 443-454. doi: 10.1127/metz/2015/0675
- Forbes, R. M., & Ahlgrim, M. (2014). On the representation of high-latitude boundary layer mixed-phase cloud in the ecmwf global model. *Monthly Weather Review*, 142(9), 3425 - 3445. doi: 10.1175/MWR-D-13-00325.1
- Fröhlich-Nowoisky, J., Hill, T. C., Pummer, B. G., Yordanova, P., Franc, G. D., & Pöschl, U. (2015). Ice nucleation activity in the widespread soil fungus *Mortierella alpina*. *Biogeosciences*. doi: 10.5194/bg-12-1057-2015
- Georgoulias, A. K., Tsikerdekis, A., Amiridis, V., Marinou, E., Benedetti, A., Zanis, P., . . . Lelieveld, J. (2018). A 3-D evaluation of the MACC reanalysis dust product over Europe, northern Africa and Middle East using CALIOP/CALIPSO dust satellite observations. *Atmos. Chem. Phys*, 18, 8601–8620. doi: 10.5194/acp-18-8601-2018
- Gettelman, A., & Morrison, H. (2015). Advanced two-moment bulk microphysics for global models. Part I: Off-line tests and comparison with other schemes. *J. Clim.*, 28(3), 1268–1287. doi: 10.1175/JCLI-D-14-00102.1
- Golaz, J., Caldwell, P. M., Van Roekel, L. P., Petersen, M. R., Tang, Q., Wolfe, J. D., . . . Zhu, Q. (2019). The DOE E3SM coupled model version 1: Overview and evaluation at standard resolution. *J. Adv. Model. Earth Syst.* doi: 10.1029/2018ms001603
- Golaz, J.-C., Larson, V. E., & Cotton, W. R. (2002). A PDF-Based Model for Boundary Layer Clouds. Part I: Method and Model Description. *J. Atmos. Sci.*, 59(24), 3540–3551. doi: 10.1175/1520-0469(2002)059(3540:APBMFB)2.0.CO;2

- Gryspeerd, E., Quaas, J., & Bellouin, N. (2016). Constraining the aerosol influence on cloud fraction. *Journal of Geophysical Research*. doi: 10.1002/2015JD023744
- Hallett, J., & Mossop, S. C. (1974). Production of secondary ice particles during the riming process. *Nature*, *249*(5452), 26–28. doi: 10.1038/249026a0
- Hartmann, S., Wex, H., Clauss, T., Augustin-Bauditz, S., Niedermeier, D., Rösch, M., & Stratmann, F. (2016). Immersion Freezing of Kaolinite: Scaling with Particle Surface Area. *Journal of the Atmospheric Sciences*. doi: 10.1175/JAS-D-15-0057.1
- Hauke, J., & Kossowski, T. (2011). Comparison of values of pearson’s and spearman’s correlation coefficients on the same sets of data. *Quaestiones Geographicae*. doi: 10.2478/v10117-011-0021-1
- Hawcroft, M., Haywood, J. M., Collins, M., Jones, A., Jones, A. C., & Stephens, G. (2017). Southern Ocean albedo, inter-hemispheric energy transports and the double ITCZ: global impacts of biases in a coupled model. *Climate Dynamics*, *48*(7-8), 2279–2295. doi: 10.1007/s00382-016-3205-5
- Heymsfield, A. J., Kennedy, P. C., Massie, S., Schmitt, C., Wang, Z., Haimov, S., & Rangno, A. (2010). Aircraft-induced hole punch and canal clouds: Inadvertent cloud seeding. *Bulletin of the American Meteorological Society*, *91*(6), 753 - 766. doi: 10.1175/2009BAMS2905.1
- Hoose, C., Kristjánsson, J. E., Chen, J.-P., & Hazra, A. (2010). A Classical-Theory-Based Parameterization of Heterogeneous Ice Nucleation by Mineral Dust, Soot, and Biological Particles in a Global Climate Model. *Journal of the Atmospheric Sciences*, *67*(8), 2483-2503. doi: 10.1175/2010JAS3425.1
- Hoose, C., Lohmann, U., Erdin, R., & Tegen, I. (2008). The global influence of dust mineralogical composition on heterogeneous ice nucleation in mixed-phase clouds. *Environmental Research Letters*. doi: 10.1088/1748-9326/3/2/025003
- Hoose, C., & Möhler, O. (2012). Heterogeneous ice nucleation on atmospheric aerosols: A review of results from laboratory experiments. *Atmospheric Chemistry and Physics*, *12*(20), 9817–9854. doi: 10.5194/acp-12-9817-2012
- Hu, W., Murata, K., Fan, C., Huang, S., Matsusaki, H., Fu, P., & Zhang, D. (2020). Abundance and viability of particle-attached and free-floating bacteria in dusty and nondusty air. *Biogeosciences*, *17*(17), 4477–4487. doi: 10.5194/bg-17-4477-2020
- Hu, Y., Rodier, S., Xu, K. M., Sun, W., Huang, J., Lin, B., ... Josset, D. (2010). Occurrence, liquid water content, and fraction of supercooled water clouds from combined CALIOP/IIR/MODIS measurements. *Journal of Geophysical Research Atmospheres*. doi: 10.1029/2009JD012384
- Hu, Y., Winker, D., Vaughan, M., Lin, B., Omar, A., Trepte, C., ... Kuehn, R. (2009). CALIPSO/CALIOP cloud phase discrimination algorithm. *Journal of Atmospheric and Oceanic Technology*, *26*(11), 2293–2309. doi: 10.1175/2009JTECHA1280.1
- Huang, L., Jiang, J. H., Wang, Z., Su, H., Deng, M., & Massie, S. (2015). Climatology of cloud water content associated with different cloud types observed by A-Train satellites. *Journal of Geophysical Research*. doi: 10.1002/2014JD022779
- Huang, W., Ickes, L., Tegen, I., Rinaldi, M., Ceburnis, D., & Lohmann, U. (2018). Global relevance of marine organic aerosol as ice nucleating particles. *Atmospheric Chemistry*

- and *Physics*, 18(15), 11423–11445. doi: 10.5194/acp-18-11423-2018
- Huang, Y., Siems, S. T., Manton, M. J., Protat, A., & Delanoë, J. (2012). A study on the low-altitude clouds over the Southern Ocean using the DARDAR-MASK. *Journal of Geophysical Research Atmospheres*, 117(17). doi: 10.1029/2012JD017800
- Ickes, L. (2015). *Using classical nucleation theory for parameterizing immersion freezing in mixed-phase clouds in global climate models* (Doctoral dissertation, ETH Zurich, Zürich). doi: 10.3929/ethz-a-010564637
- Ickes, L., Welti, A., & Lohmann, U. (2017). Classical nucleation theory of immersion freezing: Sensitivity of contact angle schemes to thermodynamic and kinetic parameters. *Atmospheric Chemistry and Physics*, 17(3), 1713–1739. doi: 10.5194/acp-17-1713-2017
- Inness, A., Ades, M., Agustí-Panareda, A., Barr, J., Benedictow, A., Blechschmidt, A. M., ... Suttie, M. (2019). The CAMS reanalysis of atmospheric composition. *Atmospheric Chemistry and Physics*, 19(6), 3515–3556. doi: 10.5194/acp-19-3515-2019
- IPCC, Chidthaisong, A., Ciais, P., Cox, P., Dickinson, R., Hauglustaine, D., ... Zhang, X. (2007). *Climate Change 2007: Working Group I: The Physical Science Basis* (Tech. Rep.).
- Johnson, M. S., Meskhidze, N., Kiliyanpilakkil, V. P., & Gassó, S. (2011). Understanding the transport of Patagonian dust and its influence on marine biological activity in the South Atlantic Ocean. *Atmospheric Chemistry and Physics*, 11(6), 2487–2502. doi: 10.5194/acp-11-2487-2011
- Kanitz, T., Seifert, P., Ansmann, A., Engelmann, R., Althausen, D., Casiccia, C., & Rohwer, E. G. (2011). Contrasting the impact of aerosols at northern and southern midlatitudes on heterogeneous ice formation. *Geophysical Research Letters*, 38(17). doi: 10.1029/2011GL048532
- Kanji, Z. A., Ladino, L. A., Wex, H., Boose, Y., Burkert-Kohn, M., Cziczo, D. J., & Krämer, M. (2017). Overview of Ice Nucleating Particles. *Meteorological Monographs*, 58, 1.1–1.33. doi: 10.1175/amsmonographs-d-16-0006.1
- Kawamoto, K., Yamauchi, A., Suzuki, K., Okamoto, H., & Li, J. (2020). Effect of dust load on the cloud top ice-water partitioning over northern middle to high latitudes with calipso products. *Geophysical Research Letters*, 47(15). doi: 10.1029/2020GL088030
- Kiselev, A., Bachmann, F., Pedevilla, P., Cox, S. J., Michaelides, A., Gerthsen, D., & Leisner, T. (2017). Active sites in heterogeneous ice nucleation—the example of k-rich feldspars. *Science*, 355(6323), 367–371. doi: 10.1126/science.aai8034
- Klein, S. A., & Hartmann, D. L. (1993). The seasonal cycle of low stratiform clouds. *Journal of Climate*. doi: 10.1175/1520-0442(1993)006<1587:TSCOLS>2.0.CO;2
- Koffi, B., Schulz, M., Bréon, F.-M., Dentener, F., Steensen, B. M., Griesfeller, J., ... Zhang, K. (2016). Evaluation of the aerosol vertical distribution in global aerosol models through comparison against caliop measurements: AeroCom phase ii results. *Journal of Geophysical Research: Atmospheres*, 121(12), 7254–7283. doi: 10.1002/2015JD024639
- Kok, J. F. (2011). A scaling theory for the size distribution of emitted dust aerosols suggests climate models underestimate the size of the global dust cycle. *Proceedings of the National Academy of Sciences*, 108(3), 1016–1021. doi: 10.1073/pnas.1014798108

- Kok, J. F., Adebisi, A. A., Albani, S., Balkanski, Y., Checa-Garcia, R., Chin, M., ... Wan, J. S. (2021). Contribution of the world's main dust source regions to the global cycle of desert dust. *Atmospheric Chemistry and Physics Discussions*, 2021, 1–34. doi: 10.5194/acp-2021-4
- Korolev, A., McFarquhar, G., Field, P. R., Franklin, C., Lawson, P., Wang, Z., ... Wendisch, M. (2017). Mixed-Phase Clouds: Progress and Challenges. *Meteorological Monographs*, 58, 5.1–5.50. doi: 10.1175/AMSMONOGRAPHIS-D-17-0001.1
- Lacher, L., DeMott, P. J., Levin, E. J. T., Suski, K. J., Boose, Y., Zipori, A., ... Kanji, Z. A. (2018). Background Free Tropospheric Ice Nucleating Particle Concentrations at Mixed phase Cloud Conditions. *Journal of Geophysical Research: Atmospheres*. doi: 10.1029/2018JD028338
- Larson, V. E., & Golaz, J.-C. (2005). Using Probability Density Functions to Derive Consistent Closure Relationships among Higher-Order Moments. *Mon. Weather Rev.*, 133(4), 1023–1042. doi: 10.1175/MWR2902.1
- Lauber, A., Kiselev, A., Pander, T., Handmann, P., & Leisner, T. (2018). Secondary Ice Formation during Freezing of Levitated Droplets. *Journal of the Atmospheric Sciences*, 75(8), 2815–2826. doi: 10.1175/JAS-D-18-0052.1
- Li, F., Ginoux, P., & Ramaswamy, V. (2008). Distribution, transport, and deposition of mineral dust in the Southern Ocean and Antarctica: Contribution of major sources. *Journal of Geophysical Research Atmospheres*, 113(10). doi: 10.1029/2007JD009190
- Li, J., Lv, Q., Zhang, M., Wang, T., Kawamoto, K., Chen, S., & Zhang, B. (2017). Effects of atmospheric dynamics and aerosols on the fraction of supercooled water clouds. *Atmospheric Chemistry and Physics*, 17(3), 1847–1863. doi: 10.5194/acp-17-1847-2017
- Li, R., Dong, X., Guo, J., Fu, Y., Zhao, C., Wang, Y., & Min, Q. (2017). The implications of dust ice nuclei effect on cloud top temperature in a complex mesoscale convective system. *Scientific Reports*. doi: 10.1038/s41598-017-12681-0
- Liu, X., Ma, P. L., Wang, H., Tilmes, S., Singh, B., Easter, R. C., ... Rasch, P. J. (2016). Description and evaluation of a new four-mode version of the Modal Aerosol Module (MAM4) within version 5.3 of the Community Atmosphere Model. *Geosci. Model Dev.*, 9(2), 505–522. doi: 10.5194/gmd-9-505-2016
- Lohmann, U., & Diehl, K. (2006). Sensitivity studies of the importance of dust ice nuclei for the indirect aerosol effect on stratiform mixed-phase clouds. *Journal of the Atmospheric Sciences*, 63(3), 968–982. doi: 10.1175/JAS3662.1
- Lohmann, U., Stier, P., Hoose, C., Ferrachat, S., Kloster, S., Roeckner, E., & Zhang, J. (2007). Cloud microphysics and aerosol indirect effects in the global climate model echam5-ham. *Atmospheric Chemistry and Physics*, 7(13), 3425–3446. doi: 10.5194/acp-7-3425-2007
- Luo, T., Wang, Z., Zhang, D., Liu, X., Wang, Y., & Yuan, R. (2015). Global dust distribution from improved thin dust layer detection using a-train satellite lidar observations. *Geophysical Research Letters*, 42(2), 620–628. doi: 10.1002/2014GL062111
- Mahowald, N., Albani, S., Kok, J. F., Engelstaeder, S., Scanza, R., Ward, D. S., & Flanner, M. G. (2014). The size distribution of desert dust aerosols and its impact on the Earth system. *Aeolian Research*, 15, 53–71. doi: 10.1016/j.aeolia.2013.09.002

- Matus, A. V., & L'Ecuyer, T. S. (2017). The role of cloud phase in Earth's radiation budget. *Journal of Geophysical Research*, *122*(5), 2559–2578. doi: 10.1002/2016JD025951
- McCoy, D. T., Hartmann, D. L., & Grosvenor, D. P. (2014a). Observed southern ocean cloud properties and shortwave reflection. part i: Calculation of sw flux from observed cloud properties. *Journal of Climate*, *27*(23), 8836 - 8857. doi: 10.1175/JCLI-D-14-00287.1
- McCoy, D. T., Hartmann, D. L., & Grosvenor, D. P. (2014b). Observed southern ocean cloud properties and shortwave reflection. part ii: Phase changes and low cloud feedback. *Journal of Climate*, *27*(23), 8858 - 8868. doi: 10.1175/JCLI-D-14-00288.1
- McCoy, D. T., Hartmann, D. L., Zelinka, M. D., Ceppi, P., & Grosvenor, D. P. (2015). Mixed-phase cloud physics and southern ocean cloud feedback in climate models. *Journal of Geophysical Research: Atmospheres*, *120*(18), 9539-9554. doi: 10.1002/2015JD023603
- McCoy, D. T., Tan, I., Hartmann, D. L., Zelinka, M. D., & Storelvmo, T. (2016). On the relationships among cloud cover, mixed-phase partitioning, and planetary albedo in GCMs. *Journal of Advances in Modeling Earth Systems*. doi: 10.1002/2015MS000589
- Mioche, G., Jourdan, O., Ceccaldi, M., & Delanoë, J. (2014). Variability of the mixed phase in the Arctic with a focus on the Svalbard region: A study based on spaceborne active remote sensing. *Atmospheric Chemistry and Physics Discussions*, *14*(16), 23453–23497. doi: 10.5194/acpd-14-23453-2014
- Morrison, A. E., Siems, S. T., & Manton, M. J. (2011). A three-year climatology of cloud-top phase over the Southern Ocean and North Pacific. *Journal of Climate*, *24*(9), 2405–2418. doi: 10.1175/2010JCLI3842.1
- Morrison, H., De Boer, G., Feingold, G., Harrington, J., Shupe, M. D., & Sulia, K. (2012). Resilience of persistent Arctic mixed-phase clouds. *Nature Geoscience*, *5*(1), 11–17. doi: 10.1038/ngeo1332
- Morrison, H., & Milbrandt, J. A. (2015). Parameterization of cloud microphysics based on the prediction of bulk ice particle properties. part i: Scheme description and idealized tests. *Journal of the Atmospheric Sciences*, *72*(1), 287-311. doi: 10.1175/JAS-D-14-0065.1
- Mülmenstädt, J., Nam, C., Salzmann, M., Kretzschmar, J., L'Ecuyer, T. S., Lohmann, U., . . . Quaas, J. (2020). Reducing the aerosol forcing uncertainty using observational constraints on warm rain processes. *Science Advances*, *6*(22). doi: 10.1126/sciadv.aaz6433
- Murray, B. J., Broadley, S. L., Wilson, T. W., Atkinson, J. D., & Wills, R. H. (2011). Heterogeneous freezing of water droplets containing kaolinite particles. *Atmospheric Chemistry and Physics*. doi: 10.5194/acp-11-4191-2011
- Murray, B. J., Carslaw, K. S., & Field, P. R. (2021). Opinion: Cloud-phase climate feedback and the importance of ice-nucleating particles. *Atmospheric Chemistry and Physics*, *21*(2), 665–679. doi: 10.5194/acp-21-665-2021
- Mülmenstädt, J., Sourdeval, O., Delanoë, J., & Quaas, J. (2015). Frequency of occurrence of rain from liquid-, mixed-, and ice-phase clouds derived from a-train satellite retrievals. *Geophysical Research Letters*, *42*(15), 6502-6509. doi: 10.1002/2015GL064604
- Neale, R. B., Chen, C.-c., Lauritzen, P. H., Williamson, D. L., Conley, A. J., Smith, A. K., . . . Morrison, H. (2004). Description of the NCAR Community Atmosphere Model (CAM 5.0). *Ncar/Tn-464+Str*(June), 214. doi: 10.5065/D6N877R0.

- Neubauer, D., Ferrachat, S., Siegenthaler-Le Drian, C., Stier, P., Partridge, D. G., Tegen, I., ... Lohmann, U. (2019). The global aerosol-climate model ECHAM6.3-HAM2.3-Part 2: Cloud evaluation, aerosol radiative forcing, and climate sensitivity. *Geoscientific Model Development*, 12(8), 3609–3639. doi: 10.5194/gmd-12-3609-2019
- Niedermeier, D., Augustin-Bauditz, S., Hartmann, S., Wex, H., Ignatius, K., & Stratmann, F. (2015). Can we define an asymptotic value for the ice active surface site density for heterogeneous ice nucleation? *Journal of Geophysical Research*. doi: 10.1002/2014JD022814
- Niedermeier, D., Shaw, R. A., Hartmann, S., Wex, H., Clauss, T., Voigtländer, J., & Stratmann, F. (2011). Heterogeneous ice nucleation: Exploring the transition from stochastic to singular freezing behavior. *Atmospheric Chemistry and Physics*. doi: 10.5194/acp-11-8767-2011
- Niemand, M., Möhler, O., Vogel, B., Vogel, H., Hoose, C., Connolly, P., ... Leisner, T. (2012). A particle-surface-area-based parameterization of immersion freezing on desert dust particles. *Journal of the Atmospheric Sciences*, 69(10), 3077–3092. doi: 10.1175/JAS-D-11-0249.1
- O’Sullivan, D., Adams, M. P., Tarn, M. D., Harrison, A. D., Vergara-Temprado, J., Porter, G. C. E., ... Murray, B. J. (2018). Contributions of biogenic material to the atmospheric ice-nucleating particle population in North Western Europe. *Scientific Reports*, 8(1), 13821. doi: 10.1038/s41598-018-31981-7
- O’Sullivan, D., Murray, B. J., Malkin, T. L., Whale, T. F., Umo, N. S., Atkinson, J. D., ... Webb, M. E. (2014). Ice nucleation by fertile soil dusts: relative importance of mineral and biogenic components. *Atmospheric Chemistry and Physics*, 14(4), 1853–1867. doi: 10.5194/acp-14-1853-2014
- O’Sullivan, D., Murray, B. J., Ross, J. F., & Webb, M. E. (2016). The adsorption of fungal ice-nucleating proteins on mineral dusts: a terrestrial reservoir of atmospheric ice-nucleating particles. *Atmospheric Chemistry and Physics*, 16(12), 7879–7887. doi: 10.5194/acp-16-7879-2016
- Pavolonis, M. J., Heidinger, A. K., & Uttal, T. (2005). Daytime global cloud typing from AVHRR and VIIRS: Algorithm description, validation, and comparisons. *Journal of Applied Meteorology*, 44(6), 804–826. doi: 10.1175/JAM2236.1
- Petters, M. D., & Wright, T. P. (2015). Revisiting ice nucleation from precipitation samples. *Geophysical Research Letters*. doi: 10.1002/2015GL065733
- Price, H. C., Baustian, K. J., McQuaid, J. B., Blyth, A., Bower, K. N., Choularton, T., ... Murray, B. J. (2018). Atmospheric Ice-Nucleating Particles in the Dusty Tropical Atlantic. *Journal of Geophysical Research: Atmospheres*. doi: 10.1002/2017JD027560
- Randall, D. A., Wood, R. A., Bony, S., Colman, R., Fichet, T., Fyfe, J., ... Taylor, K. E. (2007). Climate Models and Their Evaluation. *Climate Change 2007: The Physical Science Basis. Contribution of Working Group I to the Fourth Assessment Report of the Intergovernmental Panel on Climate Change*. doi: 10.1016/j.cub.2007.06.045
- Rasch, P. J., Xie, S., Ma, P.-l., Lin, W., Wang, H., Tang, Q., & Burrows, S. M. (2019). An Overview of the Atmospheric Component of the Energy Exascale Earth System Model. *J. Adv. Model. Earth Syst.*, 11(8), 2377–2411. doi: 10.1029/2019MS001629

- Ridley, D. A., Heald, C. L., Kok, J. F., & Zhao, C. (2016). An observationally constrained estimate of global dust aerosol optical depth. *Atmospheric Chemistry and Physics*, *16*(23), 15097–15117. doi: 10.5194/acp-16-15097-2016
- Riedi, J., Marchant, B., Platnick, S., Baum, B. A., Thieuleux, F., Oudard, C., ... Dubuisson, P. (2010). Cloud thermodynamic phase inferred from merged POLDER and MODIS data. *Atmospheric Chemistry and Physics*. doi: 10.5194/acp-10-11851-2010
- Sassen, K., & Wang, Z. (2008). Classifying clouds around the globe with the CloudSat radar: 1-year of results. *Geophysical Research Letters*, *35*(4). doi: 10.1029/2007GL032591
- Scott, R. C., & Lubin, D. (2016). Unique manifestations of mixed-phase cloud microphysics over Ross Island and the Ross Ice Shelf, Antarctica. *Geophysical Research Letters*. doi: 10.1002/2015GL067246
- Seifert, P., Ansmann, A., Mattis, I., Wandinger, U., Tesche, M., Engelmann, R., ... Hausteiner, K. (2010). Saharan dust and heterogeneous ice formation: Eleven years of cloud observations at a central European EARLINET site. *Journal of Geophysical Research Atmospheres*, *115*(20). doi: 10.1029/2009JD013222
- Seinfeld, J. H., Bretherton, C., Carslaw, K. S., Coe, H., DeMott, P. J., Dunlea, E. J., ... Wood, R. (2016). Improving our fundamental understanding of the role of aerosol-cloud interactions in the climate system. *Proceedings of the National Academy of Sciences*, *113*(21), 5781–5790. doi: 10.1073/pnas.1514043113
- Seinfeld, J. H., & Pandis, S. N. (1998). Atmospheric Chemistry and Physics: From Air Pollution to Climate Change. *Atmospheric chemistry and physics from air pollution to climate change Publisher New York NY Wiley 1998 Physical description xxvii 1326 p A WileyInterscience Publication ISBN 0471178152*, *51*, 1–4. doi: 10.1080/00139157.1999.10544295
- Shi, Y., & Liu, X. (2019). Dust radiative effects on climate by glaciating mixed-phase clouds. *Geophysical Research Letters*, *46*(11), 6128–6137. doi: 10.1029/2019GL082504
- Solomon, A., Feingold, G., & Shupe, M. D. (2015). The role of ice nuclei recycling in the maintenance of cloud ice in arctic mixed-phase stratocumulus. *Atmospheric Chemistry and Physics*, *15*(18), 10631–10643. doi: 10.5194/acp-15-10631-2015
- Stanelle, T., Bey, I., Raddatz, T., Reick, C., & Tegen, I. (2014). Anthropogenically induced changes in twentieth century mineral dust burden and the associated impact on radiative forcing. *Journal of Geophysical Research: Atmospheres*, *119*(23), 13,526–13,546. doi: 10.1002/2014JD022062
- Stengel, M., Stapelberg, S., Sus, O., Finkensieper, S., Würzler, B., Philipp, D., ... McGarragh, G. (2020). Cloud_cci advanced very high resolution radiometer post meridiem (avhrr-pm) dataset version 3: 35-year climatology of global cloud and radiation properties. *Earth System Science Data*, *12*(1), 41–60. doi: 10.5194/essd-12-41-2020
- Sullivan, S. C., Hoose, C., Kiselev, A., Leisner, T., & Nenes, A. (2018). Initiation of secondary ice production in clouds. *Atmospheric Chemistry and Physics*, *18*(3), 1593–1610. doi: 10.5194/acp-18-1593-2018
- Sullivan, S. C., Lee, D., Oreopoulos, L., & Nenes, A. (2016). Role of updraft velocity in temporal variability of global cloud hydrometeor number. *Proceedings of the National Academy of Sciences*, *113*(21), 5791–5796. doi: 10.1073/pnas.1514039113

- Tan, I., Storelvmo, T., & Choi, Y. S. (2014). Spaceborne lidar observations of the ice-nucleating potential of dust, polluted dust, and smoke aerosols in mixed-phase clouds. *Journal of Geophysical Research*, *119*(11), 6653–6665. doi: 10.1002/2013JD021333
- Tan, I., Storelvmo, T., & Zelinka, M. D. (2016). Observational constraints on mixed-phase clouds imply higher climate sensitivity. *Science*, *352*(6282), 224–227. doi: 10.1126/science.aad5300
- Tegen, I., Neubauer, D., Ferrachat, S., Drian, C. S. L., Bey, I., Schutgens, N., ... Lohmann, U. (2019). The global aerosol-climate model echam6.3-ham2.3 -Part 1: Aerosol evaluation. *Geoscientific Model Development*, *12*(4), 1643–1677. doi: 10.5194/gmd-12-1643-2019
- Toth, T. D., Campbell, J. R., Reid, J. S., Tackett, J. L., Vaughan, M. A., Zhang, J., & Marquis, J. W. (2018). Minimum aerosol layer detection sensitivities and their subsequent impacts on aerosol optical thickness retrievals in CALIPSO level 2 data products. *Atmospheric Measurement Techniques*, *11*(1), 499–514. doi: 10.5194/amt-11-499-2018
- Trenberth, K. E., & Fasullo, J. T. (2010). Simulation of Present-Day and Twenty-First-Century Energy Budgets of the Southern Oceans. *Journal of Climate*, *23*(2), 440–454. doi: 10.1175/2009JCLI3152.1
- Twomey, S. (1974). Pollution and the planetary albedo. *Atmospheric Environment (1967)*, *8*(12), 1251 - 1256. doi: 10.1016/0004-6981(74)90004-3
- Vergara-Temprado, J., Miltenberger, A. K., Furtado, K., Grosvenor, D. P., Shipway, B. J., Hill, A. A., ... Carslaw, K. S. (2018). Strong control of Southern Ocean cloud reflectivity by ice-nucleating particles. *Proceedings of the National Academy of Sciences*, 201721627. doi: 10.1073/pnas.1721627115
- Vergara-Temprado, J., Murray, B. J., Wilson, T. W., O’Sullivan, D., Browse, J., Pringle, K. J., ... Carslaw, K. S. (2017). Contribution of feldspar and marine organic aerosols to global ice nucleating particle concentrations. *Atmospheric Chemistry and Physics*, *17*(5), 3637–3658. doi: 10.5194/acp-17-3637-2017
- Villanueva, D., Heinold, B., Seifert, P., Deneke, H., Radenz, M., & Tegen, I. (2020). The day-to-day co-variability between mineral dust and cloud glaciation: A proxy for heterogeneous freezing. *Atmospheric Chemistry and Physics*, *20*(4), 2177–2199. doi: 10.5194/acp-20-2177-2020
- Villanueva, D., Neubauer, D., Gasparini, B., Ickes, L., & Tegen, I. (2021). Constraining the impact of dust-driven droplet freezing on climate using cloud top phase observations. *Accepted to Geophysical Research Letters (with modifications)*.
- Villanueva, D., Senf, F., & Tegen, I. (2021). Hemispheric and seasonal contrast in cloud thermodynamic phase from a-train spaceborne instruments. *Journal of Geophysical Research: Atmospheres*. doi: 10.1029/2020jd034322
- Wagner, R., Kiselev, A., Moehler, O., Saathoff, H., & Steinke, I. (2016). Pre-activation of ice-nucleating particles by the pore condensation and freezing mechanism. *Atmospheric Chemistry and Physics*, *16*(4), 2025–2042. doi: 10.5194/acp-16-2025-2016
- Wegener, A. (1911). *Thermodynamik der Atmosphäre*. Leipzig: J.A. Barth.
- Welti, A., Lüönd, F., Stetzer, O., & Lohmann, U. (2009). Influence of particle size on the ice nucleating ability of mineral dusts. *Atmospheric Chemistry and Physics*. doi: 10.5194/

- Westbrook, C. D., & Illingworth, A. J. (2011). Evidence that ice forms primarily in supercooled liquid clouds at temperatures $> 27^{\circ}\text{C}$. *Geophysical Research Letters*, *38*(14). doi: 10.1029/2011GL048021
- Wu, M., Liu, X., Yu, H., Wang, H., Shi, Y., Yang, K., ... Ke, Z. (2020). Understanding processes that control dust spatial distributions with global climate models and satellite observations. *Atmospheric Chemistry and Physics*, *20*(22), 13835–13855. doi: 10.5194/acp-20-13835-2020
- Wu, Y., Cordero, L., Gross, B., Moshary, F., & Ahmed, S. (2014). Assessment of CALIPSO attenuated backscatter and aerosol retrievals with a combined ground-based multi-wavelength lidar and sunphotometer measurement. *Atmospheric Environment*, *84*, 44–53. doi: 10.1016/j.atmosenv.2013.11.016
- Xie, S., Lin, W., Rasch, P. J., Ma, P.-L., Neale, R., Larson, V. E., ... Zhang, Y. (2018). Understanding Cloud and Convective Characteristics in Version 1 of the E3SM Atmosphere Model. *J. Adv. Model. Earth Syst.*, *10*, 1–27. doi: 10.1029/2018MS001350
- Yun, Y., & Penner, J. E. (2013). An evaluation of the potential radiative forcing and climatic impact of marine organic aerosols as heterogeneous ice nuclei. *Geophysical Research Letters*, *40*(15), 4121–4126. doi: 10.1002/grl.50794
- Yun, Y., Penner, J. E., & Popovicheva, O. (2013). The effects of hygroscopicity on ice nucleation of fossil fuel combustion aerosols in mixed-phase clouds. *Atmospheric Chemistry and Physics*, *13*(8), 4339–4348. doi: 10.5194/acp-13-4339-2013
- Zamora, L. M., Kahn, R. A., Huebert, K. B., Stohl, A., & Eckhardt, S. (2018). A satellite-based estimate of combustion aerosol cloud microphysical effects over the Arctic Ocean. *Atmospheric Chemistry and Physics*. doi: 10.5194/acp-18-14949-2018
- Zelinka, M. D., Myers, T. A., McCoy, D. T., Po-Chedley, S., Caldwell, P. M., Ceppi, P., ... Taylor, K. E. (2020). Causes of higher climate sensitivity in cmip6 models. *Geophysical Research Letters*, *47*(1), e2019GL085782. (e2019GL085782 10.1029/2019GL085782) doi: 10.1029/2019GL085782
- Zender, C. S., & Kwon, E. Y. (2005). Regional contrasts in dust emission responses to climate. *Journal of Geophysical Research Atmospheres*, *110*(13). doi: 10.1029/2004JD005501
- Zhang, D., Liu, D., Luo, T., Wang, Z., & Yin, Y. (2015). Aerosol impacts on cloud thermodynamic phase change over East Asia observed with CALIPSO and CloudSat measurements. *Journal of Geophysical Research*, *120*(4), 1490–1501. doi: 10.1002/2014JD022630
- Zhang, D., Wang, Z., Heymsfield, A., Fan, J., Liu, D., & Zhao, M. (2012). Quantifying the impact of dust on heterogeneous ice generation in midlevel supercooled stratiform clouds. *Geophysical Research Letters*, *39*(17). doi: 10.1029/2012GL052831
- Zhang, D., Wang, Z., Kollias, P., Vogelmann, A. M., Yang, K., & Luo, T. (2018). Ice particle production in mid-level stratiform mixed-phase clouds observed with collocated A-Train measurements. *Atmospheric Chemistry and Physics*, *18*(6), 4317–4327. doi: 10.5194/acp-18-4317-2018
- Zhang, D., Wang, Z., & Liu, D. (2010). A global view of midlevel liquid-layer topped stratiform cloud distribution and phase partition from CALIPSO and CloudSat measurements.

List of Abbreviations

ACI	Aerosol Cloud Interactions
AOT	Aerosol Optical Thickness
CALIOP	Cloud-Aerosol Lidar with Orthogonal Polarization
CALIPSO	Cloud-Aerosol Lidar and Infrared Pathfinder Satellite Observations
CAMS	Copernicus Atmosphere Monitoring Service reanalysis
CCN	Cloud Condensation Nuclei
CPR	Cloud Profiling Radar
CRE	Cloud Radiative Effect
DARDAR	liDAR-raDAR
FPR	Frequency Phase Ratio
GDP	GOCCP-DARDAR-PML2
GOCCP	Global Climate Model Oriented Cloud Calipso Product
IFS	Integrated Forecast System
INAS	Ice Nucleating Active Sites
INP	Ice Nucleating Particle
IPCC	Intergovernmental Panel on Climate Change
lidar	light detection and ranging
LTSS	Lower Troposphere Static Stability
LW	LongWave
LWP	Liquid Water Path
MACC	Monitoring Atmospheric Composition and Climate reanalysis
MODIS	MODerate resolution Imaging Spectroradiometer
PARASOL	Polarization and Anisotropy of Reflectances for Atmospheric Sciences coupled with Observations from a Lidar
PM-L2	PARASOL and Aqua/MODIS Level 2 product
POLDER	POLarization and Directionality of the Earth Reflectance
radar	radio detection and ranging
RH	Relative Humidity
SCF	Supercooled Liquid Frequency
SIP	Secondary Ice Production
SW	ShortWave
SWIR	ShortWave-InfraRed
TIR	Thermal-InfraRed
TKE	Turbulent Kinetic Energy

TROPOS Leibniz Institute for **Tropo**spheric Research
UTSS Upper **Tropo**sphere **Stati**c **Stabi**lity
WBF **W**egener **B**ergeron **F**indeisen

List of Symbols

A_j	Dust particle surface area
CCN	Number concentration of ambient Cloud Condensation Nuclei
c_{dust}	Dust freezing efficiency
C_p	Specific heat capacity of air
cvf	cloud volume fraction
FF	Fraction of frozen droplets
FPR^*	Adjusted Frequency Phase Ration (-1: liquid, 0: no cloud, +1: ice)
g	Gravitational constant
J_{imm}	Immersion freezing rate
N_A	INP temperature dependence
N_B	INP temperature dependence
$N_{imm,dust}$	Dust particle number concentration in the soluble mod
n_s	Ice active surface site density of natural dust
$\omega_{largescale}$	Large-scale term from the vertical velocity
P_x	Pressure at the surface or at x hPa
q_l	Cloud liquid water mass-mixing ratio
R	Gas constant
ρ_{air}	Air density
ρ_l	Cloud droplet density
T	Temperature
T_x	Temperature at the surface or at x hPa
TKE	Turbulent Kinetic Energy

List of Figures

1.1	Diagram of the cloud-phase feedback	2
1.2	Main types of aerosol-cloud interactions	4
1.3	Ice processes in mixed-phase clouds	8
1.4	Factors controlling dust-INP efficiency	9
1.5	Top-down vs bottom-up	10
2.1	Flow chart of the datasets' rebinning and collocation	18
2.2	Diagram of the day-to-day decile concept	18
2.3	Zonal sample size of the CALIPSO-GOCCP product	19
2.4	Case study for the CALIPSO-GOCCP product	23
2.5	Global ice cloud occurrence-frequency for GOCCP	24
2.6	Zonal mean of cloud ice occurrence-frequency	25
2.7	Histogram for relative humidity and static stability	25
2.8	Cloud phase against dust loading at -15°C	27
2.9	Cloud phase against dust loading at -30°C	28
2.10	Cloud phase against dust loading at -22°C	29
2.11	Cloud phase against meteorological factors	32
2.12	Case study for the DARDAR and ALT-DARDAR products	41
2.13	Global ice cloud occurrence-frequency for DARDAR	41
2.14	Zonal mean of cloud ice occurrence-frequency for DARDAR	41
2.S1	Global variability of $\text{FPR}_{\text{DARDAR}}$	44
2.S2	Global variability of $\text{FPR}_{\text{ALT}_{\text{DARDAR}}}$	44
2.S3	Global variability of $\text{FPR}_{\text{GOCCP}}$	44
2.S4	Global variability of MACC coarse dust	45
2.S5	Global day-to-day variability of MACC coarse dust	45
2.S6	Global variability of MACC fine dust	45
2.S7	Global day-to-day variability of MACC fine dust	46
2.S8	Global variability of MACC cloud volume fraction	46
2.S9	Global variability of MACC stratiform cloud volume fraction	46
2.S10	Global variability of MACC vertical velocity	47
2.S11	Global variability of relative humidity	47
2.S12	Global variability of isotherm height	47
2.S13	Global variability of ECMWF-AUX temperature	48
2.S14	Global variability of sample size	48
2.S15	Seasonal variability of sample size	48

2.S16	Sample size for lowers and highest dust decile	49
2.S17	Day-to-day normalized covariance between dust and ice	49
2.S18	FPR _{GOCCP} against dust mixing ratio	50
2.S19	FPR _{GOCCP} against dust at -30°C and for winter/summer	50
2.S20	FPR _{GOCCP} over sea and land	51
3.1	Diagram of GDP ensemble derivation	56
3.2	Diagram of known retrieval biases	58
3.3	Product sample size, disagreement ratio and ice frequency.	61
3.4	Contour plot for the hemispheric and seasonal contrast	64
3.5	Hemispheric and seasonal contrast at the mid-latitudes	67
3.S1	GDP sample size and disagreement ratio against temperature	72
3.S2	Cloud phase North-south difference for individual products and two-member ensembles	73
3.S3	Cloud phase Hemispheric and seasonal contrast for GDP2 ensemble	74
3.S4	Cloud phase contrast between boreal spring and austral mean	75
3.S5	Diagram of satellite horizontal binning	76
3.S6	Diagram of ensemble vertical processing	76
3.S7	Diagram of ensemble temporal averaging	77
3.S8	Diagram of GDP agreement possibilities	77
3.S9	Time series of ice cloud frequency in the Northern Hemisphere	78
3.S10	Time series of ice cloud frequency in the Southern Hemisphere	78
4.1	Diagram explaining the tuning strategy	82
4.2	Glaciated fraction, and cloud phase contrast	85
4.S1	INAS concentration for ECHAM-HAM simulations	94
4.S2	E3SM cloud phase mean and contrast	95
4.S3	Cloud phase mean and contrast for different INP efficiency	96
4.S4	Cloud phase mean and contrast for different dust thresholds	97
4.S5	Cloud phase mean and contrast for different INP efficiency and a dust threshold of 10^{-6} kg^{-1}	98
4.S6	Cloud phase mean and contrast for constant CCN and TKE	99
4.S7	Cloud phase mean and contrast for constant aerosol fractions	100
4.S8	Climate impact of dust-driven droplet freezing on water content and radiation	101
4.S9	Climate impact of dust-driven droplet freezing on water content and radiation (nudged)	102
4.S10	Climate impact of dust-driven droplet freezing on water content and radiation (constant TKE and CCN)	103
4.S11	Climate impact of dust-driven droplet freezing on cloud cover and radiation (shortwave and longwave)	104
4.S12	Climate impact of dust-driven droplet freezing on precipitation	105
4.S13	Climate impact of dust-driven droplet freezing on droplet and ice number	106

List of Tables

2.1	North-south differences in cloud phase	37
2.2	Cloud phase product comparison	42
3.1	Sample size and ice frequency for individual products	69
3.2	Sample size and hemispheric contrast for individual products	69
4.1	Changes in key microphysical parameters due to dust-INP	88
4.S1	ECHAM-HAM simulations	93
4.S2	Change of key variables for NS and NS10K	93

Appendix A

Acknowledgements

I want to thank everyone who helped directly or indirectly during my PhD especially to:

- My supervisor Ina Tegen. Without her help, this project would not have been realized.
- Kerstin Schepanski, Bernd Heinold, Patric Seifert, Hartwig Deneke, Martin Radenz, Albert Ansmann, Johannes Mülmenstädt, Julien Delanoë, Fabian Senf, David Neubauer, Blaž Gasparini, and Luisa Ickes. They provided invaluable assistance during the preparation of the manuscripts on which the chapters of this dissertation were built, making the preparation of this dissertation much easier.
- The modelling department at TROPOS and the whole TROPOS institution, which provided continuous support during my PhD.
- Max, Xalo, and Imanol for providing so much spiritual guidance.
- Moritz, Christian, and Teresa for all your help during our Master's studies.
- Lio, Anna, Theresa, Jannis, Antonia, Sara, Nora, Laura, and Amelie for having so much patience when living with me, and helping me feel at home in Leipzig.
- Hannes, Clara(x2), Anne, Max, Hammud, Simon, Mary, Chris, Mirjam, Phillip, and Pia for so many great moments during the last years.
- Jenny for advising me to come to Leipzig and pursuit a career in Meteorology.
- Jule for being so patient and understanding during the hard times of my PhD.
- My family for being so supportive of my adventurous way of life.

They kept me going on and this work would not have been possible without their emotional support.

Appendix B

List of Publications

Part of this thesis

- Villanueva, D., Heinold, B., Seifert, P., Deneke, H., Radenz, M., and Tegen, I. (2020): The day-to-day co-variability between mineral dust and cloud glaciation: a proxy for heterogeneous freezing. *Atmospheric Chemistry and Physics*.

DV processed the datasets, performed the analysis, designed the figures and drafted the manuscript. IT, BH, PS and DV contributed to the design of the study. All authors contributed valuable feedback throughout the process. All authors helped with the discussion of the results and contributed to the final manuscript.

- Villanueva, D., Senf, F., and Tegen, I. (2021): The hemispheric and seasonal contrast in cloud thermodynamic phase from A-Train spaceborne instruments. *Journal of Geophysical Research Atmospheres*.

DV contributed to the conceptualization, formal analysis, investigation, visualization and writing (original draft). FS and IT contributed to the conceptualization and writing (review and editing).

- Villanueva, D., Neubauer, D., Gasparini, B., Ickes, L., and Tegen, I. (2021b): Constraining the impact of dust-driven droplet freezing on climate using cloud top phase observations. Accepted to *Geophysical Research Letters* (with modifications).

DV contributed to the conceptualization, formal analysis, investigation, visualization and writing (original draft). DN provided support and advice for ECHAM-HAM. BG contributed the results with the E3SM model. LI provided the implementation of the NS scheme in ECHAM-HAM. DN, BG, LI, and IT contributed to the conceptualization and writing (review and editing).

Not part of this thesis

- Villanueva, D., and Schepanski, K. (2019). Investigation of atmospheric conditions fostering the spreading of legionnaires' disease in outbreaks related to cooling towers. *International Journal of Biometeorology*.

DV contributed to the conceptualization, formal analysis, investigation, visualization and writing (original draft). KS contributed to the conceptualization and writing (review and editing).

Appendix C

Curriculum Vitae

Personal data

Name: Diego Villanueva
Address: Oststr. 66a, 04317 Leipzig, Germany
Date of birth: 06 November 1991 in Santiago, Chile
Phone: +49 1522 15299234
E-mail: ortiz@tropos.de

Education and professional experience

- 2017 – present** **PhD student**, *Leibniz Institute for Tropospheric Research, Leipzig, Germany*, Doctoral thesis: A story of dust and ice — constraining dust-driven immersion freezing in climate models using spaceborne retrievals
- 2014 – 2017** **M.Sc. Meteorology**, *University of Leipzig, Leipzig, Germany*, Master thesis: Atmospheric spreading of infectious diseases
- 2015 – 2017** **Research assistant**, *Leibniz Institute for Tropospheric Research, Leipzig, Germany*, Investigation of atmospheric conditions fostering the spreading of legionnaires' disease in outbreaks related to cooling towers
- 2010 – 2014** **B.Sc. Physics and Mathematics**, *University of Chile, Santiago, Chile*

Appendix D

Declaration of Independence

I hereby declare that I prepared this PhD thesis without inadmissible aid and only by the usage of the specified sources. I also declare that I marked the directly or indirectly adopted ideas from external references. Furthermore, I confirm that this PhD thesis is entirely the result of my own investigations except where otherwise indicated. In particular, I assure that I did not use the assistance of a doctoral consultant. I guarantee that no one has gained pecuniary advantages related to the content of this PhD thesis from me or from other persons on behalf of me.

I assure that this PhD thesis was not submitted in an identical or similar design to another examination office for the purpose of a graduation or another examination procedure. I also state that I have not been involved in another PhD procedure.

Leipzig, May 15, 2021
